PhD thesis

Prediction of Atmospheric Dispersion on All Scales for Emergency Preparedness

Kasper Skjold Tølløse

Supervisors: Eigil Kaas (NBI) & Jens Havskov Sørensen (DMI),
Co-supervisor: Henrik Feddersen (DMI)

Submitted: May 31, 2024

This thesis has been submitted to the PhD School of The Faculty of Science, University of Copenhagen

A Thesis Submitted for the Degree of Doctor of Philosophy

Author:	M.Sc. Kasper Skjold Tølløse
E-mail:	kasper.tollose@nbi.ku.dk, ktoe@dmi.dk
UCPH username:	qrm173
Ph.D. partners:	Niels Bohr Institute, University of Copenhagen Danish Meteorological Institute Innovation Fund Denmark

University Supervisor (NBI): Professor Eigil Kaas

External Supervisor (DMI): PhD Jens Havskov Sørensen

External Co-Supervisor (DMI): PhD Henrik Feddersen

Abstract

Long-range atmospheric dispersion modelling is carried out at the Danish Meteorological Institute (DMI) to predict concentration and deposition fields of various kinds of hazardous matter such as radioactive gasses and particles, toxic chemicals and smoke, aerosols containing infectious germs, and volcanic ash particles. These simulations are provided as a service to the responsible Danish authorities, thereby enabling early warnings and facilitating the implementation of optimal countermeasures in different emergency situations. The atmospheric dispersion is modelled by using the Danish Emergency Response Model of the Atmosphere (DERMA), which is a Lagrangian puff model designed specifically for long-range dispersion modelling. However, to extend this capability to a shorter range (up to about 50 km from the source), reformulations of essential parts of the model are required. In this PhD thesis, a new hybrid particle-puff approach is developed and implemented in DERMA, enabling the model to simulate short-range atmospheric dispersion more accurately. This new description of turbulent diffusion is evaluated against data from three different tracer experiments to validate both the short-range and long-range capabilities of the model.

In addition, both historical and recent events have demonstrated the necessity for being able to conduct inverse modelling as an operational service. This capability would assist responsible authorities in localizing unknown sources and/or characterizing the temporal development of gas and particle emissions in emergency situations. Therefore, two inverse methods have been developed: The first allows for source localization based on a set of air concentration measurements in cases where the release location is unknown. The second enables estimation of the multi-nuclide source term from a nuclear power plant accident in cases where little or no direct information about the release is available, as it has in fact been the case in historical nuclear accidents. This second method is designed specifically for use in the early stages of an accident, where an improved source term estimate may be crucial for facilitating reliable dispersion predictions.

The developments and findings in this PhD project successfully lay the foundations for new operational tasks at DMI while also constituting important contributions to the research field of dispersion modelling, especially inverse modelling for source term estimation and localization.

Resume

Ved Danmarks Meteorologiske Institut (DMI) foretages lang-distance spredningsmodellering for at udarbejde prognoser for koncentrationer og deponerede mængder af luftbårne partikler og gasser til forskellige beredskabsformål. Dette kan for eksempel være relevant ved radioaktive udslip, spredning af askepartikler fra vulkanudbrud og luftbårne dyresygdomme såsom mund- og klovsyge. Formålet er at forsyne de relevante beredskabsmyndigheder med oplysninger, som kan give bedre grundlag for at håndtere forskellige krisesituationer. Til disse formål benyttes *the Danish Emergency Response Model of the Atmosphere* (DERMA), som er en Lagrangesk puff model, der er udviklet specifikt til simulering af langdistancespredning. Der er dog et stigende behov for, at DERMA også skal kunne simulere spredning på kortere distancer (indenfor de første ca. 50 km fra kilden). I dette ph.d.-projekt udvikles en ny hybrid partikel/puff beskrivelse af turbulent diffusion, som har til formål at forbedre DERMA's egenskaber på korte distancer. Denne nye turbulensbeskrivelse evalueres ved at sammenligne modelforudsigelser med observationer fra tre forskellige sporgaseksperimenter, som tester modellens evner på både korte og lange distancer.

Derudover har både historiske og nylige hændelser vist, at der er et behov for at kunne bruge invers modellering til at lokalisere ukendte kilder samt at kunne estimere størrelser og tidsforløb for et udslip, hvor informationer om disse mangler eller er usikre. Derfor udvikles to forskellige inverse metoder: Den første er udviklet til kildelokalisering i tilfælde, hvor udslipspunktet er ukendt, og den anden er udviklet til at estimere kildens størrelse og tidsforløb i tilfælde, hvor udslipspunktet er kendt, men der mangler information om udslippets omfang. Den sidstnævnte metode er tiltænkt de tidligste stadier af en ulykke på et kernekraftværk, hvor en bedre kildeestimering kan være afgørende for at kunne simulere realistiske spredningsmønstre.

Resultaterne af ph.d.-projektet danner grundlaget for, at DMI i fremtiden kan varetage nye, eller udvidede, operationelle opgaver indenfor spredningsmodellering. Derudover bidrager projektet med vigtige resultater indenfor disse forskningsfelter, særligt indenfor brug af probabilistiske inverse metoder.

Acknowledgements

I am grateful for the help and support I have received throughout this process. First, I would like to thank my supervisor, Jens Havskov Sørensen, for his continuous investment in the project and for always making time to discuss my research. I also want to thank my supervisor, Eigil Kaas, for his valuable inputs, and my co-supervisor, Henrik Feddersen, for his assistance with creating the NWP model data essential for conducting my simulations. Additionally, I would like to thank Professor Andreas Stohl and his *Atmospheric Transport Processes* group at the University of Vienna for their hospitality and the interesting discussions during my stay there.

I also want to express my appreciation to my colleagues and fellow PhD students at both NBI and DMI for making this experience more enjoyable.

Finally, I would like to thank my family, friends, and my partner, Freja, for their support through everything. Their encouragement has been crucial in helping me navigate through the challenges and successes of this project.

Contents

Chapter 1

Introduction

1.1 Motivation

Airborne transport of radioactive or otherwise harmful particles and gasses plays an important role in different types of emergency preparedness. Applications include radioactive releases associated with e.g., nuclear power plant accidents or detonation of nuclear weapons, ash from volcanic eruptions, and airborne spread of certain animal diseases. In addition, there are several categories of minor releases, such as accidental leakage of gasses or smoke from wildfires, which may cause high concentrations locally.

Particles and gasses can be transported by the wind over large distances. During this transport, atmospheric turbulence will mix it with the surrounding air and thereby gradually lower the concentration while distributing it over a larger area. Other processes may cause particles to deposit onto the ground either by direct contact with the surface or due to rainout or washout by precipitation. Additionally, some materials may undergo radioactive decay or may interact chemically along the way, adding further complexity.

From a modelling perspective, it can be useful to distinguish between transport over different spatial scales (e.g., Zannetti, 2013). In this thesis, we will make the following distinction between different transport scales:

- near-field transport: within 1 km from the source,

- short-range transport: within 50 km from the source,

- long-range transport: above 50 km from the source and including synoptic scale phenomena,

- global transport.

For emergency preparedness, the main interest is in the short-range and long-range transport regimes, depending on the type of incident and its location relative to the area

of interest. Of course, most accidents will have more severe consequences closer to the location of the event, i.e. in the near-field regime. However, on these scales, dispersion modelling may not always be the most relevant tool.

1.1.1 Examples of applications for emergency preparedness

Historical events have shown that accidents in nuclear power plants release enormous amounts of radioactive nuclides into the atmosphere, which can be transported thousands of kilometers by the wind. The most notable example was the Chernobyl disaster in April 1986, where a core meltdown in one of the four reactors of the Chernobyl nuclear power plant caused an explosion and a subsequent radioactive release to the atmosphere (Saenko et al., 2011). Roughly 116,000 people were evacuated from the area, and in addition to the 28 people who died from direct exposure to radiation, the radioactive release may, according to some estimates, be responsible for more than 20,000 cases of thyroid cancer in Ukraine, Belarus, and Russia during the period 1991-2015 (Weiss, 2018).

Before the Chernobyl disaster, atmospheric transport was not believed to have a significant impact over such long distances. However, the detection of high levels of deposited Cs-137 in Sweden ($> 37,000$ Bq/m^2) (Saenko et al., 2011), more than 1000 km from the Chernobyl power plant, highlighted the necessity for long-range dispersion modelling in nuclear emergency preparedness (Ádám Leelőssy et al., 2018).

Another major historical nuclear accident is the Fukushima disaster. In March 2011, the Fukushima Daiichi nuclear power plant had three of its six reactor cores damaged after it was hit by a tsunami and, as a consequence, more than 200,000 people were evacuated from the area (Koo et al., 2014). Fortunately, westerly winds mostly transported the radioactive plume over the Pacific Ocean, whereas northerly winds could have transported it in the direction of Tokyo, which is located only about 220 km south-southwest of Fukushima. Instead, when the plume finally reached the west coast of North America after at least 5,000 km of travel, the concentrations of Cs-137 that could be detected were far below concerning levels (Koo et al., 2014).

In addition, long-range dispersion modelling is relevant for the transport of ash from volcanic eruptions, where potentially large amounts of microscopic ash particles can be injected into the atmosphere (Beckett et al., 2020). Given enough explosive power, the initial vertical distribution of particles may reach high into the troposphere or even well above the tropopause. In such cases, the concentration levels may impact flight safety, as demonstrated by the eruption of the Icelandic volcano below the glacier Eyjafjallajökull in April 2010. The plume of ash caused the airspace above parts of Europe to close for almost a week, costing the airline industry an estimated US $ 250 million per day (Gudmundsson et al., 2010).

Finally, in veterinary emergency preparedness, atmospheric dispersion modelling can potentially be a useful tool in case of an outbreak of certain viral diseases on animal farms (Sørensen et al., 2001). Previous cases have demonstrated that airborne spread of foot-and-mouth disease (FMD), may be transported several hundred kilometers from an infected farm while maintaining concentrations high enough to potentially infect new farms (Sørensen et al., 2000; Mikkelsen et al., 2003).

1.1.2 Use of inverse modelling for atmospheric dispersion

Inverse atmospheric dispersion modelling can be used in cases where information is lacking about the release, e.g. if the source term is poorly estimated and/or if the release location is unknown. In October 2017, a plume of Ru-106 drifted over Europe and was detected in more than 1000 air filter measurements from 34 different countries, but no release was officially reported (Masson et al., 2019). Several studies have attempted to estimate the source location in this case, with most findings pointing towards the southern Ural region of Russia, suggesting the Mayak nuclear facility as the most likely release location (Sørensen, 2018; Saunier et al., 2019; Le Brazidec et al., 2020; Kovalets et al., 2020; Tomas et al., 2021). However, some work still needs to be done on developing robust methods that are suitable for operational use for emergency preparedness.

Further, inverse modelling can be used to estimate the magnitude as well as the temporal evolution of a release based on available measurements. In the historical nuclear power plant accidents, the exact circumstances of the releases remain uncertain. Therefore, efforts have been made to estimate the source term describing the releases from both the Chernobyl accident (Liu et al., 2017; Davoine and Bocquet, 2007) and the Fukushima accident (Winiarek et al., 2012; Stohl et al., 2012; Saunier et al., 2013; Liu et al., 2017; Terada et al., 2020).

Similarly, in the event of a future accident, it is likely that a significant source of uncertainty of the predicted dispersion will be due to a lack of information about the source term. Thus, for emergency preparedness, there is still a need for methods that can use the early available measurements to constrain the source term sufficiently to make useful predictions of atmospheric dispersion of the released radionuclides. This task is further complicated by the fact that, at the early stages, mainly measurements from ground-based gamma dose rate monitors will be available. This is because the network of filter measurement stations is sparse, and they have a low sampling frequency, e.g. 12 hours, 24 hours, or even less frequently. The network of gamma dose rate monitors is, at least in some areas, relatively dense and samples at a high frequency, e.g. ten minutes or one hour. However, the drawback is that gamma dose rates are measurements of the combined radiation from all gamma-emitting nuclides. Studies have been carried out on developing methods for source term estimation based on gamma dose rates (Saunier et al., 2013, 2020; Tichý et al., 2018), but solving this inverse problem presents significant challenges because, as discussed by Saunier et al. (2013), the problem may be ill-conditioned due to the many degrees of freedom of the source term.

1.2 Objectives and outline

This thesis describes an industrial PhD with the Danish Meteorological Institute (DMI) acting as the industrial partner. Hence, the framework for the PhD is the current and possible future emergency preparedness related tasks carried out by DMI for the relevant authorities. Further, the research carried out as part of this study is centered on the Danish Emergency Response Model of the Atmosphere (DERMA), which is DMI's Lagrangian puff model (Sørensen, 1998; Baklanov and Sørensen, 2001; Sørensen et al., 2007). DERMA is specifically developed for long-range dispersion modelling and, thus, some assumptions are not valid on shorter spatial scales. For example, DERMA assumes instant, complete vertical mixing within the planetary boundary layer (PBL), which may cause large biases near the release location.

Currently, DERMA is used operationally for long-range dispersion in case of nuclear

accidents, volcanic eruptions, and airborne animal diseases (Sørensen et al., 2000, 2001; Mikkelsen et al., 2003; Gloster et al., 2010). The objectives of this PhD are to develop new methodologies enabling DERMA to be used for the following tasks:

- inverse modelling for source localization in case of unknown release location,
- inverse modelling for source term estimation in case of a nuclear power plant accident, intended to be used at the early stages of an accident in order to obtain a reliable source term for further simulations,
- short-range modelling, which most importantly includes the development and implementation of a new turbulence description.

The thesis is structured as follows:
The present Chapter gives an introduction as well as an overview of the thesis, Chapter 2 presents the theory and background relevant to the research conducted as part of the thesis. However, since the articles include parts of the theoretical background, this chapter should be read in combination with the papers to get the full overview. Next, the research results are presented in the same chronological order that the research was carried out. First, Chapter 3 presents the results from the two projects on inverse modelling, including two published research articles and some additional supplementary results. Next, the development and implementation of the new turbulence description in DERMA is described in Chapter 4 in the form of an unpublished manuscript. Finally, Chapter 5 summarizes the conclusions and presents a broader discussion of the results in relation to the defined objectives, as well as a discussion of perspectives for further research.

1.3 Manuscripts and results included in the thesis

The thesis includes three manuscripts in full length presenting the main results of the research. The first two have been published, whereas submission of the third manuscript is planned to follow shortly after the hand-in of the PhD thesis. Further, the supplementary results presented in Chapter 3.3 were partly published in the final report of the DMI-organized NKS-project SOurce CHAracterizatiOn accounting for meTeorologIcal unCertainties (SOCHAOTIC), which was also co-authored by the author of this thesis (Sørensen et al., 2023). The report is not included in full length; instead, only the relevant results are included in the thesis.

Paper 1 (first author)
   Tølløse, K. S., Kaas, E., and Sørensen, J. H. (2021). Probabilistic inverse method for source localization applied to etex and the 2017 case of ru-106 including analyses of sensitivity to measurement data. *Atmosphere*, 12(12)

Paper 2 (first author)
   Tølløse, K. S. and Sørensen, J. H. (2022). Bayesian inverse modelling for probabilistic multi-nuclide source term estimation using observations of air concentration and gamma dose rate. *Atmosphere*, 13(11)

Paper 3 (first author)
   Tølløse, K. S. and Sørensen, J. H. (2024*). A New Hybrid Particle-Puff Approach to Atmospheric Dispersion Modelling, Implemented in the Danish Emergency Response Model of the Atmosphere (DERMA). **manuscript not yet submitted*

References

Baklanov, A. and Sørensen, J. H. (2001). Parameterisation of radionuclide deposition in atmospheric dispersion models. *Phys. Chem. Earth*, 26:787–799.

Beckett, F. M., Witham, C. S., Leadbetter, S. J., Crocker, R., Webster, H. N., Hort, M. C., Jones, A. R., Devenish, B. J., and Thomson, D. J. (2020). Atmospheric dispersion modelling at the london vaac: A review of developments since the 2010 eyjafjallajökull volcano ash cloud. *Atmosphere*, 11(4).

Davoine, X. and Bocquet, M. (2007). Inverse modelling-based reconstruction of the chernobyl source term available for long-range transport. *Atmospheric Chemistry and Physics*, 7(6):1549–1564.

Gloster, J., Jones, A., Redington, A., Burgin, L., Sørensen, J. H., Turner, R., Hullinger, P., Dillon, M., Astrup, P., Garner, G., D'Amours, R., Sellers, R., and Paton, D. (2010). Airborne spread of foot-and-mouth disease – model intercomparison. *Veterinary Journal*, 183:278–286.

Gudmundsson, M. T., Pedersen, R., Vogfjörd, K., Thorbjarnardóttir, B., Jakobsdóttir, S., and Roberts, M. J. (2010). Eruptions of eyjafjallajökull volcano, iceland.

Koo, Y.-H., Yang, Y.-S., and Song, K.-W. (2014). Radioactivity release from the fukushima accident and its consequences: A review. *Progress in Nuclear Energy*, 74:61–70.

Kovalets, I. V., Romanenko, O., and Synkevych, R. (2020). Adaptation of the rodos system for analysis of possible sources of ru-106 detected in 2017. *Journal of environmental radioactivity*, 220:106302.

Le Brazidec, J. D., Bocquet, M., Saunier, O., and Roustan, Y. (2020). Mcmc methods applied to the reconstruction of the autumn 2017 ruthenium-106 atmospheric contamination source. *Atmospheric Environment: X*, 6:100071.

Liu, Y., Haussaire, J.-M., Bocquet, M., Roustan, Y., Saunier, O., and Mathieu, A. (2017). Uncertainty quantification of pollutant source retrieval: comparison of bayesian methods with application to the chernobyl and fukushima daiichi accidental releases of radionuclides. *Quarterly Journal of the Royal Meteorological Society*, 143(708):2886–2901.

Masson, O., Steinhauser, G., Zok, D., Saunier, O., Angelov, H., Babić, D., Bečková, V., Bieringer, J., Bruggeman, M., Burbidge, C., et al. (2019). Airborne concentrations and chemical considerations of radioactive ruthenium from an undeclared major nuclear release in 2017. *Proceedings of the National Academy of Sciences*, 116(34):16750–16759.

Mikkelsen, T., Alexandersen, S., Astrup, P., Champion, H. J., Donaldson, A. I., Dunkerley, F. N., Gloster, J., Sørensen, J. H., and Thykier-Nielsen, S. (2003). Investigation of airborne foot-and-mouth disease virus transmission during low-wind conditions in the early phase of the uk 2001 epidemic. *Atmos. Chem. Phys*, 3:2101–2110.

Saenko, V., Ivanov, V., Tsyb, A., Bogdanova, T., Tronko, M., Demidchik, Y., and Yamashita, S. (2011). The chernobyl accident and its consequences. *Clinical Oncology*, 23(4):234–243. The Radiobiological Consequences of the Chernobyl Accident 25 Years On - April 2011.

Saunier, O., Didier, D., Mathieu, A., Masson, O., and Le Brazidec, J. D. (2019). Atmospheric modeling and source reconstruction of radioactive ruthenium from an undeclared major release in 2017. *Proceedings of the National Academy of Sciences*, 116(50):24991–25000.

Saunier, O., Korsakissok, I., Didier, D., Doursout, T., and Mathieu, A. (2020). Real-time use of inverse modeling techniques to assess the atmospheric accidental release of a nuclear power plant. *Radioprotection*, 55:107–115.

Saunier, O., Mathieu, A., Didier, D., Tombette, M., Quélo, D., Winiarek, V., and Bocquet, M. (2013). An inverse modeling method to assess the source term of the fukushima nuclear power plant accident using gamma dose rate observations. *Atmospheric Chemistry and Physics*, 13(22):11403–11421.

Sørensen, J., Feddersen, H., Tølløse, K., Uppstu, A., Klein, H., Ulimoen, M., Robertson, L., Pehrsson, J., Lauritzen, B., Hac-Heimburg, A., Roed, H., Améen, E., Syed, N., Blixt Buhr, A., Lindgren, J., and Peltonen, T. (2023). *SOurce CHAracterizatiOn accounting for meTeorologIcal unCertainties (SOCHAOTIC) – final report: Final report of the NKS-B SOCHAOTIC activity*. NKS Secretariat. Report no NKS-470.

Sørensen, J. H. (1998). Sensitivity of the derma long-range gaussian dispersion model to meteorological input and diffusion parameters. *Atmospheric Environment*, 32(24):4195–4206.

Sørensen, J. H. (2018). Method for source localization proposed and applied to the october 2017 case of atmospheric dispersion of ru-106. *Journal of environmental radioactivity*, 189:221–226.

Sørensen, J. H., Baklanov, A., and Hoe, S. (2007). The danish emergency response model of the atmosphere (derma). *Journal of environmental radioactivity*, 96(1-3):122–129.

Sørensen, J. H., Jensen, C. Ø., Mikkelsen, T., Mackay, D., and Donaldson, A. I. (2001). Modelling the atmospheric spread of foot-and-mouth disease virus for emergency preparedness. *Phys. Chem. Earth*, 26:93–97.

Sørensen, J. H., Mackay, D. K. J., Jensen, C. Ø., and Donaldson, A. I. (2000). An integrated model to predict the atmospheric spread of foot-and-mouth disease virus. *Epidemiol. Infect.*, 124:577–590.

Stohl, A., Seibert, P., Wotawa, G., Arnold, D., Burkhart, J. F., Eckhardt, S., Tapia, C., Vargas, A., and Yasunari, T. J. (2012). Xenon-133 and caesium-137 releases into the atmosphere from the fukushima dai-ichi nuclear power plant: determination of the source term, atmospheric dispersion, and deposition. *Atmospheric Chemistry and Physics*, 12(5):2313–2343.

Terada, H., Nagai, H., Tsuduki, K., Furuno, A., Kadowaki, M., and Kakefuda, T. (2020). Refinement of source term and atmospheric dispersion simulations of radionuclides

during the fukushima daiichi nuclear power station accident. *Journal of environmental radioactivity*, 213:106104.

Tichỳ, O., Šmídl, V., Hofman, R., and Evangeliou, N. (2018). Source term estimation of multi-specie atmospheric release of radiation from gamma dose rates. *Quarterly Journal of the Royal Meteorological Society*, 144(717):2781–2797.

Tomas, J. M., Peereboom, V., Kloosterman, A., and van Dijk, A. (2021). Detection of radioactivity of unknown origin: Protective actions based on inverse modelling. *Journal of environmental radioactivity*, 235:106643.

Weiss, W. (2018). Chernobyl thyroid cancer: 30 years of follow-up overview. *Radiation Protection Dosimetry*, 182(1):58–61.

Winiarek, V., Bocquet, M., Saunier, O., and Mathieu, A. (2012). Estimation of errors in the inverse modeling of accidental release of atmospheric pollutant: Application to the reconstruction of the cesium-137 and iodine-131 source terms from the fukushima daiichi power plant. *Journal of Geophysical Research: Atmospheres*, 117(D5).

Zannetti, P. (2013). *Air pollution modeling: theories, computational methods and available software.* Springer Science & Business Media.

Ádám Leelőssy, Lagzi, I., Kovács, A., and Mészáros, R. (2018). A review of numerical models to predict the atmospheric dispersion of radionuclides. *Journal of Environmental Radioactivity*, 182:20–33.

Chapter 2

Background

The articles written as part of this thesis include extensive theoretical sections, which are unnecessary to repeat in detail here. The aim of this chapter is instead to give an introduction to the different research fields and describe the theoretical foundation upon which the papers are based. However, some repetition will occur in order to make this chapter self-contained.

Chapter 2.1 gives a basic description of the phenomenon of atmospheric transport and the concept of turbulent diffusion, while 2.2 introduces Lagrangian model types and different approaches to modelling turbulent diffusion. Next, Chapter 2.3 describes the main concepts behind parameterization of turbulent quantities. Finally, Chapter 2.4 describes the Bayesian approach to solving inverse problems and presents the approaches typically used in relation to atmospheric dispersion.

2.1 Atmospheric transport and dispersion

The dynamics of the atmosphere are described by a set of non-linear partial differential equations, including the Navier-Stokes equations, which describe the momentum-conservation for a Newtonian fluid, conservation of energy via the thermodynamic equation, and mass conservation equations, i.e. continuity equations for dry air, water vapor, liquid water, and ice. As there are no known analytical solutions, to this equation system, weather forecasts are obtained through numerical integration of the equations starting from some set of initial conditions.

When it comes to airborne transport of particles and gasses, assuming that they behave as a passive tracer, i.e., they do not change the thermodynamic properties of the atmosphere but merely follow the atmospheric flow, the evolution of the concentration field can be described by the continuity equation

$$\frac{\partial c}{\partial t} = -\frac{\partial}{\partial x_i}(c u_i) + \lambda, \tag{2.1}$$

where c is the concentration of the passive tracer in units mass per volume, u_i is the wind component in the x_i-direction, and λ denotes any sinks or sources, which can represent e.g. radioactive decay or loss of mass due to deposition. Further, Eq. (2.1) should in theory include a molecular diffusion term, but this can often be assumed negligible. The equation is presented in Eulerian form, meaning that the left-hand side describes the evolution of the concentration c from a fixed point in space. The first term on the

right-hand side is the divergence of the kinematic flux cu_i, which can be interpreted as the difference between the mass flux in and out of an infinitesimal cube.

Most atmospheric dispersion models are so-called offline models, i.e. they take as input the wind fields and other relevant atmospheric variables, which are already calculated by numerical weather prediction (NWP) models. However, weather models apply Reynolds averaging to the equations in order to make a numerical solution of the equation system computationally feasible. This process involves writing any variable, a as a sum of a slowly varying mean flow variable A and a small fluctuating part a', and then applying the following averaging rules (Wyngaard, 2010, Ch. 2)

$$\overline{A + a'} = A,$$
$$\overline{(A + a')(B + b')} = AB + \overline{a'b'}, \tag{2.2}$$

where the overbar denotes averaging. Therefore, the turbulent fluctuations are not included in the wind fields resolved by NWP models, and the effects of turbulence must instead be parameterized. By applying Reynolds averaging to Eq. (2.1) the continuity equation instead reads

$$\frac{\partial C}{\partial t} = -\frac{\partial}{\partial x_i}\left(CU_i\right) - \frac{\partial}{\partial x_i}\left(\overline{c'u_i'}\right) + \lambda, \tag{2.3}$$

where $\overline{c'u_i'}$ is the average kinematic turbulent flux. This term is commonly parameterized by assuming a diffusion form

$$\overline{c'u_i'} = -K_i\frac{\partial C}{\partial x_i}, \tag{2.4}$$

where K_i is the turbulent diffusivity in the x_i-direction. Further, the first term on the right-hand side of Eq. (2.3) can further be expanded into

$$\frac{\partial}{\partial x_i}(CU_i) = C\frac{\partial U_i}{\partial x_i} + U_i\frac{\partial C}{\partial x_i},$$

describing the change in concentration due to divergence of the wind field and advection, respectively. It is common to assume that the three-dimensional average wind field is non-divergent, and we therefore get

$$\frac{\partial C}{\partial t} = -U_i\frac{\partial C}{\partial x_i} + \frac{\partial}{\partial x_i}\left(K_i\frac{\partial C}{\partial x_i}\right) + \lambda, \tag{2.5}$$

which is the advection-diffusion equation with the added sinks/sources term λ, and where the diffusion term represents the effects of turbulent mixing and not molecular diffusion.

In an Eulerian model, Eq. (2.5) can be solved numerically, if parameterizations for K_i and λ are provided. Examples of Eulerian dispersion models are MATCH and SILAM, which are the dispersion models used operationally for Swedish and Finnish emergency preparedness (Robertson et al., 1999; Sofiev et al., 2015).

One advantage of this model type is that Eulerian dispersion models automatically represent the concentration field C in a regular grid, whereas fully Lagrangian models must interpolate the concentration to a grid in order to provide a useful output. The drawback of this, however, is that Eulerian models use the same resolution throughout the domain, although the plume may not fill out the domain. In contrast, Lagrangian

models are not constrained by grid resolution in the same manner, because the evolution of the plume is simulated by predicting the particle positions.

Another disadvantage of Eulerian numerical models is the numerical dispersion associated with temporal and spatial discretization, which tends to generate artificial numerical noise. Additionally, Eulerian models generally require much shorter numerical time steps to maintain numerical stability. As discussed by Sofiev et al. (2015), these latter issues can, to some extent, be dealt with by using a semi-Lagrangian approach, i.e. particles follow Lagrangian trajectories that end up in grid point coordinates of a homogeneous Eulerian grid at each time step.

2.2 Atmospheric transport from a Lagrangian perspective

There are overall two types of Lagrangian dispersion models, stochastic particle models and puff models. Both solve the continuity equation in Lagrangian form, where the change in the concentration is seen from the perspective of the particle moving with the flow instead of from a fixed grid. We can rewrite both Eq. (2.1) and Eq. (2.5) on Lagrangian forms, again assuming that the wind field is non-divergent

$$\frac{\partial c}{\partial t} + u_i \frac{\partial c}{\partial x_i} = \lambda, \tag{2.6}$$

$$\frac{\partial C}{\partial t} + U_i \frac{\partial C}{\partial x_i} = \frac{\partial}{\partial x_i} \left(K_i \frac{\partial C}{\partial x_i} \right) + \lambda, \tag{2.7}$$

where the left-hand sides of the equations are the change of the concentration from the perspective of a particle moving with the wind field u_i and the mean wind field U_i, respectively. Note that in Eq. (2.6), the wind field u_i includes the turbulent fluctuations and, therefore, there is no turbulent flux term.

2.2.1 Lagrangian stochastic particle models

The conceptually simplest type of Lagrangian model is a stochastic particle model, where the particle trajectories follow the actual wind including the turbulent fluctuations, see illustration in Figure 2.1. As seen from Eq. (2.6), the change in concentration of each particle is then only due to λ, which represents processes such as radioactive decay and deposition. Essentially, this means that the stochastic trajectories explicitly account for turbulent mixing, and the final concentration field is simply calculated by adding the contributions from the various particles in each grid box. However, since the NWP model only provides the average wind, the turbulent fluctuating parts of the winds are simulated using stochastic differential equations, called the Langevin equations (Chock and Winkler, 1994)

$$\frac{\mathrm{d}u_i'}{\mathrm{d}t} = -\frac{u_i'}{t_{L_{u_i}}} + \left(\frac{2}{t_{L_{u_i}}} \right)^{1/2} \sigma_{u_i} \eta, \tag{2.8}$$

where $\sigma_{u_i}^2 = \overline{u_i' u_i'}$ is the variance of the turbulent fluctuation, $t_{L_{u_i}}$ is the Lagrangian time scale, which refers to the auto-correlation time scale of the corresponding wind component, and $\eta \in \mathcal{N}(0, 1)$ is a Gaussian distributed variable with a mean of zero and a variance one. The quantities $\sigma_{u_i}^2$ and $t_{L_{u_i}}$ can be linked to the turbulent diffusivity

via the relation $K_i = \sigma_{u_i}^2 t_{L_{u_i}}$. For the vertical component, it is necessary to take into account the change of σ_w with height, which adds an extra term to Eq. (2.8). The Langevin equations can then be written in the numerical form (Chock and Winkler, 1994)

$$v_i'(t + \Delta t) = \alpha_H v_i'(t) + \left(1 - \alpha_H^2\right)^{1/2} \sigma_{v_i}\eta, \qquad \text{(horizontal)} \qquad (2.9)$$

$$\frac{w'}{\sigma_w}(t + \Delta t) = \alpha_v \frac{w'}{\sigma_w}(t) + \left(1 - \alpha_v^2\right)^{1/2} \eta + (1 - \alpha_v)\, t_{L_w} \frac{\partial \sigma_w}{\partial z}(t), \qquad \text{(vertical)} \qquad (2.10)$$

where $\alpha_H = \exp\left(-\Delta t/t_{L_{v_i}}\right)$ and $\alpha_v = \exp\left(-\Delta t/t_{L_w}\right)$, where H and v denote horizontal and vertical. Further, the equation for horizontal components has been rewritten in terms of v_i', which here denotes the two-dimensional horizontal turbulent wind vector.

Examples of stochastic particle models are FLEXPART, which can be considered a "pure" stochastic particle model (Pisso et al., 2019), HYSPLIT, which allows the user to specify whether a particle or a puff formulation is used (Draxler and Hess, 1997), and NAME, which is a stochastic particle model that uses a puff description on shorter spatial scales (Jones et al., 2004).

A notable advantage of stochastic particle models is their explicit consideration of turbulence through stochastic trajectories, eliminating the need to parameterize turbulent flux terms resulting from Reynolds averaging. Thus, with reliable estimates of $\sigma_{u_i}^2$ and $t_{L_{u_i}}$, this model type has the potential to accurately simulate dispersion. In addition, Lagrangian transport schemes do not have the same problems with numerical dispersion and diffusion as Eulerian models. However, the main disadvantage is that many particles are needed to resolve the concentration field, which can cause these models to be computationally expensive. Further, to accurately represent the stochastic trajectories, the numerical time steps must be small compared to $t_{L_{u_i}}$, which may again add to the

Plume from stack

Particle model   Puff model
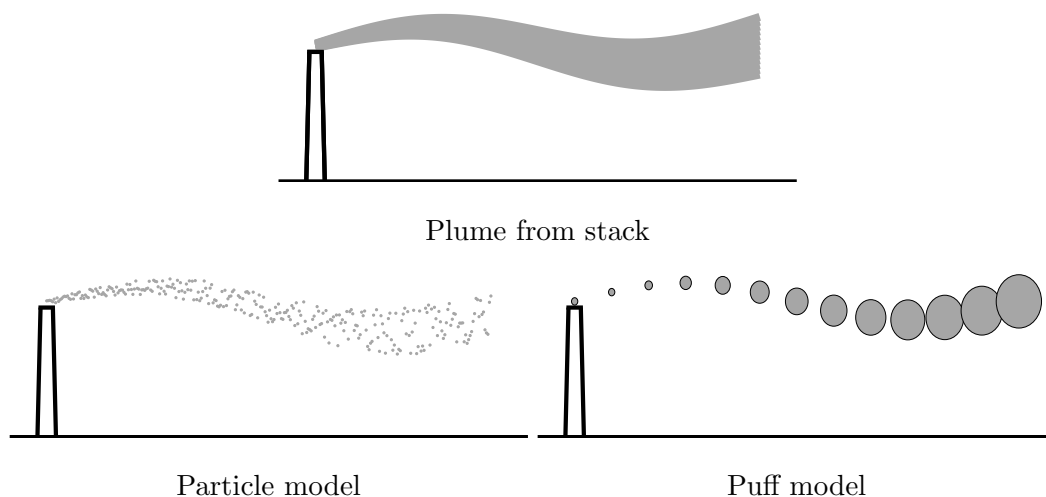
Figure 2.1: Illustration of the different modelling approaches. The upper figure shows the plume that is simulated by the models. The lower left figure illustrates how a stochastic particle model may simulate the dispersion, while the lower right figure illustrates a puff model. In practice, more puffs are of course released to ensure that the puffs overlap and form a continuous plume.

computational expenses (Stohl et al., 2005). As discussed by Jones et al. (2004), the particle approach is perhaps not suitable on short scales because of the many particles that are needed to sufficiently resolve the fine structures of the three-dimensional plume, which may ultimately not be resolved by the output grid. For long-range dispersion, on the other hand, Jones et al. (2004) argue that the particle approach is more appropriate, as the plume tends to be well-mixed throughout the PBL. For that reason, the NAME model employs a hybrid puff-particle approach for short-range modelling but transitions to a pure particle formulation on longer spatial scales (Jones et al., 2004).

2.2.2 Lagrangian puff models

In Lagrangian puff models, each particle/puff follows the mean wind trajectories, and the effects of turbulence are instead parameterized by assuming Gaussian diffusion around each puff center, see illustration in Figure 2.1. The relative dispersion around a particle moving with the mean wind can be related to the properties of the turbulent wind components as (Gifford, 1984)

$$\sigma_i^2 = 2\sigma_{u_i}^2 t_{L_{u_i}}^2 \left\{ \tau_i - \left(1 - e^{-\tau_i}\right) - \frac{1}{2}\left(1 - e^{-\tau_i}\right)^2 \right\}, \tag{2.11}$$

where t is the age of the puff, and $\tau_i = t/t_{L_{u_i}}$. The concentration field from a puff with center coordinates (x_p, y_p, z_p) can then be written as

$$C_p = \frac{Q_p}{2\pi\sigma_y^2\sigma_z}\exp\left\{-\frac{1}{2}\left(\frac{x - x_p}{\sigma_y}\right)^2 - \frac{1}{2}\left(\frac{y - y_p}{\sigma_y}\right)^2 - \frac{1}{2}\left(\frac{z - z_p}{\sigma_z}\right)^2\right\}, \tag{2.12}$$

where Q_p is the mass/activity carried by the puff, which is assumed radially symmetric in the horizontal dimensions. Hence, σ_y and σ_z denote the horizontal and vertical standard deviations of the puff's distribution, respectively.

In addition to HYSPLIT and NAME, which, as mentioned above include some puff elements, a few examples of puff models are CALPUFF (Scire et al., 2000) and RIM-PUFF (Thykier-Nielsen et al., 1999), which can both be considered "pure" puff models. Further, models such as DIPCOT (Andronopoulos et al., 2009), DERMA (Sørensen et al., 2007), and the Puff-Particle-Model (PPM) (De Haan and Rotach, 1998) are examples of models that combine the puff approach with stochastic particle trajectories. Like the hybrid formulation proposed by Jones et al. (2004) for short-range modelling, PPM divides dispersion into a meandering component and a puff component, representing relative dispersion. Thus, PPM aims to describe the turbulence more accurately by dividing the turbulence into these two physically distinct processes. However, to obtain this, PPM needs more particles and more frequent puff splitting compared to normal puff models and is therefore intended as a more efficient version of a stochastic particle model (De Haan and Rotach, 1998).

The main advantages of the puff model approach compared to stochastic particle models are that much fewer particles are needed to resolve the concentration field and that the trajectories following the mean wind can still be represented correctly using long numerical time steps because only the smooth mean wind trajectories need to be estimated. However, a significant disadvantage is that when puffs grow large, one of the underlying assumptions fails. This is because puffs are advected with the wind at their center, leading to unrealistic behavior when the puff size grows larger than the

characteristic scale of the wind shear. Especially the vertical wind shear, i.e. different wind speeds and directions at different heights, should in theory distort the Gaussian shape of the puff. The typical solution to this problem is vertical puff splitting, such that puffs growing larger than some threshold will be divided into, e.g., three new puffs at different heights. This approach is used in models such as CALPUFF, RIMPUFF, NAME, HYSPLIT and PPM (Scire et al., 2000; Thykier-Nielsen et al., 1999; Jones et al., 2004; Draxler and Hess, 1997; De Haan and Rotach, 1998).

While this approach does enable a more physically realistic behavior, the use of puff splitting may, as noted by Draxler and Hess (1997), cause practical issues because the number of puffs may exceed the array dimension. While solutions exist for this, such as puff merging, it introduces a new layer of complexity to the code structure. A different solution to the problem, avoiding the use of puff splitting, is the approach used in DERMA proposed by Sørensen (1998). In DERMA, complete mixing is assumed within the boundary layer. Thus, the concentration field from a puff within the boundary layer is described by a modified version of (2.12)

$$ C_p = \frac{Q_p}{2\pi\sigma_y^2 h}\exp\left\{-\frac{1}{2}\left(\frac{x - x_p}{\sigma_y}\right)^2 - \frac{1}{2}\left(\frac{y - y_p}{\sigma_y}\right)^2\right\}\delta(z, h), \qquad (2.13) $$

where $\delta(z, h) = 1$ if $z < h$ and otherwise $\delta(z, h) = 0$. According to the discussion above, this formulation is only anticipated to amplify the issue of puffs growing larger than the characteristic scale of vertical wind shear. However, DERMA combines this formulation with a stochastic transport scheme, which randomly moves puff centers in the vertical direction inside the PBL, thereby ensuring that all puffs are exposed to the vertical wind shear. While this formulation is perhaps less intuitive than using puff splitting, DERMA has demonstrated a good performance when compared to other models for long-range dispersion (Graziani et al., 1998).

On the other hand, the formulation in Eq. (2.13) is not suitable for short-range modelling, primarily due to the instantaneous complete mixing. The development of a new, more advanced hybrid particle-puff formulation for DERMA is one of the main focuses of this PhD. Hence, the topic is further explored in the manuscript presented in Chapter 4.1.

The different model formulations described above depend on unknown quantities, which represent statistics of the turbulent fluctuations, either K_i in the Eulerian case, or the turbulent quantities $\sigma_{u_i}^2$ and $t_{L_{u_i}}$. However, estimating these requires some understanding of the atmospheric boundary layer turbulence, which is the subject of the subsequent section.

2.3 Turbulence in the planetary boundary layer

Turbulence is chaotic, which means that it is only theoretically predictable for time scales characteristic of the dynamics considered. Since the time scales of the largest turbulent eddies of the atmosphere are in the order of tens of minutes, they can be considered random for most practical purposes. However, although the actual turbulent fluctuations are random, underlying statistics governing this random motion may still be described. This section is mostly based on Wyngaard (2010, Ch. 9-10), with additional references explicitly cited where relevant. Given the extensive scope of this subject, the

purpose of this section is mainly to motivate the ideas behind the common approaches used for parameterizing turbulent quantities.

2.3.1 Structure of the PBL

In the free atmosphere, the atmospheric flow is largely laminar. However, as a lower boundary condition of the atmosphere, the contact with the stationary surface of the earth imposes a no-slip condition. Thus, in the lowest part of the atmosphere, there will always be a region with vertical wind shear, which may cause the formation of turbulence. The turbulent eddies then tend to enhance vertical mixing, thereby creating a region with well-mixed conditions, which we generally call the planetary boundary layer (PBL) or the atmospheric boundary layer (ABL). Thus, the magnitude of the vertical wind shear is very important for the turbulent conditions of the PBL. Specifically, we often consider the shear production of turbulent kinetic energy (TKE), which can be assumed proportional to

$$\left(\frac{\partial U}{\partial z}\right)^2 + \left(\frac{\partial V}{\partial z}\right)^2.$$

In addition to this mechanical interaction, there is also an exchange of heat between the atmosphere and the surface, which greatly impacts the static stability of the atmosphere. In practice, the surface flux of virtual potential temperature, also called the *buoyancy flux*, is considered. This quantity impacts the gradient of virtual potential temperature, which accounts for the stability effects related to both the temperature profile and water vapor content in the atmosphere. Generally, the atmosphere can be considered statically stable when the virtual potential temperature increases with height, i.e.

$$\frac{\partial \Theta_v}{\partial z} > 0.$$

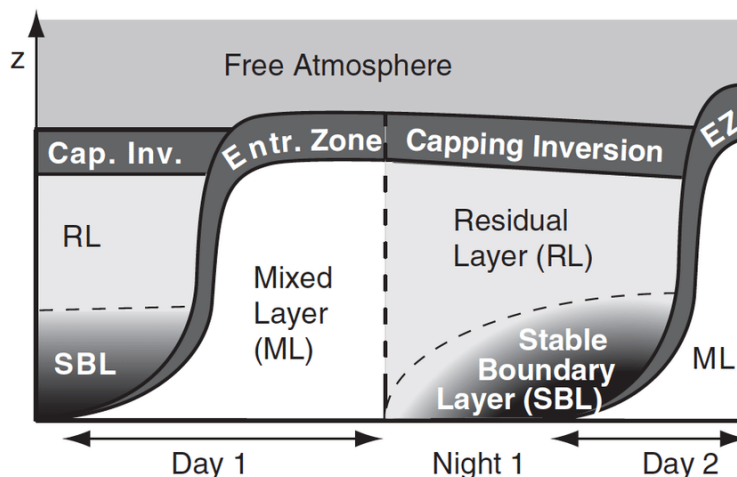Figure 2.2: Illustration of the typical diurnal cycle of the PBL over land and under clear skies. At sunrise, heating from the surface initiates the formation of a convective boundary layer/mixed layer. At sunset, the surface starts effectively losing heat via long-wave radiation and, therefore, starts cooling the atmosphere from below, forming a stable nocturnal boundary layer. The figure is from Stull et al. (2000).

Static stability is very important for the behavior of the PBL because an unstable stratification will amplify any vertical movement and typically produce more turbulent eddies. A stable stratification, on the other hand, dampens the vertical movement and tends to reduce the amount of turbulence and thereby vertical mixing.

An important concept relating these means of turbulent production is the *dynamic stability*, which can be quantified through the gradient Richardson number

$$Ri = \frac{\frac{g}{T_v}\frac{\partial \Theta_v}{\partial z}}{\left(\frac{\partial U}{\partial z}\right)^2 + \left(\frac{\partial V}{\partial z}\right)^2}, \tag{2.14}$$

which is the fraction of the *buoyant production* of turbulence (may be positive or negative) and the *shear production*. The atmospheric flow is said to be dynamically unstable for $Ri < Ri_c$, where $Ri_c = 0.25$ is the typically agreed critical Richardson number. On the other hand, when Ri exceeds this limit, the stable stratification is strong enough to "kill" the turbulence produced by the wind shear.

The surface fluxes of momentum and heat play an important role for the resulting structure of the PBL. The latter is related to the temperature difference between the surface and the atmosphere, which causes a natural diurnal cycle in the structure of the PBL. The typical diurnal cycle consists of a growing convective boundary layer during the day, which is dominated by buoyant production, while during the night when the surface cools the atmosphere, the PBL will tend to stably stratify, see Figure 2.2. Further, above the stably stratified nocturnal boundary layer (NBL), there may be a residual layer with "left-over" turbulence from the previous day. It should be noted that this typical diurnal cycle may evolve differently depending on the conditions, e.g., a low cloud cover at night may absorb and re-emit long-wave radiation and prevent the formation of the NBL. Further, even when a stable nocturnal boundary layer is formed, its structure may not be constant, but the NBL may intermittently be destroyed by the turbulence in the residual layer.

As mentioned previously, the static stability is determined by the buoyancy flux, which can be related to the surface sensible and latent heat fluxes, Q_s and Q_l, as $(w'\theta_v')_0 \approx (Q_s + 0.07Q_l)/(\rho_0 c_p)$, where ρ_0 is the surface air density and c_p is the heat capacity at constant pressure (Zannetti, 2013, Ch. 3). The surface momentum flux $\tau_0 = -\rho_0\sqrt{\overline{(w'u')}_0^2 + \overline{(w'v')}_0^2}$ is often considered via the so-called friction velocity $u_* = \sqrt{\tau_0/\rho_0}$. As described in the following sections, these quantities are fundamental in any PBL parameterization.

2.3.2 Surface layer

As the structure of the PBL is highly complex, some understanding can be gained from considering different parts of the boundary layer individually. Right above the surface is a thin *viscous sublayer*, where only molecular diffusion is responsible for the vertical transport of momentum, heat, and moisture. Above this is the *surface layer*, typically the lowest $\sim 10\%$ of the PBL, where turbulent fluxes can be assumed constant with height.

By assuming that the surface layer structure depends only on z, u_*, $(w'\theta_v')_0$, and g/T_v, Monin and Obukhov (1954) used similarity theory to show that the structure of the mean wind speed U and the mean virtual potential temperature Θ_v could be written

as

$$\frac{\kappa z}{u_*} \frac{\partial U}{\partial z} = \phi_m \left(\frac{z}{L}\right) \quad \text{and} \quad -\frac{\kappa z u_*}{\left(\overline{w'\theta_v'}\right)_0} \frac{\partial \Theta_v}{\partial z} = \phi_h \left(\frac{z}{L}\right), \tag{2.15}$$

where the left-hand sides are dimensionless gradients, and ϕ_m and ϕ_h are unknown functions of the dimensionless height z/L. Further, $\kappa = 0.4$ is the von Kármán constant, and the length scale L, called the Obukhov length, is defined as

$$L = -\frac{u_*^3 T_v}{\kappa g \left(\overline{w'\theta_v'}\right)_0}. \tag{2.16}$$

Using experimental data, the functions ϕ_m and ϕ_h can be estimated, for example, Högström (1988) proposed the following expressions

$$
\begin{aligned}
\text{stable}: \quad &\phi_m &&= 1.0 + 4.8\frac{z}{L}, &&\phi_h = 1.0 + 7.8\frac{z}{L}, \\
\text{unstable}: \quad &\phi_m &&= \left(1.0 - 19.3\frac{z}{L}\right)^{-1/4}, \quad &&\phi_h = \left(1.0 - 12.0\frac{z}{L}\right)^{-1/2}.
\end{aligned}
\tag{2.17}
$$

By integrating (2.15) from the surface to some reference height, the surface fluxes can be determined.

2.3.3 Turbulence parameterizations in Lagrangian dispersion models

Just as Monin and Obukhov (1954) showed how the constant surface fluxes of momentum and heat can be estimated based on simple assumptions about the surface layer structure, estimates of the turbulent fluxes throughout the remaining boundary layer can be based on similar considerations. As already described, in Lagrangian dispersion models, the turbulent fluxes are related to the quantities $\sigma_{u_i}^2$ and $t_{L_{u_i}}$.

As described by e.g. Zannetti (2013, Ch. 3), many different parameterizations exist, and most of them rely on semi-empirical relations between $\sigma_{u_i}^2$ and $t_{L_{u_i}}$ and the quantities z, u_*, L, as well as the PBL height h. In addition, while u_* is typically assumed a representative velocity scale of stable and neutral boundary layers, a convective velocity scale is typically assumed the representative velocity scale of unstable boundary layers

$$w_* = \left(\frac{hg \left(\overline{w'\theta_v'}\right)_0}{T_v}\right)^{1/3}. \tag{2.18}$$

As part of the improvement of DERMA in the short-range regime, the parameterization by Hanna (1984) was implemented, which is described in further detail in the manuscript presented in Chapter 4.

2.4 Inverse dispersion modelling

The term *inverse problem* describes any problem where a physical quantity cannot be measured directly. Instead, it must be inferred indirectly through another quantity, which, when combined with physical or mathematical models, enables the estimation of the quantity of interest. This section provides a brief introduction to Bayesian theory and its applications to atmospheric dispersion problems.

First, we consider Bayes' theorem, which connects the probability distribution of a set of parameters $\mathbf{m}$, representing the variables we seek to estimate, to a set of observations $\mathbf{y}$, which only provide indirect information about $\mathbf{m}$:

$$P(\mathbf{m}|\mathbf{y}, I) = \frac{P(\mathbf{m}|I)\,P(\mathbf{y}|\mathbf{m}, I)}{P(\mathbf{y}|I)}. \tag{2.19}$$

Here, $P(\mathbf{m}|\mathbf{y}, I)$ is the posterior probability distribution for $\mathbf{m}$, given $\mathbf{y}$ as well as I, representing any prior informaiton. Next, $P(\mathbf{m}|I)$ is the prior probability distribution for $\mathbf{m}$, i.e. based only on I, and $P(\mathbf{y}|\mathbf{m}, I)$ is the likelihood, which is the probability distribution for $\mathbf{y}$ given $\mathbf{m}$. Finally, for most practical purposes, $P(\mathbf{y}|I)$ is an unknown normalization constant and, therefore, Eq. (2.19) is often written on the form

$$P(\mathbf{m}|\mathbf{y}, I) \propto P(\mathbf{m}|I)\,P(\mathbf{y}|\mathbf{m}, I). \tag{2.20}$$

2.4.1 Solving inverse problems

In order to estimate the posterior distribution, we must be able to solve the *forward problem*, which is the problem relating $\mathbf{m}$ to a set of modelled observations $\hat{\mathbf{y}}$. This can be written as

$$\hat{\mathbf{y}} = f(\mathbf{m}), \tag{2.21}$$

where f is the *forward operator*. In addition, some functional forms need to be assumed for $P(\mathbf{m}|I)$ and $P(\mathbf{y}|\mathbf{m}, I)$. The former will depend strongly on the type of variable and the available prior information, while the latter is often assumed to be Gaussian, $P(\mathbf{y}|\mathbf{m}, I) = \mathcal{N}(\hat{\mathbf{y}}, \boldsymbol{\sigma})$, where $\boldsymbol{\sigma}$ may be related to uncertainties of both observations and model predictions (Tarantola, 2005).

One approach to solving inverse problems is to simply maximize Eq. (2.20) and thereby find the optimal solution for $\mathbf{m}$. In the simplest cases, where f is linear, and where both the likelihood and the prior distribution are Gaussian, an analytical solution can be found (Tarantola, 2005). In more complex cases, e.g. with a non-linear f, more advanced variational methods can be used, such as the 3D-var and 4D-var methods typically used for data assimilation in numerical weather prediction models (Andersson et al., 1998; Courtier et al., 1994).

However, instead of estimating the optimal solution for $\mathbf{m}$, there are also probabilistic inversion methods that sample the posterior probability distribution by evaluating the right-hand side of Eq. (2.20) for a sufficiently large number of realizations of $\mathbf{m}$ and normalize the resulting distribution. One option is to use random-walk-based Markov Chain Monte Carlo (MCMC) methods, such as Metropolis-Hastings or Gibbs (Hastings, 1970; Casella and George, 1992) to explore the parameter space of $\mathbf{m}$. Although these methods are designed to gradually gravitate towards higher probabilities, they require tuning of case-dependent parameters such as the step size of the random walk. An alternative approach, avoiding the use of random walks, is Hamiltonian Monte Carlo (HMC) methods, which propose new realizations of $\mathbf{m}$ based on estimated gradients of the posterior distribution (Betancourt, 2017). An example of a Hamiltonian Monte Carlo algorithm is the No U-Turn Sampling (NUTS), which uses adaptive step sizing such that the user only needs to perform a minimum of parameter tuning (Hoffman et al., 2014). This advantage is significant compared to other Monte Carlo methods, which typically require parameter tuning to ensure convergence.

It is important to note that, despite the robustness of the mathematical framework for solving inverse problems, there is no guarantee that a method will converge to a meaningful solution, as these problems can be ill-conditioned. As discussed by e.g. Enting (2002, Ch. 8), this issue is particularly relevant for atmospheric dispersion modelling, because the diffusive processes lead to a gradual information loss as the tracer is dispersed. Combined with the fact that the three-dimensional plume is typically only sampled by a coarse two-dimensional surface network, this means there may not be enough data to adequately constrain the parameters we are trying to estimate.

2.4.2 Source-receptor relationship

In the context of dispersion modelling, the forward problem, also sometimes called the source-receptor relationship, is the relation between a certain release scenario and a set of modelled observations. Solving this problem consists of first running the dispersion model based on the specific scenario and then interpolating the resulting concentration field to the locations and times of the measurements. A detailed description is provided in the article presented in Chapter 3.1, but the basics are covered in the description below.

First, we can write the atmospheric dispersion problem as $L(C) = Q$, where C is the concentration field, $Q = Q(\mathbf{m}, \mathbf{x}, t)$ is a source function related to the source term model $\mathbf{m}$, a vector containing relevant quantified information about the source term, and $L(\cdot)$ is the forward advection-diffusion operator, based on Eq. (2.7)

$$L(\cdot) = \frac{\partial}{\partial t}(\cdot) + \mathbf{U} \cdot \nabla(\cdot) - \nabla \cdot (\mathbf{K}\nabla(\cdot)) - \lambda(\cdot). \qquad (2.22)$$

Next, given the location and time of the i'th observation y_i, the corresponding modelled observation is calculated as

$$\hat{y}_i = \langle C, h_i \rangle \equiv \int_t \int_V C h_i \, \mathrm{d}V \, \mathrm{d}t, \qquad (2.23)$$

where h_i is a filter function, extracting the concentration at the location and time of the i'th measurement. This forward-based approach has been used for both source localization (e.g., Saunier et al., 2019; Le Brazidec et al., 2020) and for source term estimation in cases with known location (e.g., Stohl et al., 2012; Liu et al., 2017; Saunier et al., 2020). However, since this approach requires a new run with the dispersion model for every proposed source location, it may not be computationally efficient, if prior knowledge is limited.

Another approach is to make use of the adjoint model. This method relies on the Lagrangian duality relationship (Pudykiewicz, 1998; Marchuk et al., 2005)

$$\langle C, Q^* \rangle = \langle C^*, Q \rangle, \qquad (2.24)$$

where C^* is the adjoint concentration field obtained running the adjoint dispersion model with the source term Q^*, i.e. $L^*(C^*) = Q^*$, where the adjoint advection-diffusion operator is defined as

$$L^*(\cdot) = -\left(\frac{\partial}{\partial t}(\cdot) + \mathbf{U} \cdot \nabla(\cdot)\right) - \nabla \cdot (\mathbf{K}\nabla(\cdot)) - \lambda(\cdot). \qquad (2.25)$$

As we can see from this equation, the total derivative changes sign in the adjoint version, meaning that puffs follow back-trajectories. It follows from Eq. (2.24) that, by setting $Q^* = h_i$, the modelled observation $\hat{y}_i$ can be computed as

$$\hat{y}_i = \langle C_i^*, Q \rangle = \int_t \int_V C_i^* Q \, \mathrm{d}V \, \mathrm{d}t. \tag{2.26}$$

Hence, Eq. (2.23) and Eq. (2.26) provide two mathematically equivalent methods for solving the forward problem. Depending on the specific inverse problem, there may be advantages to either of the two approaches. The forward-based approach requires a run with the dispersion model for every proposed source term model, whereas the adjoint-based approach requires a run with the adjoint dispersion model for each available observation. Thus, the efficiency of each approach will depend on how well the prior distribution constrains $\mathbf{m}$, as well as on the number of observations available. For this reason, the adjoint-based approach is popular for source localization methods in particular, where it may significantly reduce the number of model runs needed (e.g., Seibert et al., 2002; Yee et al., 2014; Efthimiou et al., 2017; Kovalets et al., 2018; Sørensen, 2018; Tomas et al., 2021).

Based on these considerations, the methods developed as part of this PhD, described thoroughly in Chapter 3, use an adjoint-based approach for source localization and a forward-based approach for cases with known release location. Figure 2.3 is from the article presented in Chapter 3.1 and shows the resulting two-dimensional probability distribution for source location when the method is applied to the Ru-106 case.
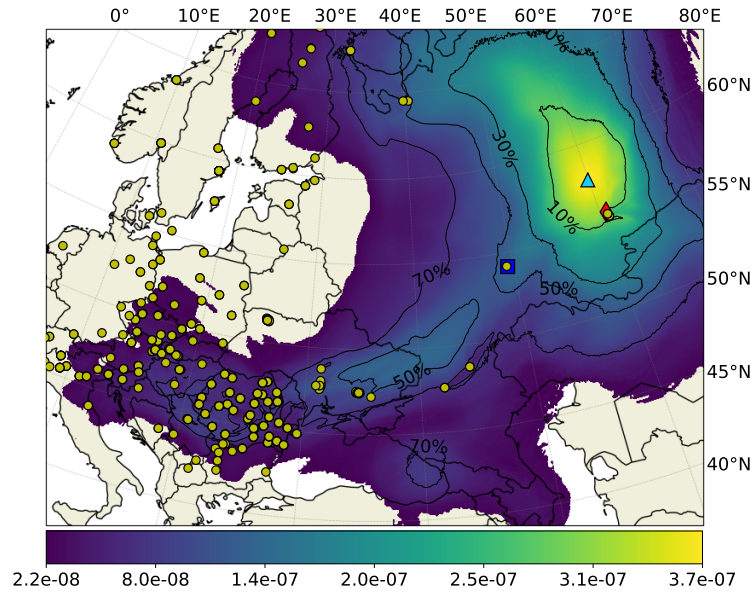
Figure 2.3: Example of a probabilistic source localization method applied to the Ru-106 case. The blue triangle shows the location of the highest probability density, the red diamond shows the location of the Mayak nuclear facility, the blue square shows the location of the NIIAR nuclear facility, and the yellow circles show the locations of the sampling stations. For more details, see the original figure description in the article in Chapter 3.1 The figure is from Tølløse et al. (2021).

References

Andersson, E., Haseler, J., Undén, P., Courtier, P., Kelly, G., Vasiljevic, D., Brankovic, C., Gaffard, C., Hollingsworth, A., Jakob, C., Janssen, P., Klinker, E., Lanzinger, A., Miller, M., Rabier, F., Simmons, A., Strauss, B., Viterbo, P., Cardinali, C., and Thépaut, J.-N. (1998). The ecmwf implementation of three-dimensional variational assimilation (3d-var). iii: Experimental results. *Quarterly Journal of the Royal Meteorological Society*, 124(550):1831–1860.

Andronopoulos, S., Davakis, E., and Bartzis, J. G. (2009). Rodos-dipcot model description and evaluation. *Report RODOS (RA2)-TN (09)*, 1.

Betancourt, M. (2017). A conceptual introduction to hamiltonian monte carlo. *arXiv preprint arXiv:1701.02434*.

Casella, G. and George, E. I. (1992). Explaining the gibbs sampler. *The American Statistician*, 46(3):167–174.

Chock, D. P. and Winkler, S. L. (1994). A particle grid air quality modeling approach: 1. the dispersion aspect. *Journal of Geophysical Research: Atmospheres*, 99(D1):1019–1031.

Courtier, P., Thépaut, J.-N., and Hollingsworth, A. (1994). A strategy for operational implementation of 4d-var, using an incremental approach. *Quarterly Journal of the Royal Meteorological Society*, 120(519):1367–1387.

De Haan, P. and Rotach, M. W. (1998). A novel approach to atmospheric dispersion modelling: The puff-particle model. *Quarterly Journal of the Royal Meteorological Society*, 124(552):2771–2792.

Draxler, R. R. and Hess, G. (1997). Description of the hysplit4 modeling system.

Efthimiou, G. C., Kovalets, I. V., Venetsanos, A., Andronopoulos, S., Argyropoulos, C. D., and Kakosimos, K. (2017). An optimized inverse modelling method for determining the location and strength of a point source releasing airborne material in urban environment. *Atmospheric environment*, 170:118–129.

Enting, I. G. (2002). *Inverse problems in atmospheric constituent transport*. Cambridge University Press.

Gifford, F. (1984). The random force theory: Application to meso-and large-scale atmospheric diffusion. *Boundary-Layer Meteorology*, 30(1):159–175.

Graziani, G., Klug, W., and Mosca, S. (1998). *Real-time long-range dispersion model evaluation of the ETEX first release*. Office for Official Publications of the European communities.

Hanna, S. (1984). Applications in air pollution modeling. In *Atmospheric Turbulence and Air Pollution Modelling: A Course held in The Hague, 21–25 September, 1981*, pages 275–310. Springer.

Hastings, W. K. (1970). Monte carlo sampling methods using markov chains and their applications.

Hoffman, M. D., Gelman, A., et al. (2014). The no-u-turn sampler: adaptively setting path lengths in hamiltonian monte carlo. *J. Mach. Learn. Res.*, 15(1):1593–1623.

Högström, U. (1988). Non-dimensional wind and temperature profiles in the atmospheric surface layer: A re-evaluation. *Topics in micrometeorology. A Festschrift for arch dyer*, pages 55–78.

Jones, A., Thomson, D., Hort, M., and Devenish, B. (2004). The uk met office's next-generation atmospheric dispersion model, name iii. In *Air Pollution Modeling and its Application XVII, Proceedings of the 27th NATO/CCMS International Technical Meeting on Air Pollution Modelling and its Application*, pages 24–29.

Kovalets, I. V., Efthimiou, G. C., Andronopoulos, S., Venetsanos, A. G., Argyropoulos, C. D., and Kakosimos, K. E. (2018). Inverse identification of unknown finite-duration air pollutant release from a point source in urban environment. *Atmospheric Environment*, 181:82–96.

Le Brazidec, J. D., Bocquet, M., Saunier, O., and Roustan, Y. (2020). Mcmc methods applied to the reconstruction of the autumn 2017 ruthenium-106 atmospheric contamination source. *Atmospheric Environment: X*, 6:100071.

Liu, Y., Haussaire, J.-M., Bocquet, M., Roustan, Y., Saunier, O., and Mathieu, A. (2017). Uncertainty quantification of pollutant source retrieval: comparison of bayesian methods with application to the chernobyl and fukushima daiichi accidental releases of radionuclides. *Quarterly Journal of the Royal Meteorological Society*, 143(708):2886–2901.

Marchuk, G., Shutyaev, V., and Bocharov, G. (2005). Adjoint equations and analysis of complex systems: Application to virus infection modelling. *Journal of computational and applied mathematics*, 184(1):177–204.

Monin, A. and Obukhov, A. (1954). Osnovnye zakonomernosti turbulentnogo peremeshivanija v prizemnom sloe atmosfery (basic laws of turbulent mixing in the atmosphere near the ground). *Trudy geofiz. inst. AN SSSR*, 24(151):163–187.

Pisso, I., Sollum, E., Grythe, H., Kristiansen, N. I., Cassiani, M., Eckhardt, S., Arnold, D., Morton, D., Thompson, R. L., Groot Zwaaftink, C. D., et al. (2019). The lagrangian particle dispersion model flexpart version 10.4. *Geoscientific Model Development*, 12(12):4955–4997.

Pudykiewicz, J. A. (1998). Application of adjoint tracer transport equations for evaluating source parameters. *Atmospheric environment*, 32(17):3039–3050.

Robertson, L., Langner, J., and Engardt, M. (1999). An eulerian limited-area atmospheric transport model. *Journal of Applied Meteorology and Climatology*, 38(2):190–210.

Saunier, O., Didier, D., Mathieu, A., Masson, O., and Le Brazidec, J. D. (2019). Atmospheric modeling and source reconstruction of radioactive ruthenium from an undeclared major release in 2017. *Proceedings of the National Academy of Sciences*, 116(50):24991–25000.

Saunier, O., Korsakissok, I., Didier, D., Doursout, T., and Mathieu, A. (2020). Real-time use of inverse modeling techniques to assess the atmospheric accidental release of a nuclear power plant. *Radioprotection*, 55:107–115.

Scire, J. S., Strimaitis, D. G., Yamartino, R. J., et al. (2000). A user's guide for the calpuff dispersion model. *Earth Tech, Inc*, 521:1–521.

Seibert, P., Frank, A., and Kromp-Kolb, H. (2002). Inverse modelling of atmospheric trace substances on the regional scale with lagrangian models. In *Proceedings of the EUROTRAC-2 Symposium*, pages 11–15. Garmisch-Partenkirchen, Germany.

Sofiev, M., Vira, J., Kouznetsov, R., Prank, M., Soares, J., and Genikhovich, E. (2015). Construction of the silam eulerian atmospheric dispersion model based on the advection algorithm of michael galperin. *Geoscientific Model Development*, 8(11):3497–3522.

Sørensen, J. H. (1998). Sensitivity of the derma long-range gaussian dispersion model to meteorological input and diffusion parameters. *Atmospheric Environment*, 32(24):4195–4206.

Sørensen, J. H. (2018). Method for source localization proposed and applied to the october 2017 case of atmospheric dispersion of ru-106. *Journal of environmental radioactivity*, 189:221–226.

Sørensen, J. H., Baklanov, A., and Hoe, S. (2007). The danish emergency response model of the atmosphere (derma). *Journal of environmental radioactivity*, 96(1-3):122–129.

Stohl, A., Forster, C., Frank, A., Seibert, P., and Wotawa, G. (2005). The lagrangian particle dispersion model flexpart version 6.2. *Atmospheric Chemistry and Physics*, 5(9):2461–2474.

Stohl, A., Seibert, P., Wotawa, G., Arnold, D., Burkhart, J. F., Eckhardt, S., Tapia, C., Vargas, A., and Yasunari, T. J. (2012). Xenon-133 and caesium-137 releases into the atmosphere from the fukushima dai-ichi nuclear power plant: determination of the source term, atmospheric dispersion, and deposition. *Atmospheric Chemistry and Physics*, 12(5):2313–2343.

Stull, R. B., Ahrens, C. D., et al. (2000). *Meteorology for scientists and engineers*.

Tarantola, A. (2005). *Inverse problem theory and methods for model parameter estimation*. SIAM.

Thykier-Nielsen, S., Deme, S., and Mikkelsen, T. (1999). Description of the atmospheric dispersion module rimpuff. *Riso National Laboratory, PO Box*, 49.

Tomas, J. M., Peereboom, V., Kloosterman, A., and van Dijk, A. (2021). Detection of radioactivity of unknown origin: Protective actions based on inverse modelling. *Journal of environmental radioactivity*, 235:106643.

Tølløse, K. S., Kaas, E., and Sørensen, J. H. (2021). Probabilistic inverse method for source localization applied to etex and the 2017 case of ru-106 including analyses of sensitivity to measurement data. *Atmosphere*, 12(12).

Wyngaard, J. C. (2010). *Turbulence in the Atmosphere*. Cambridge University Press.

Yee, E., Hoffman, I., and Ungar, K. (2014). Bayesian inference for source reconstruction: A real-world application. *International Scholarly Research Notices*, Volume 2014:12 pages.

Zannetti, P. (2013). *Air pollution modeling: theories, computational methods and available software.* Springer Science & Business Media.

Chapter 3

Inverse modelling for source term estimation

For emergency preparedness, the most important role of atmospheric dispersion modelling is of course being able to make forward calculations predicting current and future air and ground concentrations, which can support decision-making during emergency situations. However, in cases of unexplained elevated levels of harmful particles or gasses, it is likely that the responsible authorities wish to know the cause, at least in order to predict if there are geographical areas with worse conditions. However, it could also help provide a clearer understanding of the types of scenarios for which they need to prepare. In such cases, the main objective would be the localization of the source.

Moreover, during the initial phases of emergency situations, there may be limited information regarding what has actually happened. Thus, there will be large uncertainties on the estimated released amounts and, consequently, on the predicted dispersion. Therefore, a method for source term estimation can be very useful during or immediately after the release to enable better simulations of the dispersed matter.

In both these types of cases, inverse dispersion modelling can be used to estimate all quantifiable information about the source term, such as the location, spatial extent, and the temporal evolution of release rates, whether it is stationary or moving, etc. In theory, these two types of problems are described by the same overall inverse problem only with different prior knowledge about the source term. However, in order to develop methods that are best suited for the tasks they are intended to solve, it is useful to consider the two types of scenarios individually such that the methods can be tailored to the specific problems.

3.1 Paper 1: Probabilistic Inverse Method for Source Localization Applied to ETEX and the 2017 Case of Ru-106 including Analyses of Sensitivity to Measurement Data

The inspiration for this article (Tølløse et al., 2021) stemmed from the unexplained release of Ru-106 in 2017. Given the large amount of measurement data available (more than 1000 air concentration measurements from 34 different countries), the case offered an ideal opportunity to test source localization methods. Consequently, the case gave

rise to a series of studies attempting to estimate the location of the release based on the available measurements (Sørensen, 2018; Saunier et al., 2019; Le Brazidec et al., 2020; Kovalets et al., 2020; Tomas et al., 2021). These studies generally agree that the release most likely came from the southern Ural region in Russia, and most suggest the Mayak nuclear facility as a likely candidate.

In this article, we describe a new method for source localization, a probabilistic approach based on Bayesian theory which allows accounting for the uncertainties associated with both measurements and model predictions. For validation, the method is first applied to the ETEX case, where the method accurately predicts the source location. Further, to examine the robustness of the method, sensitivity analyses are performed, where the ETEX data is essentially modified to be more similar to the Ru-106 case. This involved excluding observations within varying distances from the source location, as well as computing average concentrations over extended durations using the three-hour average concentrations provided by the ETEX data. The method offers robust predictions, in the sense that the release location was predicted within the region of highest probability density throughout the sensitivity analyses. Finally, the method is applied to the Ru-106 case, leading us to the same conclusion as other studies: the Mayak nuclear facility is identified as the most probable release location.

3.1. PAPER 1: PROBABILISTIC INVERSE METHOD FOR SOURCE LOCALIZATION APPLIED TO ETEX AND THE 2017 CASE OF RU-106 INCLUDING ANALYSES OF SENSITIVITY TO MEASUREMENT DATA

Probabilistic Inverse Method for Source Localization Applied to ETEX and the 2017 Case of Ru-106 including Analyses of Sensitivity to Measurement Data

Kasper Skjold Tølløse [1,2,*] , **Eigil Kaas** [1,2] **and Jens Havskov Sørensen** [1]

1   Danish Meteorological Institute, DK-2100 Copenhagen, Denmark; ek@dmi.dk (E.K.); jhs@dmi.dk (J.H.S.)
2   Niels Bohr Institute, University of Copenhagen, DK-2100 Copenhagen, Denmark
*   Correspondence: ktoe@dmi.dk

Abstract: In recent years, cases of unexplained, elevated levels of radioactive particles have demonstrated an increasing need for efficient and robust source localization methods. In this study, a Bayesian method for source localization is developed and applied to two cases. First, the method is validated against the European tracer experiment (ETEX) and then applied to the still unaccounted for release of Ru-106 in the fall of 2017. The ETEX dataset, however, differs significantly from the Ru-106 dataset with regard to time resolution and the distance from the release site to the nearest measurements. Therefore, sensitivity analyses are conducted in order to test the method's sensitivity to these parameters. The analyses show that the resulting source localization depends on both the observed temporal resolution and the existence of sampling stations close to the source. However, the method is robust, in the sense that reducing the amount of information in the dataset merely reduces the accuracy, and hence, none of the results are contradictory. When applied to the Ru-106 case, the results indicate that the Southern Ural region is the most plausible release area, and, as hypothesized by other studies, that the Mayak nuclear facility is the most likely release location.

Keywords: source localization; atmospheric dispersion modelling; inverse modelling; Bayesian inference; ETEX; Ru-106

1. Introduction

In the case of an accidental release of a substance to the atmosphere, the time and location of the release may be unknown, in which case, only indirect information about the source location is available. If a network of sampling stations has detected the substance, this provides an indication of the geographic location of the plume of the substance at times later than the release time. There is no unambiguous way of calculating the source location from this information; instead, inverse problem theory is needed in order to relate the measurements to possible release scenarios. In the case of an unreported release of harmful particles or gasses, source localization is likely to be an operational task carried out by national emergency management agencies. The aim of this study is to develop and illustrate a method suitable for operational usage, and therefore, the focus is on efficiency and robustness.

Examples of previous work on source localization include different applications of adjoint dispersion modelling, i.e., running the model backwards in time, such as the methods by Pudykiewicz [1], Wotawa et al. [2], Seibert et al. [3,4], and Sørensen [5]. Some studies have combined adjoint dispersion modelling with Bayesian inference and Markov chain Monte Carlo methods, such as the method by Keats et al. [6] and Yee et al. [7,8]. One of the main challenges in inverse dispersion modelling is that model predictions are subject to large unknown errors, which complicate direct comparison of model and measurements. This is demonstrated by Yee et al. [8], who suggest altering the cost function to take this into account by representing the standard deviations with probability distributions allowing for

variation around the estimated uncertainties. Other studies suggest using a cost function that is less sensitive to outliers, i.e., model predictions with large errors, than the typical Gaussian distribution, such as the log-normal distribution [9,10]. As opposed to the previously mentioned studies, Saunier et al. [9] and Le Brazidec et al. [10] both estimate the source term using forward-based methods, utilizing a variational approach and a Markov chain Monte Carlo method, respectively. Another approach, which is also less sensitive to outliers, is to use a correlation-based cost function such as the methods by Efthimiou et al. [11], Kovalets et al. [12,13], and Tomas et al. [14]. An additional advantage of this approach is that evaluation of the probability is possible without a need for explicitly specifying the uncertainties.

A recent case, which has demonstrated the need for better source localization methods, is the release of Ru-106 in the fall of 2017 (see Section 2.2). To date, no release has been reported, but several studies have attempted to estimate the source location [5,9,10,13–15]. These studies are in overall agreement and point towards the Southern Ural region as the most likely release area. Within this geographical area, it has been suggested that the release site could be either the Mayak nuclear facility, cf. http://www.po-mayak.ru/ (accessed on 13 October 2021), or the NIIAR nuclear facility, cf. http://www.niiar.ru (accessed on 13 October 2021).

The methodology developed in this study is inspired by the combination of Bayesian inference and adjoint dispersion modelling used by Keats et al. [6] and Yee et al. [7,8] but with a correlation-based measure for the probability, similar to the method by Tomas et al. [14]. First, the method is validated against the European tracer experiment (ETEX) (see Section 2.1) and then applied to the Ru-106 case (Section 2.2). However, there are a few important differences between the ETEX dataset and the dataset of Ru-106 measurements: first, ETEX consists of a large set of three-hour measurements, whereas most measurements in the Ru-106 case are conducted over either approximately 12 h, 24 h, or one week; this is at least the case for the dataset used in this study, where a number of measurements have been discarded, because they do not meet the quality control requirements defined in Section 2.2. Second, in the ETEX case, there are several measurement stations located less than a few hundred kilometers from the release site, one of which is located directly downstream (see Section 3.1 for a discussion of this). In the Ru-106 case, on the other hand, most measurements that fulfill the quality control requirements are more than 2000 km away from the estimated source. There are a few measurements from locations in Russia close to the estimated source. However, these measurements are conducted over a week or more and therefore contain only limited information about when the plume of Ru-106 passed the measurement stations. To study the effects of the differences between the two datasets, the validation against the ETEX case includes analyses of the sensitivity to these parameters. In addition, the importance of including non-detections is examined, i.e., measurements conducted in the relevant geographical area and period, which have not detected concentrations above the detection limit. Further, there are a few differences that could be mentioned: the tracer gas used in the ETEX experiment was non-depositing and non-decaying, whereas Ru-106 is subject to both radioactive decay (although with a quite long half-life of 371.5 days) as well as dry and wet deposition.

Section 2 describes the data and methodology, Sections 2.1 and 2.2 describe the measurement datasets, Sections 2.3 and 2.4 describe the meteorological data and the dispersion model, while Sections 2.5 and 2.6 describe the methodology. Next, the results are presented and discussed in Section 3, Section 3.1 presents the results of the validation on the ETEX dataset, including tests of sensitivity to the data quality, and Section 3.2 shows the results of applying the methodology to the Ru-106 case. Finally, Section 4 presents a summary and the conclusions of the study.

2. Materials and Methods

2.1. ETEX Dataset

The European tracer experiment (ETEX) is a tracer gas experiment designed to test and compare the capabilities of atmospheric transport models to predict long-range atmospheric

dispersion [16,17]. ETEX consisted of two separate experiments, ETEX-1 and ETEX-2, of which only the first is considered in this study. The non-decaying and non-depositing gas perfluoromethylcyclohexane (PMCH) was used as tracer, and a total of 340 kg of the gas was released to the atmosphere with a constant release rate during the release period, starting from 16.00 UTC on 23 October 1994 and lasting 11 h and 50 min. The location of the release (48°03′30″ N, 2°00′30″ W) is close to the village of Monterfil in Brittany, France.

The sampling network consisted of 168 ground-level sampling stations distributed in 17 European countries. The sampling was carried out over 30 three-hour intervals, the first starting at 15.00 UTC on 23 October 1994, i.e., one hour before the release started. The different sampling stations were planned to start sampling about six hours before the expected time of tracer arrival. Therefore, each sampling station has not necessarily measured the concentration in all possible sampling intervals. A total of 3046 valid samples are available, of which 935 are measurements of non-zero concentrations, and the remaining are non-detections, i.e., levels below the detection limit.

As mentioned previously, the sensitivity analyses include a deliberate reduction in the temporal resolution of the ETEX dataset. This is performed by computing averages of four measurements at adjacent time intervals, such that a 12 h measurement interval is obtained. However, there are some measurement intervals, where measurements are lacking, which means that it is not possible to combine the measurements to 12 h averages. These intervals occur randomly throughout the measurement campaign. The measurements that only combine to shorter time intervals are discarded. This approach has resulted in a dataset consisting of a total of 665 12 h measurements, of which 281 are measurements of non-zero concentrations. This is repeated for 24 h intervals, resulting in a dataset consisting of 288 24 h measurements, of which 123 are measurements of non-zero concentrations.

2.2. Ru-106 Dataset

During September and October 2017, small concentrations of Ru-106 were detected in high-volume air samples in several European countries by different sampling networks. The concentration levels were below those requiring public protective actions, but the large geographical area affected suggested a release of considerable magnitude [18].

The dataset used in this study is adapted from Masson et al. [18]. The full dataset consists of more than 1000 air concentration measurements from 34 different countries, of which some are non-detections, i.e., levels below detection limits. However, for some of these measurements, information about the sampling period is limited to a start and end date, with no information on the time of the day. For measurements conducted over, e.g., 24 h, this incomplete information gives rise to large uncertainties. For longer measurements, on the other hand, imposing starting and ending time is not as problematic. In this study, all measurements conducted over less than five days where no starting and ending time is given have been discarded. For longer measurements, we assume that the measurement interval starts and ends at 12.00 UTC if the times are not specified. Further, a few measurement periods either start or end outside the simulation period (see Section 2.3), and hence, these measurements have been discarded as well. Finally, the dataset includes a number of non-detections with quite high detection limits compared to the numerical values of some of the non-zero measurements. As described in Section 2.6.1, the non-detections are interpreted as zeros, and therefore, non-detections with high detection limit have also been discarded from the dataset. The maximum accepted detection limit is chosen somewhat arbitrarily to the 5th percentile of all included non-zero measurements, which ensures that all included non-detections are, if not zero, at least small in comparison with the majority of the non-zero measurements. The limits defined in this way are $0.22 \, \mathrm{mBq \, m^{-3}}$ for measurements conducted over up to 36 h and $0.0030 \, \mathrm{mBq \, m^{-3}}$ for measurements conducted over more 36 h.

The dataset that remains, after discarding the measurements described above, consists of 583 samples, of which 349 are measurements of non-zero concentrations and the remaining are non-detections. However, approximately half of these measurements are

concentration averages over a week or more. It is questionable whether a weekly mean value is useful for source localization, since there is no information about when, during this period, the plume actually passed the measurement station. To address this issue, a source localization is first based on all 583 measurements, and next, a localization is based on two separate datasets: the first only including measurements conducted over up to 36 h, similar to approaches by other studies [5,14], and the second only including measurements conducted over more than 36 h. The purpose is to examine whether the weekly averages contain valuable information, but also whether including them in the dataset introduces a risk of reducing the accuracy of the localization.

2.3. Meteorological Data

The simulations have been conducted using meteorological data from the global numerical weather prediction model of the European Centre for Medium-Range Weather Forecasts (ECMWF) [19,20]. For the ETEX case, ERA5 reanalysis data [19] of horizontal resolution $0.25° × 0.25°$ are employed; for the Ru-106 case, cycle CY47R1 data [20] of $0.1° × 0.1°$ resolution. The meteorological fields are available hourly in regular lat-lon grids. The model simulation for the ETEX case starts on 27 October 1994 at 09.00 UTC and runs (backwards in time) until 22 October 1994 at 06.00 UTC. The model simulation for the Ru-106 case starts on 10 October 2017 at 00.00 UTC and runs (also backwards) until 21 September 2017 at 00.00 UTC. The domains used for the simulations are limited area domains: for the ETEX case, the domain limits are 20° W to 30° E and 40° N to 65° N, and for the Ru-106 case, the domain limits are 15° W to 80° E and 30° N to 70° N.

2.4. Dispersion Modelling

The atmospheric dispersion is modelled using the Lagrangian model DERMA, the Danish Emergency Response Model of the Atmosphere [21,22]. The model can be represented mathematically with the operator:

$$L(\cdot) = \frac{D}{Dt}(\cdot) - \nabla \cdot (\mathbf{K}\nabla(\cdot)) + \lambda(\cdot), \tag{1}$$

where $\frac{D}{Dt}(\cdot) = \frac{\partial}{\partial t}(\cdot) + \mathbf{u} \cdot \nabla(\cdot)$ is the total derivative and thus contains both the time derivative and the advection terms, $\mathbf{u}$ is the three-dimensional wind field, $\nabla \cdot (\mathbf{K}\nabla(\cdot))$ is the turbulent diffusion term, where $\mathbf{K}$ is the turbulent diffusion tensor, and λ denotes radioactive decay and deposition. Provided a source function Q, the concentration field C can then be obtained by numerically integrating the differential equation $L(C) = Q$.

Our method for source localization relies on the use of adjoint dispersion modelling, which implies that the sign of the total derivative is changed and the particles, and thus moves opposite the wind direction. The mathematical operator for the adjoint dispersion model is defined as [1,23]:

$$L^*(\cdot) = -\frac{D}{Dt}(\cdot) - \nabla \cdot (\mathbf{K}\nabla(\cdot)) + \lambda(\cdot). \tag{2}$$

The adjoint concentration field C^* can be obtained by applying a source function, Q^*, and numerically integrating the differential equation $L^*(C^*) = Q^*$. Note that only the total derivative changes sign, which can be interpreted as if the particles are moved backwards in time, but the physical processes diffusion, decay, and deposition behave as in the original forward-in-time model.

2.5. Source-Receptor Relationship

Although the aim is to estimate the location of the source, it is necessary to consider additional source term characteristics such as start time, duration, and amount of released material, since these characteristics are closely related to the release location. In this study, only stationary point releases with a constant release rate in a finite time interval are considered. Further, the source is assumed to be located inside the planetary boundary

layer (PBL), where the concentration is assumed constant with height and, consequently, only two spatial coordinates are necessary. Thus, all possible sources can be described by the following source term model:

$$\mathbf{m} = (\mathbf{x}_{\text{release}}, t_{\text{start}}, \Delta t_{\text{release}}, q),$$ (3)

where $\mathbf{x}_{\text{release}} = (\phi_{\text{release}}, \lambda_{\text{release}})$ are the horizontal coordinates of the source location, latitude, and longitude, respectively. t_{start} is the start time of the proposed release, $\Delta t_{\text{release}}$ is the duration, and q is the constant release rate.

In order to establish the source–receptor relationship, i.e., a function that relates a proposed source term model $\mathbf{m}$ to a set of expected detections $\hat{\mathbf{y}}$ (implying that a set of detections $\mathbf{y}$ exists), a source function $Q(\mathbf{m}, \mathbf{x}, t)$ must be related to the proposed source term model $\mathbf{m}$:

$$Q(\mathbf{m}, \mathbf{x}, t) = \delta(\mathbf{x} - \mathbf{x}_{\text{release}}) \, q_t(\mathbf{m}, t),$$ (4)

$$q_t(\mathbf{m}, t) = \begin{cases} q & t_{\text{start}} \leq t \leq t_{\text{start}} + \Delta t_{\text{release}} \\ 0 & \text{otherwise} \end{cases}.$$

Here, Q is the release rate corresponding to the proposed source term model $\mathbf{m}$ as function of location $\mathbf{x}$ and time t, and $\delta(\mathbf{x})$ is the Dirac delta function. Assuming that the ith measurement y_i is a point measurement at the location $\mathbf{x}_i$, initiated at time t_i, and of duration Δt_i, the expected detection $\hat{y}_i$ can be computed as the following inner product:

$$\hat{y}_i = \langle C, h_i \rangle \equiv \int_t \int_V C h_i \, \mathrm{d}V \, \mathrm{d}t = \frac{1}{\Delta t_i} \int_{t_i}^{t_i + \Delta t_i} C(\mathbf{x}_i) \, \mathrm{d}t,$$ (5)

where the filter function h_i extracts the concentration value C at the location and time of the ith measurement. C is related to $Q(\mathbf{m}, \mathbf{x}, t)$ as described in Section 2.4. To obtain the last equality in Equation (5), the following definition of the filter function is used:

$$h_i(\mathbf{x}, t) = \delta(\mathbf{x} - \mathbf{x}_i) \, \tau_i(t),$$ (6)

$$\tau_i(t) = \begin{cases} \Delta t_i^{-1} & t_i \leq t \leq t_i + \Delta t_i \\ 0 & \text{otherwise} \end{cases}.$$

Using Equation (5) to estimate the expected detections requires a forward run with the dispersion model for each proposed source term model, $\mathbf{m}$. If a large number of realizations of $\mathbf{m}$ is needed, this approach may be computationally inefficient. Instead, the method developed here relies on the adjoint source–receptor relationship [6–8], which is obtained by using the Lagrangian duality relationship. Only the main result is shown here, and for further details, the reader is referred to [1,6,23]. The Lagrangian duality relationship states:

$$\langle C, Q^* \rangle = \langle C^*, Q \rangle,$$ (7)

where, as described in Section 2.4, C is the concentration field obtained by using the source function Q, and C^* is the adjoint concentration field obtained by using the source function Q^*. Equation (7) provides a relation between the value of an adjoint concentration field C^* originating from a given location and the actual concentration C evaluated at the same location. By setting $Q^* = h_i$ and using Equations (5) and (7), it follows that the expected detections $\hat{y}_i$ can be computed using the adjoint concentration field:

$$\hat{y}_i = \langle C_i^*, Q \rangle = \int_t \int_V C_i^* Q \, \mathrm{d}V \, \mathrm{d}t,$$ (8)

where C_i^* is the adjoint concentration field obtained by using the filter function h_i as source function. Thus, when using this adjoint source–receptor relationship, it is sufficient to run

the adjoint dispersion model once per measurement instead of once per realization of $\mathbf{m}$. Further, using the definition of the source function, Equation (4), it follows that:

$$\hat{\mathbf{y}} = q\mathbf{X}, \text{ where} \tag{9}$$

$$X_i = X_i(\mathbf{x}_{\text{release}}, t_{\text{start}}, \Delta t_{\text{release}}) \equiv \int_{t_{\text{start}}}^{t_{\text{start}} + \Delta t_{\text{release}}} C_i^*(\mathbf{x}_{\text{release}}) \, dt.$$

Thus, the expected detection is proportional to the time integrated adjoint concentration field, and the proportionality constant is the proposed release rate q.

2.6. Proposed Method for Direct Marginal Posterior Estimation

Given a set of concentration measurements, $\mathbf{y}$, which contains indirect information about the source term, the probability distribution for the elements of $\mathbf{m}$, Equation (3), can be determined by applying Bayes' theorem:

$$P(\mathbf{m}|\mathbf{y}, I) = \frac{P(\mathbf{m}|I) \, P(\mathbf{y}|\mathbf{m}, I)}{P(\mathbf{y}|I)}, \tag{10}$$

where $P(\mathbf{m}|I)$ is the prior probability distribution for $\mathbf{m}$, $P(\mathbf{y}|\mathbf{m}, I)$ is the likelihood, and $P(\mathbf{y}|I)$ is a statistical model-independent constant called the evidence. I is any background information that may be available about, e.g., source location or amount of released material. To evaluate Equation (10), the quantities $P(\mathbf{m}|I)$ and $P(\mathbf{y}|\mathbf{m}, I)$ need to be estimated for a selection of realizations of $\mathbf{m}$, and the resulting posterior probability distribution $P(\mathbf{m}|\mathbf{y}, I)$ can then be estimated by normalizing the distribution. To obtain a good estimate of the probability distribution, it is important to make sure that the relevant parts of this parameter space is sampled. One option is to use Markov chain Monte Carlo methods to sample the parameter space [6–8,10]. This approach is especially useful for sampling very large parameter spaces. However, a few simplifications are described below, which further reduce the dimensionality of the parameter space, such that evaluation of the probability for the entire model grid is computationally feasible. Therefore, there is no need for using Markov chain Monte Carlo methods to sample the probability distribution.

Instead of sampling the posterior distribution for $\mathbf{m}$, the idea presented here is to obtain a direct estimate of the marginal posterior distribution for $\boldsymbol{\mu} = (\mathbf{x}_{\text{release}}, t_{\text{start}}, \Delta t_{\text{release}})$. First, the posterior probability distribution for $\mathbf{m}$ may be rewritten as:

$$P(q, \boldsymbol{\mu}|\mathbf{y}, I) = \frac{P(q|\boldsymbol{\mu}, I) \, P(\boldsymbol{\mu}|I) \, P(\mathbf{y}|q, \boldsymbol{\mu}, I)}{P(\mathbf{y}|I)}. \tag{11}$$

Further, it is useful to define the conditional posterior distribution for q, where $\boldsymbol{\mu}$ is assumed known:

$$P(q|\mathbf{y}, \boldsymbol{\mu}, I) = \frac{P(q|\boldsymbol{\mu}, I) \, P(\mathbf{y}|q, \boldsymbol{\mu}, I)}{P(\mathbf{y}|\boldsymbol{\mu}, I)}. \tag{12}$$

The marginal distribution for $\boldsymbol{\mu}$ can be related to Equations (11) and (12), and by reordering the terms, it can be shown that:

$$P(\boldsymbol{\mu}|\mathbf{y}, I) = \frac{P(q, \boldsymbol{\mu}|\mathbf{y}, I)}{P(q|\mathbf{y}, \boldsymbol{\mu}, I)} = \frac{P(\boldsymbol{\mu}|I) \, P(\mathbf{y}|\boldsymbol{\mu}, I)}{P(\mathbf{y}|I)}.$$

Focusing on the case where no quantifiable prior information about the source is available, both $P(\boldsymbol{\mu}|I)$ and $P(q|\boldsymbol{\mu}, I)$ can be assumed uniform. However, for the prior probability to be uniform for the source location, a factor of $\cos(\phi_{\text{release}})$ is necessary to compensate for the convergence of longitude lines approaching the poles. The marginal distribution for $\boldsymbol{\mu}$ is proportional to the evidence of the conditional posterior distribution for q, $P(\mathbf{y}|\boldsymbol{\mu}, I)$, which, in this case, reduces to:

$$P(\boldsymbol{\mu}|\mathbf{y}, I) \propto \int \cos(\phi_{\text{release}}) \, P(\mathbf{y}|q, \boldsymbol{\mu}, I) \, dq. \tag{13}$$

3.1. PAPER 1: PROBABILISTIC INVERSE METHOD FOR SOURCE LOCALIZATION APPLIED TO ETEX AND THE 2017 CASE OF RU-106 INCLUDING ANALYSES OF SENSITIVITY TO MEASUREMENT DATA

2.6.1. Likelihood and Uncertainty Quantification

In order to evaluate Equation (13), one first needs to define the likelihood, $P(\mathbf{y}|q, \boldsymbol{\mu}, I)$. The traditional approach is to evaluate the probability of observing y_i given the model prediction $\hat{y}_i = qX_i$ and some assumed probability distribution for the residual $y_i - qX_i$. For example, one could assume that $y_i - qX_i$ is Gaussian distributed with variance σ_i^2, such as the methods by Keats et al. and Yee et al. [6–8]. The variance can then be related to the uncertainties associated with both the observation and the model prediction $\sigma_i^2 = \sigma_{o,i}^2 + \sigma_{m,i}^2$, where $\sigma_{o,i}$ is the observation uncertainty, and $\sigma_{m,i}$ is the modelling uncertainty. The resulting likelihood is the joint Gaussian distribution:

$$P(\mathbf{y}|q, \boldsymbol{\mu}, I) = \frac{1}{\sqrt{(2\pi)^N |\mathbf{R}|}} \exp\left[-\frac{1}{2}(\mathbf{y} - q\mathbf{X})^{\mathrm{T}} \mathbf{R}^{-1}(\mathbf{y} - q\mathbf{X})\right], \tag{14}$$

where N is the number of measurements, $\mathbf{R} = \mathbf{O} + \mathbf{M}$ is the error covariance matrix, with $\mathbf{O}$ and $\mathbf{M}$ being the error covariance matrices for observation and modelling errors, respectively. $|\mathbf{R}|$ denotes the determinant of $\mathbf{R}$. Assuming that measurements are unbiased, the observation errors can be assumed uncorrelated, and hence $\mathbf{O}$ is a diagonal matrix with diagonal elements $\sigma_{o,i}^2$ related to the accuracy of the measurement equipment. The elements of $\mathbf{M}$, on the other hand, are unknown, and the structure is likely to be complex. There are three main contributions to the uncertainty on the time integrated adjoint concentration X_i: (1) errors in the estimated trajectories due to uncertain meteorological data, (2) errors in the turbulent diffusion and deposition due to inaccurate parameterizations, and (3) numerical errors. The two first contributions, which we assume are dominant, may cause systematic errors, e.g., due to systematic over- or underestimation of wind speeds or of the turbulent diffusion coefficients. Considering this nature of the modelling errors, it is likely that the errors on predictions that are close in time and space are correlated. However, estimating the off-diagonal elements of $\mathbf{M}$ is highly non-trivial, and therefore, the best solution might still be to assume that $\mathbf{M}$ is diagonal; previous studies also assume uncorrelated modelling errors [6–8,10]. Based on these assumptions, the likelihood in Equation (14) can be related to the following cost function:

$$J = \sum_i^N \left(\frac{y_i - qX_i}{\sigma_i}\right)^2, \tag{15}$$

such that $P(\mathbf{y}|q, \boldsymbol{\mu}, I) \propto \exp(-J)$. Although the values of $\sigma_{o,i}$ may be known, we assume that the errors on the model prediction are generally much larger than the observation uncertainties $\sigma_{m,i} \gg \sigma_{o,i}$, and hence $\sigma_i \approx \sigma_{m,i}$. Thus, minimizing J as defined in Equation (15) requires quantitative estimates of $\sigma_{m,i}$. In this study, we use an alternative correlation-based cost function, which allows for evaluation of the likelihood without the need for quantifying uncertainties. As described below, the cost function defined in Equation (15) will then only be used to determine the source strength. As mentioned previously, this approach is inspired by previous methods using correlation-based cost functions [11–14]. However, in contrast to the previous studies, we implement the correlation-based cost function in the Bayesian framework described in the previous section. Our method resembles the method by Tomas et al. [14], where the probability of a given source location is assumed to be proportional to the time integrated Pearson correlation coefficient. In our Bayesian framework, this corresponds to marginalizing over the t_{start} dimension of $P(\boldsymbol{\mu}|\mathbf{y}, I)$. Thus, the main difference is that the method presented here allows for releases of different durations.

The likelihood is assumed proportional to the reflective correlation coefficient defined as:

$$r(y_i, \hat{y}_i) = \frac{\sum_i y_i \hat{y}_i}{\sqrt{\sum_i y_i^2 \sum_i \hat{y}_i^2}}. \tag{16}$$

It should be stressed that this assumption is not theory-based, and that correlation cannot, in general, be interpreted as probability. Consequently, the resulting probability

distribution should be interpreted as a rough estimate of the true probability distribution. The use of the reflective correlation coefficient is also different from the previous studies, which use the regular Pearson correlation coefficient [11–14]. The reflective correlation coefficient can be thought of as a non-central version of the Pearson correlation coefficient. Both are normalized measures of the co-variation of two variables, but instead of comparing the variation around the mean values of each variable, the reflective correlation compares the variation around zero. Thus, as opposed to the Pearson correlation coefficient, r, as defined in Equation (16), is not invariant under translation, i.e., adding a constant to all instances of one of the variables will change the value of r. Both correlation coefficients are equal to either 1 or -1 for a perfect linear relation; however, the Pearson correlation coefficient assumes a relation of the form $y = ax + b$, whereas the reflective correlation assumes a relation of the form $y = ax$. Thus, r, as defined in Equation (16), is more suited for the problem considered here. Further, since concentration variables are non-negative, r varies between 0 and 1. Therefore, probabilities are naturally ensured to be non-negative as well.

Finally, as mentioned previously, one of the challenges in this problem is direct comparison of a measurement and a model prediction with a large, unknown error. However, the correlation is a measure of how well high and low values follow each other in the two variables. Thus, the exact value of the individual model prediction is less important, and hence, the correlation-based probability is potentially a robust alternative to more traditional approaches. Based on these considerations, it is also reasonable to include non-detections by assuming that these are measurements of zero concentration; as long as the detection limit of the filter station considered is small compared to the numerical values of the non-zero measurements.

Another important feature of the correlation coefficient is the independence of the release rate, q, due to the direct proportionality $\hat{\mathbf{y}} = q\mathbf{X}$. This means that the likelihood can be taken outside the integral in Equation (13), and thus, the marginal distribution $P(\boldsymbol{\mu}|\mathbf{y}, I)$ can be written as:

$$P(\boldsymbol{\mu}|\mathbf{y}, I) \propto \cos(\phi_{\text{release}}) \frac{\sum_i y_i X_i}{\sqrt{\sum_i y_i^2 \sum_i X_i^2}}, \tag{17}$$

where, as in Equation (9), X_i is the time integrated adjoint concentration at the location of the proposed release and over the proposed release interval.

Although the likelihood is independent of q, it is still possible to estimate the most likely release rate, denoted $\hat{q}$, since this is just the slope of the best linear fit. By minimizing the least-squares cost function defined in Equation (15) with respect to q, one obtains the expression:

$$\hat{q}(\boldsymbol{\mu}, \mathbf{y}) = \frac{\sum_i \sigma_i^{-2} y_i X_i}{\sum_i \sigma_i^{-2} X_i^2}.$$

Thus, in order to estimate $\hat{q}$, one needs to quantify σ_i. As described previously, we assume $\sigma_i \approx \sigma_{\text{m},i}$. We have then examined the perhaps three simplest assumptions: (1) assuming $\sigma_i \propto X_i$ as suggested by Keats et al. [6], (2) assuming $\sigma_i \propto y_i$, and (3) assuming σ_i constant, i.e., the uncertainty is the same for all model predictions. The idea behind the two first approaches is that the uncertianty should be of the same magnitude as the predicted concentration itself. The first approach, however, leads to the assumption that predictions of zero concentration has no uncertainty, and since these predictions are not rare, this approach does not work well in practice. The idea behind the third approach is that the model might be better at predicting higher concentrations, and accordingly, one should give greater weights to these terms. We found that the third approach gives the overall best results, while the second approach leads to systematic underestimation of the release rates for the ETEX case. It should be noted that this is not necessarily a general

result; it may depend on the dispersion model used as well as on the case considered. By assuming σ_i constant, we obtain the following simple expression for $\hat{q}$:

$$\hat{q}(\boldsymbol{\mu}, \mathbf{y}) = \frac{\sum_i y_i X_i}{\sum_i X_i^2}. \tag{18}$$

3. Results and Discussions

Since the elements of $\boldsymbol{\mu}$ are continuous variables, there are infinitely many possible realizations of $\boldsymbol{\mu}$ within the limited area domain of the simulation. However, it is assumed that the resolution of the output data is sufficient to properly resolve the main features of the probability distribution. The spatial resolution of the output is the same as the input meteorological data, see Section 2.3, and the concentration fields are output every third hour. Thus, only model grid points are considered as possible source locations, only model output times are considered possible start times, and only durations, which are multiples of the time-resolution of model output are considered possible release periods. In addition, an upper limit for the release duration has been chosen, of 36 h.

As described in the previous section, $P(\boldsymbol{\mu}|\mathbf{y}, I)$ is a four-dimensional probability distribution for the source location, start time, and duration. When nothing is known about the release time, the best estimate of the source location is obtained by marginalization:

$$P(\mathbf{x}_{\text{release}}|\mathbf{y}, I) = \int_{\Delta t_{\text{release}}} \int_{t_{\text{start}}} P(\boldsymbol{\mu}|\mathbf{y}, I) \, \mathrm{d}t_{\text{start}} \, \mathrm{d}\Delta t_{\text{release}}. \tag{19}$$

Another useful concept, which was applied to inverse atmospheric dispersion modelling by Tomas et al. [14], is the highest posterior density region (HDR) [24]. Let M be the sample space of $\mathbf{x}_{\text{release}}$, in this case, the coordinates of all grid points in the simulation domain. Given the probability density function $P(\mathbf{x}_{\text{release}}|\mathbf{y}, I)$, the $100(1 - \alpha)\%$ HDR is defined as the subset $R(P_\alpha)$ of the sample space of M, such that

$$R(P_\alpha) = \{\mathbf{x}_{\text{release}}|P(\mathbf{x}_{\text{release}}|\mathbf{y}, I) \geq P_\alpha\}. \tag{20}$$

Thus, the $100(1 - \alpha)\%$ HDR is the smallest possible region, in which the probability density integrates to $100(1 - \alpha)\%$. The HDR can be thought of as a generalization of a confidence interval, where $R(P_\alpha)$ is the most credible region for the confidence level $100(1 - \alpha)\%$. However, due to the assumptions described in Section 2.6, the probability distribution, and therefore the HDRs, should be interpreted with caution. Thus, it cannot a priori be assumed that, e.g., the 10% HDR corresponds to a 10% confidence level. Instead, the results based on the ETEX case can give an indication of how to interpret the different HDRs.

3.1. Application to the ETEX Case

First, the methodology is applied to the set of three-hour measurements, both with and without non-detections. The two-dimensional marginal distributions for the release location, shown in Figure 1, are obtained by initially applying Equation (17) and then Equation (19). Figure 1a shows the results based on non-zero measurements only, while Figure 1b shows the results when including non-detections. It should be noted that the plots do not use the same colorbars; instead, the minimum and maximum values on each colorbar are defined by the minimum value of the 90% HDR and the maximum value of the probability density. The reason is that comparing the overall structures of the probability densities is considered more relevant than comparing the actual values of the probability densities. Further, Table 1 shows the coordinates for the locations of maximum probability as well as the distances from these locations to the true release site. The table also shows results based on the different datasets used as part of the sensitivity analyses described in Section 3.1.1.
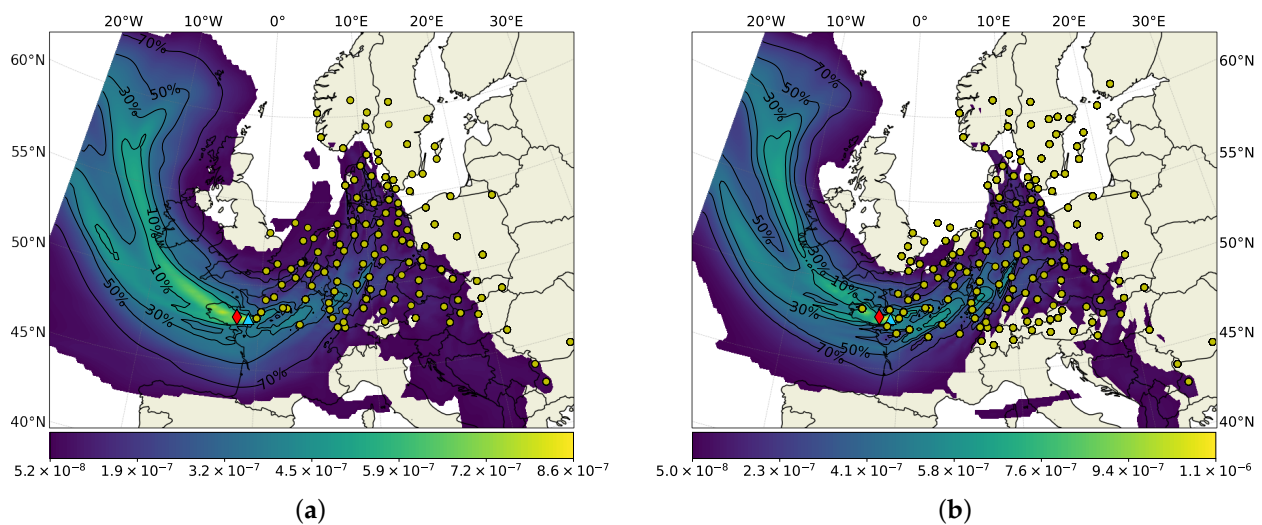
Figure 1. Marginal posterior probability distribution for release location for ETEX in units of km^{-2}. The blue triangle shows the location of highest probability density, the red diamond shows the actual release location, and the yellow circles show the locations of the sampling stations. The results are based on the set of three-hour measurements. (**a**) is based on non-zero measurements only, while (**b**) is the result when including non-detections. A zoom of the area near the maximum probability is shown in Figure 2.

Table 1. List of locations of maximum probability for the different versions of the ETEX dataset. The table also shows the distance to the true release site.

Data Set	Coordinates for Location of Maximum Probability	Distance to True Release Site
3 h measurements excluding non-detections	48.0° N, 1.0° W	75 km
3 h measurements all measurements	48.0° N, 1.0° W	75 km
12 h measurements all measurements	48.0° N, 0.75° W	94 km
24 h measurements all measurements	48.0° N, 0.75° W	94 km
24 h measurements excluding data within 200 km	47.75° N, 2.5° W	50 km
24 h measurements excluding data within 400 km	46.5° N, 0.25° W	218 km
24 h measurements excluding data within 800 km	47.0° N, 1.5° W	123 km

Figure 2 shows the same results as in Figure 1, only for a smaller geographical area. Here, it is easier to see that the probability is generally high in the area close to the true release location. Further, comparison of the two figures clearly indicates the added effects of the non-detections: the result in Figure 2b is based on more sampling stations (more yellow circles) than the result in Figure 2a. Associated with several of these added sampling stations, there are areas of lower probability upstream from the measurement station, e.g., the stations north east and south east of the release location.

Finally, it is worth noticing that, in both figures, the sharp peaks of the probability distributions are located near the sampling station in Rennes (the yellow circle directly east of the estimated release location). Examining the dataset, it was discovered that this sampling station measured the highest values in the dataset, which emphasizes the importance of testing the sensitivity to measurements close to the source location.
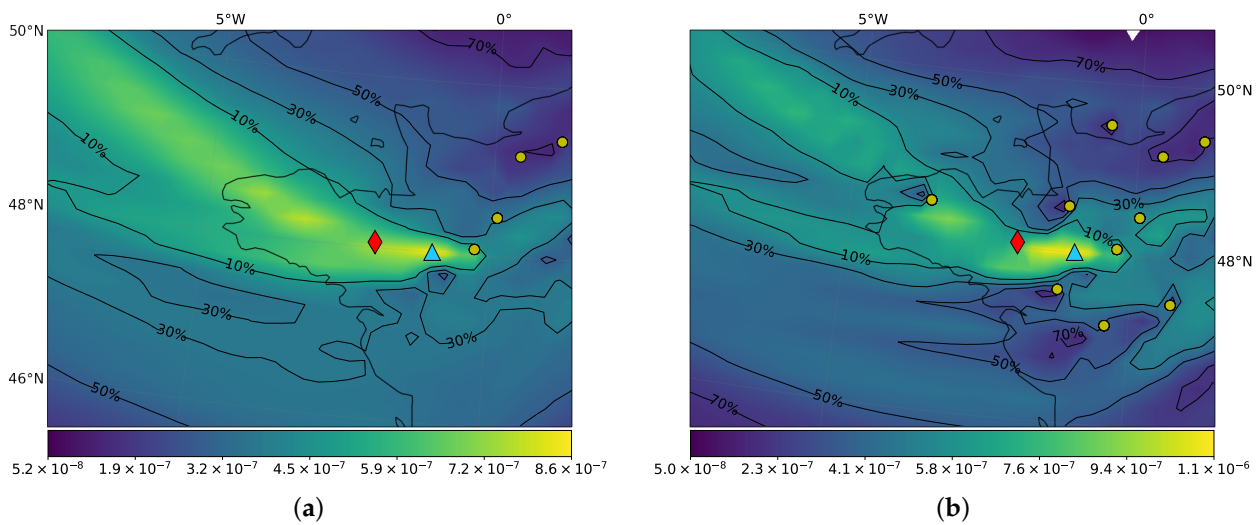
3.1. PAPER 1: PROBABILISTIC INVERSE METHOD FOR SOURCE LOCALIZATION APPLIED TO ETEX AND THE 2017 CASE OF RU-106 INCLUDING ANALYSES OF SENSITIVITY TO MEASUREMENT DATA

Figure 2. Marginal posterior probability distribution for release location for ETEX in units of km^{-2}. The blue triangle shows the location of highest probability density, the red diamond shows the actual release location, and the yellow circles show the locations of the sampling stations. The results are based on the set of three-hour measurements. (**a**) is based on non-zero measurements only, while (**b**) is the result when including non-detections. The probability distributions are identical to those shown in Figure 1 but for a smaller geographical area.

3.1.1. Sensitivity Analyses

Now, the sampling periods are deliberately extended to 12 and 24 h, as described in Section 2.1. In both cases, non-detections are included. The resulting probability distributions are shown in Figure 3, and to make comparison easier, the same geographical area as in Figure 2 is used. Thus, Figures 2b and 3a,b show the results based on measurements of 3, 12 and 24 h, respectively. As one might expect, the coarser time resolutions result in wider, less accurate, probability distributions. Nonetheless, all three distributions have the area of maximum probability in the same general area, indicating that even 24 h average concentrations are useful for source localization.

Figure 3. Marginal posterior probability distribution for release location for ETEX in units of km^{-2}. The blue triangle shows the location of highest probability density, the red diamond shows the actual release location, and the yellow circles show the locations of the sampling stations. The results are based on both non-zero measurements and non-detections. (**a**) is based on 12-h measurements, while (**b**) is based on 24-h measurements.

Figure 4 shows the results based on the 24-h measurements, where in Figure 4b–d, measurements within a radius of 200, 400, and 800 km of the release location, respectively,

are excluded from the dataset. The resulting probability distribution strongly depends on the distance from the release site to the nearest measurements: the precision of the source localization gradually decreases as measurements are removed from the dataset, i.e., the peak of the distribution becomes less sharp. The location of maximum probability, on the other hand, is closest to the true release site for the dataset, where measurements within a radius of 200 km are excluded, see Table 1. This may be a coincidence, or it may be explained by the fact that the measurement station in Rennes dominates the localization when these measurements are included.
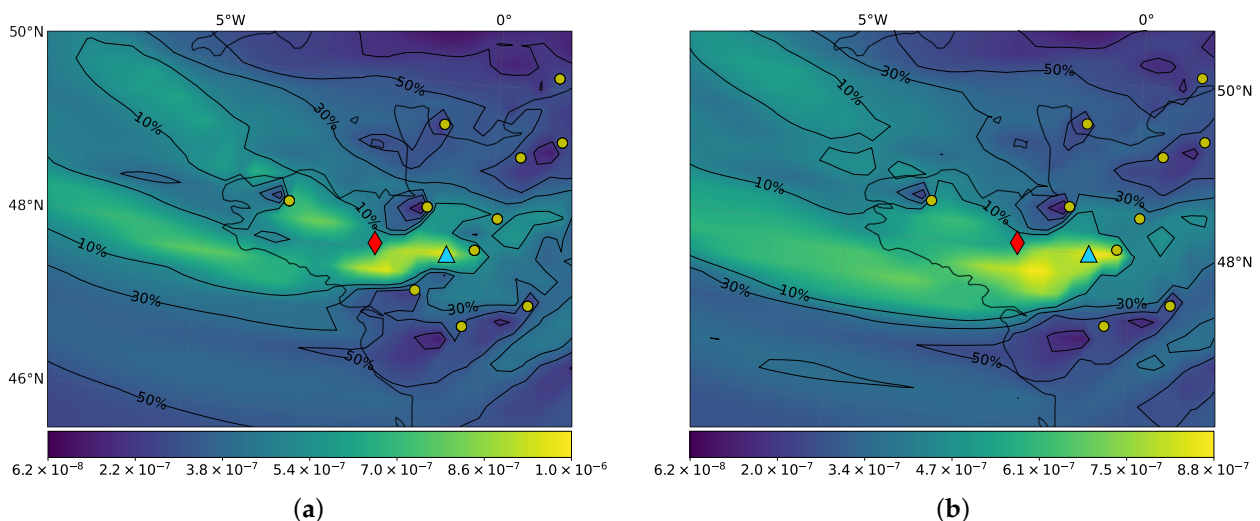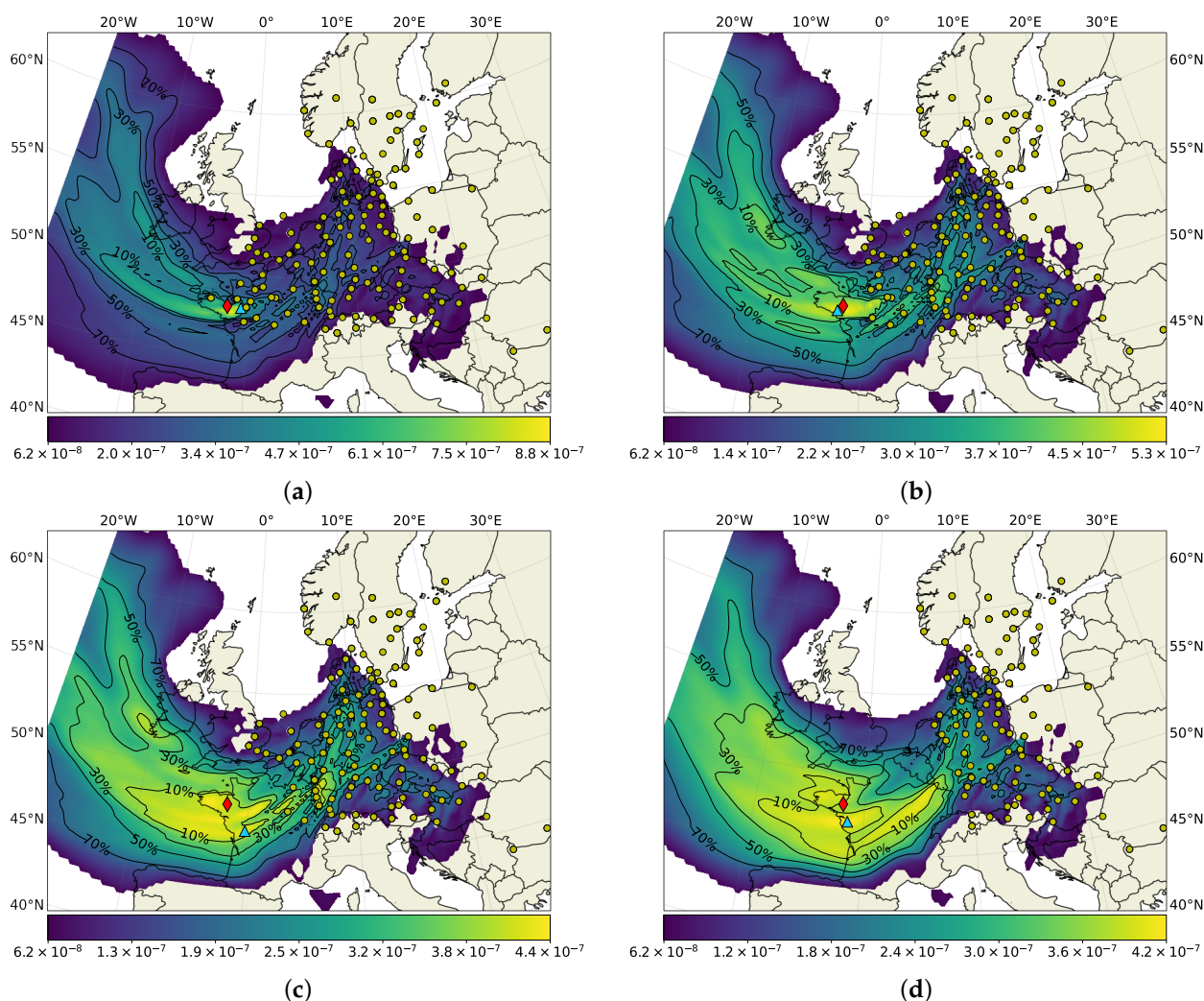

Figure 4. Marginal posterior probability distribution for release location for ETEX in units of km^{-2}. The blue triangle shows the location of highest probability density, the red diamond shows the actual release location, and the yellow circles show the locations of the sampling stations. The results are based on the 24 h measurements and include both non-zero measurements and non-detections. (**a**) is based on all measurements, (**b**) is the result when excluding measurements within a radius of 200 km from the source, (**c**) is the result when excluding measurements within a radius of 400 km from the source, and (**d**) is the result when excluding measurements within a radius of 800 km from the source.

For all four probability distributions, the true source location is located well within the 30% HDR, and only in one case, Figure 4d, the true source is located just outside, almost at border, of the 10% HDR. This indicates that, rather than considering the location of maximum probability, one should consider, e.g., the 10% HDR and combine this with independent information about possible release site candidates, if such exists.

3.1. PAPER 1: PROBABILISTIC INVERSE METHOD FOR SOURCE LOCALIZATION APPLIED TO ETEX AND THE 2017 CASE OF RU-106 INCLUDING ANALYSES OF SENSITIVITY TO MEASUREMENT DATA

3.1.2. Time and Magnitude of the Release

Determining the most likely release period and the amount of released material can be approached in different ways. One option is to consider the two-dimensional marginal posterior distribution $P(t_{start}, \Delta t_{release} | \mathbf{y}, I)$. However, the start time and duration vary significantly with the release location considered. Therefore, instead, the two-dimensional conditional posterior distribution $P(t_{start}, \Delta t_{release} | \mathbf{y}, \mathbf{x}_{release}, I)$ is considered for the most likely release sites. In case no information about possible release sites exist, the best estimate of the source location would be the location of maximum probability. However, if we imagine that ETEX was a nuclear accident, it would most likely be possible to obtain a list of nuclear facilities within the 10% HDR, which could be used to suggest one or a few concrete source locations. Thus, for the ETEX case, the time and magnitude of the release will simply be evaluated for the true release site.

The resulting conditional posterior distribution is shown in Figure 5a using the dataset of three-hour measurements, and in Figure 6a, using the dataset of 24 h measurements, where measurements within a radius of 800 km are excluded. In both figures, the 25, 50, and 75% HDRs are plotted together with the probability densities. Further, based on all release periods within the 50% HDR, the distribution of $\hat{q}\Delta t_{release}$, i.e., the time integrated release, is estimated and shown in Figures 5b and 6b, where the values of $\hat{q}$ are estimated using Equation (18). Since the amount of released material may vary several orders of magnitude, the logarithm of the time integrated release is considered.

According to the result shown in Figure 5a, the most likely release started on 23 October 1994 at 18.00 UTC and lasted six hours, which is two hours after the true release started and half the duration. However, both the 25% and 50% HDR indicate that releases that start earlier but have a longer duration have almost similar probabilities. The same pattern, only more pronounced, is seen in in Figure 6a, where an even larger area of the parameter space have almost the same probability. This is expected, since this result is based on the dataset with the coarser time resolution and without measurements within the first 800 km. In both cases, the true release is located inside the 50% HDR, and hence, this is interpreted as the best possible estimate of the release period.

(a)	(b)

Figure 5. Time and magnitude of the release based on the true release site. The blue triangles show the most likely release, and the red diamond shows the true release. (**a**) Marginal posterior probability distribution for start time and duration for ETEX in units of h^{-2}. The result is based on the set of three-hour measurements. (**b**) Probability distribution for time integrated release based on the start times and durations within the 50% HDR of the result in (**a**).
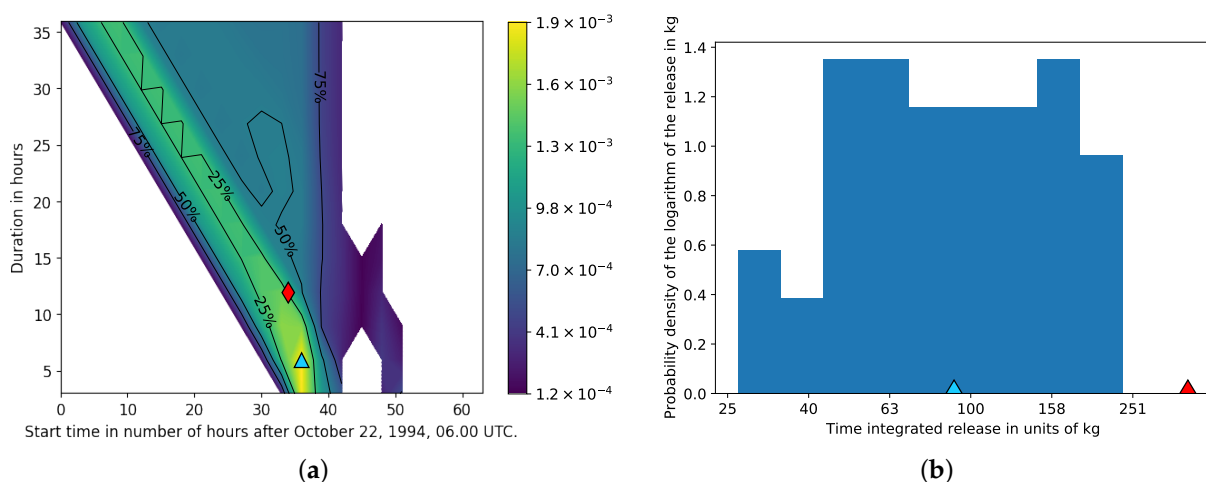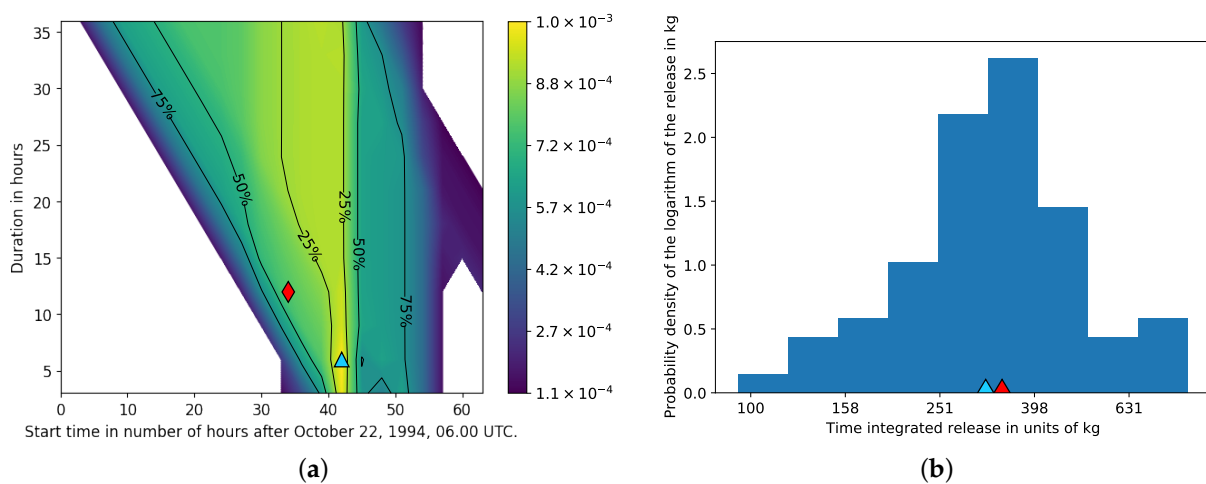
Figure 6. Time and magnitude of the release based on the true release site. The blue triangles show the most likely release, and the red diamond shows the true release. (**a**) Marginal posterior probability distribution for start time and duration for ETEX in units of h^{-2}. The result is based on the set of 24 h measurements, where measurements within a radius of 800 km are excluded. (**b**) Probability distribution for time integrated release based on the start times and durations within the 50% HDR of the result in (**a**).

Surprisingly, the probability distributions for the logarithm of the time integrated release rates, Figures 5b and 6b, indicate that the second dataset, where the data quality has been reduced, gives a better prediction of the magnitude of the release. The probability distribution in Figure 5b predicts a release between 30 and 240 kg, with the most likely release being 90 kg. In comparison, the true release is 340 kg, which is of the same order of magnitude as the largest estimated releases but not included in the predicted interval. The probability distribution in Figure 6b, on the other hand, predicts a release between 90 and 840 kg with the most likely release being 310 kg. As mentioned previously, examination of the dataset showed that the measurement station in Rennes had measured the highest values in the dataset and that this measurement station seems to dominate the resulting probability distribution, see Section 3.1. It is, therefore, possible that the estimate of $\hat{q}$ in Figure 5b is also dominated by a few measurements close to the source, which may make it less robust than the estimate of $\hat{q}$ in Figure 6b.

3.2. Application to the Ru-106 Case

The two-dimensional marginal distributions for the release location, shown in Figures 7 and 8, are obtained by first applying Equation (17) and then Equation (19). Figure 7 shows the result based on all Ru-106 measurements, while Figure 8 shows the results based on two different sub-datasets: Figure 8a shows the result based on measurements of up to 36 h, of which the majority are either 12-h or 24-h averages, and Figure 8b shows the result based on measurements of more than 36 h, of which the majority are weekly averages (see Section 2.2 for details). Further, Table 2 shows the coordinates for the location of maximum probability as well as the distance from this location to the NIIAR and Mayak nuclear facilities, respectively.

The results in both Figures 7 and 8a show areas of high probability near the Mayak nuclear facility, which is located within the 10% HDR. In both cases, the NIIAR nuclear facility is located only just inside the 50% HDR. Assuming that the HDRs can be interpreted as in the ETEX case, Section 3.1, we would expect the true source location to be located inside or at least close to 10% HDR. Therefore, we conclude that Mayak is the most likely release site.

The 10% HDR of the probability distribution based on long-period measurements only, Figure 8b, extends further to the north and does not contain Mayak. However, Mayak is located just outside the 10% HDR, whereas NIIAR is only included in the 50% HDR. Hence, this result also indicates that the Mayak nuclear facility is the most likely release site.
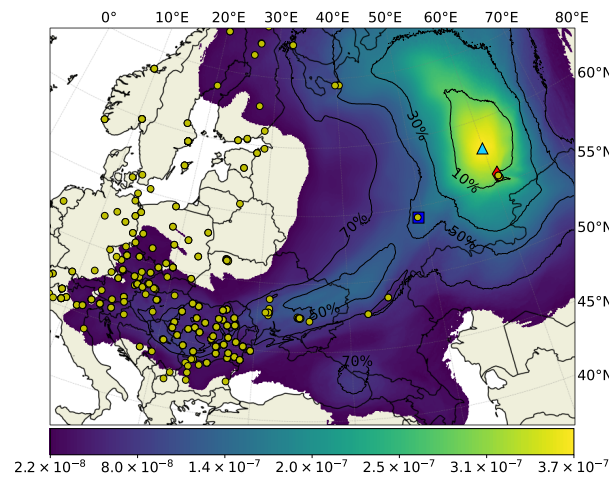
3.1. PAPER 1: PROBABILISTIC INVERSE METHOD FOR SOURCE LOCALIZATION APPLIED TO ETEX AND THE 2017 CASE OF RU-106 INCLUDING ANALYSES OF SENSITIVITY TO MEASUREMENT DATA

Figure 7. Marginal posterior probability distribution for the Ru-106 case in units of km^{-2}. The blue triangle shows the location of highest probability density, the red diamond shows the location of the Mayak nuclear facility, the blue square shows the location of the NIIAR nuclear facility, and the yellow circles show the locations of the sampling stations. The result is based on all non-zero measurements and non-detections.

| (a) | (b) |
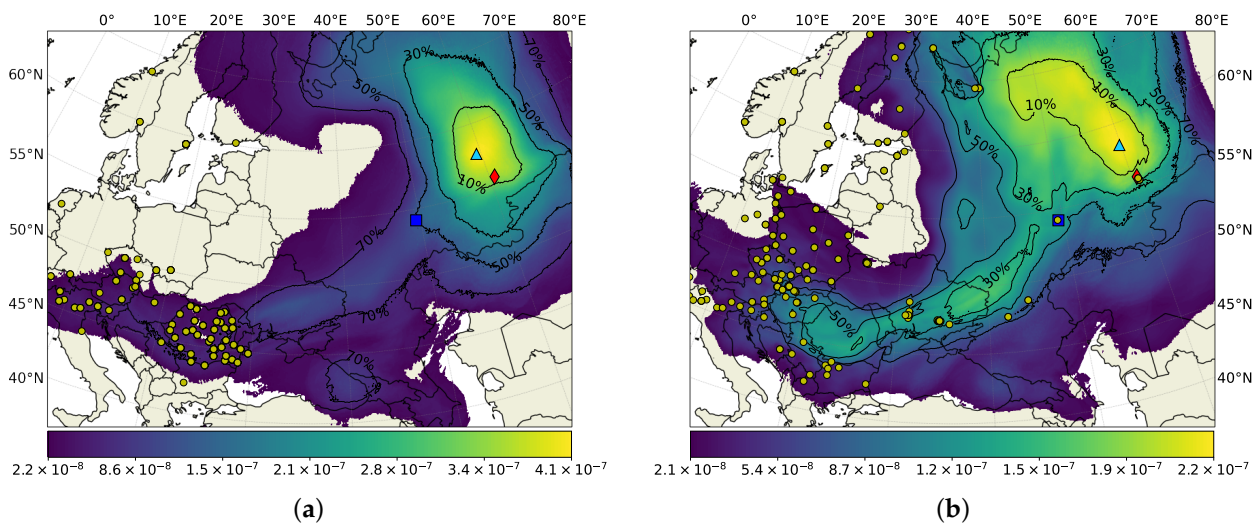
Figure 8. Marginal posterior probability distribution for the Ru-106 case in units of km^{-2}. The blue triangle shows the location of highest probability density, the red diamond shows the location of the Mayak nuclear facility, the blue square shows the location of the NIIAR nuclear facility, and the yellow circles show the locations of the sampling stations. (**a**) the result is based on all non-zero measurements and non-detections, both up to 36 h. (**b**) the result is based on all non-zero measurements and non-detections, both more than 36 h.

Table 2. List of locations of maximum probability for the different versions of the Ru-106 dataset. The table also shows the distance to the Mayak and NIIAR nuclear facilities.

Data Set	Coordinates for Location of Maximum Probability	Distance to Mayak	Distance to NIIAR
All measurements	57.9° N, 60.0° E	241 km	771 km
Measurements conducted over up to 36 h	57.8° N, 59.4° E	239 km	735 km
Measurements conducted over more than 36 h	58.4° N, 59.9° E	296 km	794 km

Time and Magnitude of the Release

The release period is estimated by considering the conditional posterior distribution $P(t_{\text{start}}, \Delta t_{\text{release}} | \mathbf{x}_{\text{release}})$ based on the most likely release site. Further, as described in Section 3.1.2, the amount of released material is estimated by considering the distribution of $\hat{q} \Delta t_{\text{release}}$ based on all release periods within the 50% HDR. Again, the values of $\hat{q}$ are estimated using Equation (18). Assuming that the Mayak nuclear facility is the release site, we obtain the conditional posterior distribution $P(t_{\text{start}}, \Delta t_{\text{release}} | \mathbf{x}_{\text{release}})$ shown in Figure 9.

The result in Figure 9a indicates that the release started between 23 September 2017 around 18.00 UTC and 26 September 2017 at 15.00 UTC and lasted between 3 and 36 h; generally, earlier releases (before September 00.00 UTC) would be of longer duration. In fact, the probability distribution has at least three local maxima: one on 24 September around 00.00 UTC, one on 25 September around 08.00 UTC, and one on 26 September around 02.00 UTC. This may indicate that the release possibly consisted of a few different release periods, which has also been hypothesized by Saunier et al. [9]. However, since the source term model only allows for constant releases within a single time interval, the probability of the combination of two release periods is not considered explicitly, and hence this hypothesis cannot be tested with our method. The 50% HDR covers quite a large area of the parameter space, and it is therefore difficult to estimate the release time and duration more accurately than this.

The probability distribution for the logarithm of the time integrated release rate, Figure 9b, predicts a release between approximately 210 and 1600 TBq, with the most likely release being 620 TBq, which is in accordance with the estimates of other studies [5,9,10,14]. The probability distribution also allows for a release that is significantly larger, up to about 8250 TBq, although this is in unlikely scenario. By comparison with the distribution $P(t_{\text{start}}, \Delta t_{\text{release}} | \mathbf{x}_{\text{release}})$ in Figure 9a, it is likely that this option of a much larger release is related to the possibility of an early release, i.e., 23–24 September.

(a)   **(b)**
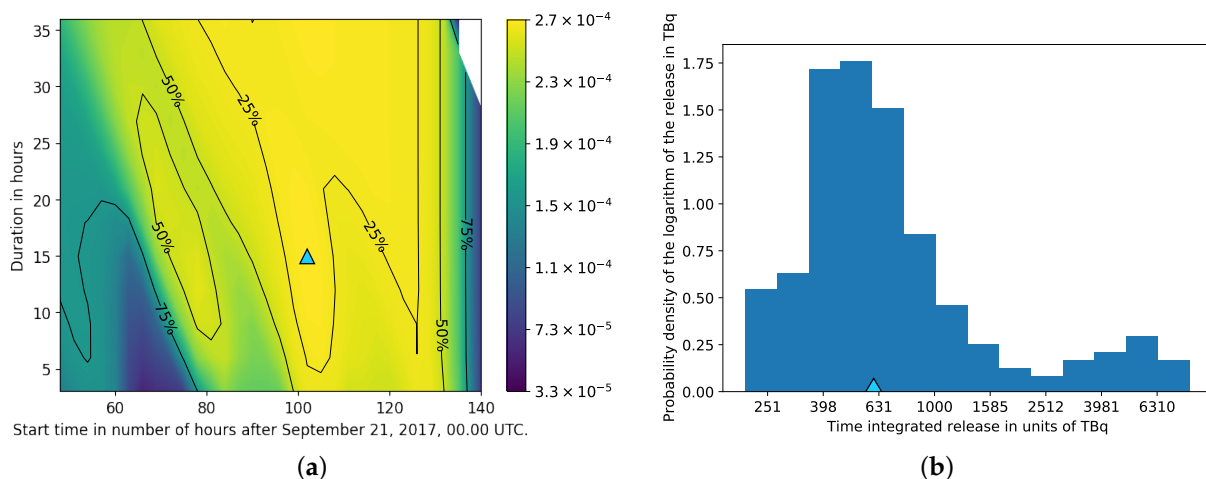
Figure 9. Time and magnitude of the release based on the location of the Mayak nuclear facility. The blue triangles show the most likely release. (**a**) Marginal posterior probability distribution for start time and duration for the Ru-106 case in units of h^{-2}. The result is based on all measurements, i.e., also including measurements conducted over more than 36 h. (**b**) Probability distribution for time integrated release based on the start times and durations within the 50% HDR of the result in (**a**).

4. Summary and Conclusions

The methodology combines the adjoint source–receptor relationship with a simplified Bayesian approach and a correlation-based probability measure. This provides an efficient way to obtain an estimate of the four-dimensional probability distribution for latitude, longitude, start time, and duration of a release, based on the assumption that the release rate is constant during the release period. The two-dimensional probability distribution for the source location is then obtained by marginalization.

3.1. PAPER 1: PROBABILISTIC INVERSE METHOD FOR SOURCE LOCALIZATION
APPLIED TO ETEX AND THE 2017 CASE OF RU-106 INCLUDING ANALYSES OF SEN-
SITIVITY TO MEASUREMENT DATA

The validation against ETEX shows that the methodology yields an accurate source localization when applied to the entire set of three-hour measurements; in this case, the location of maximum probability is 75 km downstream from the true source location, and the latter is located well within the 10% HDR. When excluding measurements close to the source or extending the measurement intervals, the width of the probability distribution is increased, but the area of high probability, e.g., the 10% or 30% HDR, still contains the true release site. The exact location of maximum probability, on the other hand, depends less systematically on these parameters, cf. Table 1, indicating that this measure is not useful alone but should be interpreted in combination with the 10% HDR. Thus, since the location of the maximum probability does not necessarily coincide with the true source location, a more robust interpretation of the result is to consider a larger area of high probability, such as the 10% HDR, and combine this result with information about possible release sites in the area to be able to suggest concrete source locations.

For a suggested release site, the start time and duration of the release is estimated by considering the conditional posterior distribution. When evaluating the conditional posterior distribution for the true source location in the ETEX case, a rough estimate of the start time and duration of the release is obtained. The methodology does not accurately pinpoint the correct release period but rather gives an interval of possible start times and durations. For the ETEX case, this means that releases of 3 to 36 h duration are possible, with the starting times ranging from 22 October 1994 around 10–15 UTC until approximately 32 h later. Thus, this method may not necessarily be ideal for accurately estimating the release period.

An estimate of the magnitude of the release is obtained by considering the distribution of the logarithm of the time-integrated release. For the ETEX case, the estimate is better when excluding the measurements close to the source. This may be related to the fact that the estimated optimal release rate is dominated by fewer data points with high values, when the measurements close to the source are included. As described in Section 2.6.1, the implication of setting $\sigma_i =$ constant is that measurements of higher values dominate the estimate of $\hat{q}$, which is likely to explain why the magnitude of the release is better estimated when excluding these measurements. However, a more thorough analysis of this is needed in order to reach a conclusion. For the two different versions of the ETEX datasets considered, the source was estimated between 30 and 240 kg and between 90 and 840 kg, respectively. In both cases, the interval of estimated releases includes values of the roughly the same order of magnitude as true release, 340 kg.

Further, the non-detections are included in the dataset by assuming that these are measurements of zero concentration, though they can be non-zero concentrations below the detection limit. The results show that the non-detections do add information, e.g., by locally decreasing the probability in areas upstream from measurement stations that only measured concentrations below the detection limit. However, the result is quite similar to that based on the dataset of only non-zero measurements. This indicates that, for the case considered, non-detections are not crucial for source localization, but they should be included if they exist.

The methodology is then applied to the Ru-106 case using three different datasets: the first including all measurements that fulfill the quality control requirements described in Section 2.2, the second only including measurements conducted over up to 36 h, and the third only including measurements conducted over more than 36 h. The result based on the first two datasets are almost indistinguishable by visual comparison. The third share similar features, but the 10% HDR is shifted towards north and covers a larger geographical area. However, despite these differences, the method proves to be robust, since the three datasets lead to the same overall conclusion. The two-dimensional marginal probability distribution for the location indicates that the Southern Ural region is the most plausible release area. By comparison of the 10% HDR and previously suggested release sites, we conclude that the most likely release site is the Mayak nuclear facility. Based on this assumption, the results indicate that the release started between 23 September 2017

at 18.00 UTC and 26 September 2017 at 15.00 UTC and lasted between 3 and 36 h. Finally, the magnitude of the release is estimated between 210 and 1600 TBq, with the most likely release being 620 TBq.

The main objective of this study was to develop a robust and efficient method suitable for operational use. The simplifications made allow for efficient evaluation of the probability, while the correlation-based probability measure provides a robust way of comparing measurements and model results despite the potentially large, unknown modelling errors. Through various sensitivity analyses, it has been demonstrated that the methodology yields useful results, even when the information contained in the dataset is reduced.

Author Contributions: Conceptualization, K.S.T., E.K. and J.H.S.; methodology, K.S.T. and J.H.S.; software, K.S.T.; validation, K.S.T. formal analysis, K.S.T.; investigation, K.S.T.; writing—original draft preparation, K.S.T.; writing—review and editing, K.S.T., E.K. and J.H.S.; visualization, K.S.T.; supervision, E.K. and J.H.S.; funding acquisition, K.S.T., E.K. and J.H.S. All authors have read and agreed to the published version of the manuscript.

Institutional Review Board Statement: Not applicable.

Informed Consent Statement: Not applicable.

Data Availability Statement: The ETEX observation dataset is published by Nodop et al. [17]. The Ru-106 observation dataset is described and made publicly available in the work of Masson et al. [18]. The ERA5 dataset is available via the https://www.ecmwf.int/en/forecasts/datasets/reanalysis-datasets/era5 (accessed on 13 October 2021).

Conflicts of Interest: The authors declare no conflict of interest.

Abbreviations

The following abbreviations are used in this manuscript:

DERMA	Danish Emergency Response Model of the Atmophere
PBL	Planetary Boundary Layer
ETEX	European Tracer Experiment
ECMWF	European Centre for Medium-Range Weather Forecasts
PMCH	Perfluoromethylcyclohexane
HDR	High Density Region

References

1. Pudykiewicz, J.A. Application of adjoint tracer transport equations for evaluating source parameters. *Atmos. Environ.* **1998**, *32*, 3039–3050. [CrossRef]
2. Wotawa, G.; De Geer, L.E.; Denier, P.; Kalinowski, M.; Toivonen, H.; D'Amours, R.; Desiato, F.; Issartel, J.P.; Langer, M.; Seibert, P.; et al. Atmospheric transport modelling in support of CTBT verification—Overview and basic concepts. *Atmos. Environ.* **2003**, *37*, 2529–2537. [CrossRef]
3. Seibert, P. Methods for source determination in the context of the CTBT radionuclide monitoring system. In Proceedings of the Informal Workshop on Meteorological Modelling in Support of CTBT Verification, Vienna, Austria, 4–6 December 2000; pp. 1–6.
4. Seibert, P.; Frank, A.; Kromp-Kolb, H. Inverse modelling of atmospheric trace substances on the regional scale with Lagrangian models. In Proceedings of the EUROTRAC-2 Symposium, Garmisch-Partenkirchen, Germany, 11–15 March 2002; pp. 11–15.
5. Sørensen, J.H. Method for source localization proposed and applied to the October 2017 case of atmospheric dispersion of Ru-106. *J. Environ. Radioact.* **2018**, *189*, 221–226. [CrossRef] [PubMed]
6. Keats, A.; Yee, E.; Lien, F.S. Bayesian inference for source determination with applications to a complex urban environment. *Atmos. Environ.* **2007**, *41*, 465–479. [CrossRef]
7. Yee, E.; Lien, F.S.; Keats, A.; D'Amours, R. Bayesian inversion of concentration data: Source reconstruction in the adjoint representation of atmospheric diffusion. *J. Wind Eng. Ind. Aerodyn.* **2008**, *96*, 1805–1816. [CrossRef]
8. Yee, E.; Hoffman, I.; Ungar, K. Bayesian Inference for Source Reconstruction: A Real-World Application. *Int. Sch. Res. Not.* **2014**, *2014*, 12. [CrossRef]
9. Saunier, O.; Didier, D.; Mathieu, A.; Masson, O.; Le Brazidec, J.D. Atmospheric modeling and source reconstruction of radioactive ruthenium from an undeclared major release in 2017. *Proc. Natl. Acad. Sci. USA* **2019**, *116*, 24991–25000. [CrossRef] [PubMed]

10. Le Brazidec, J.D.; Bocquet, M.; Saunier, O.; Roustan, Y. MCMC methods applied to the reconstruction of the autumn 2017 Ruthenium-106 atmospheric contamination source. *Atmos. Environ. X* **2020**, *6*, 100071. [CrossRef]

11. Efthimiou, G.C.; Kovalets, I.V.; Venetsanos, A.; Andronopoulos, S.; Argyropoulos, C.D.; Kakosimos, K. An optimized inverse modelling method for determining the location and strength of a point source releasing airborne material in urban environment. *Atmos. Environ.* **2017**, *170*, 118–129. [CrossRef]

12. Kovalets, I.V.; Efthimiou, G.C.; Andronopoulos, S.; Venetsanos, A.G.; Argyropoulos, C.D.; Kakosimos, K.E. Inverse identification of unknown finite-duration air pollutant release from a point source in urban environment. *Atmos. Environ.* **2018**, *181*, 82–96. [CrossRef]

13. Kovalets, I.V.; Romanenko, O.; Synkevych, R. Adaptation of the RODOS system for analysis of possible sources of Ru-106 detected in 2017. *J. Environ. Radioact.* **2020**, *220*, 106302. [CrossRef] [PubMed]

14. Tomas, J.M.; Peereboom, V.; Kloosterman, A.; van Dijk, A. Detection of radioactivity of unknown origin: Protective actions based on inverse modelling. *J. Environ. Radioact.* **2021**, *235*, 106643. [CrossRef] [PubMed]

15. Sørensen, J.H.; Klein, H.; Ulimoen, M.; Robertson, L.; Pehrsson, J.; Lauritzen, B.; Bohr, D.; Hac-Heimburg, A.; Israelson, C.; Buhr, A.M.B.; et al. *NKS-430: Source Localization by Inverse Methods (SLIM)*; Technical Report; Nordic Nuclear Safety Research (NKS): Roskilde, Denmark, 2020.

16. Graziani, G.; Klug, W.; Mosca, S. *Real-Time Long-Range Dispersion Model Evaluation of the ETEX First Release*; Office for Official Publications of the European Communities: Luxembourg, 1998.

17. Nodop, K.; Connolly, R.; Girardi, F. The field campaigns of the European Tracer Experiment (ETEX): Overview and results. *Atmos. Environ.* **1998**, *32*, 4095–4108. [CrossRef]

18. Masson, O.; Steinhauser, G.; Zok, D.; Saunier, O.; Angelov, H.; Babić, D.; Bečková, V.; Bieringer, J.; Bruggeman, M.; Burbidge, C.; et al. Airborne concentrations and chemical considerations of radioactive ruthenium from an undeclared major nuclear release in 2017. *Proc. Natl. Acad. Sci. USA* **2019**, *116*, 16750–16759. [CrossRef] [PubMed]

19. Hersbach, H.; Bell, B.; Berrisford, P.; Hirahara, S.; Horányi, A.; Muñoz-Sabater, J.; Nicolas, J.; Peubey, C.; Radu, R.; Schepers, D.; et al. The ERA5 global reanalysis. *Q. J. R. Meteorol. Soc.* **2020**, *146*, 1999–2049. [CrossRef]

20. PartIII: Dynamics and Numerical Procedures. In *IFS Documentation CY47R1*; IFS Documentation, ECMWF: Reading, UK, 2020.

21. Sørensen, J.H. Sensitivity of the DERMA long-range Gaussian dispersion model to meteorological input and diffusion parameters. *Atmos. Environ.* **1998**, *32*, 4195–4206. [CrossRef]

22. Sørensen, J.H.; Baklanov, A.; Hoe, S. The Danish emergency response model of the atmosphere (DERMA). *J. Environ. Radioact.* **2007**, *96*, 122–129. [CrossRef] [PubMed]

23. Marchuk, G.; Shutyaev, V.; Bocharov, G. Adjoint equations and analysis of complex systems: Application to virus infection modelling. *J. Comput. Appl. Math.* **2005**, *184*, 177–204. [CrossRef]

24. Hyndman, R.J. Computing and graphing highest density regions. *Am. Stat.* **1996**, *50*, 120–126.

3.1. PAPER 1: PROBABILISTIC INVERSE METHOD FOR SOURCE LOCALIZATION APPLIED TO ETEX AND THE 2017 CASE OF RU-106 INCLUDING ANALYSES OF SENSITIVITY TO MEASUREMENT DATA

3.2 Paper 2: Bayesian Inverse Modelling for Probabilistic Multi-Nuclide Source Term Estimation Using Observations of Air Concentration and Gamma Dose Rate

The article (Tølløse and Sørensen, 2022) describes a method developed for source term estimation in case of nuclear power plant accidents. After the Chernobyl disaster in 1986, long-range dispersion models have been developed to predict the dispersion of radioactive particles and gasses in case of a similar accident. In March 2011, the Fukushima Daiichi nuclear power plant experienced a loss of electricity, after it was hit by a tsunami. This caused the cooling systems for three of the power plant's six reactors to stop working, which eventually resulted in damaged reactor cores, several hydrogen explosions, and large amounts of radioactive matter released to the atmosphere (Koo et al., 2014). In addition, the loss of electricity meant that the in-plant monitoring systems were shut down. Thus, with no measurements available to provide reliable information about the release, any simulations made in real-time were associated with large uncertainties. Afterward, inverse methods have been used to estimate the source term (Winiarek et al., 2012; Stohl et al., 2012; Saunier et al., 2013; Liu et al., 2017; Terada et al., 2020). However, the methods developed in these studies may not be suitable for real-time use in case of a future accident.

This issue was addressed by Saunier et al. (2020), who refined their method specifically for deployment during the early stages of an accident. In 2022 and 2023, the DMI-organized international research project SOurce CHAracterizatiOn accounting for meTeorologIcal unCertainties (SOCHAOTIC) also targeted this problem (Sørensen et al., 2023). To be able to evaluate the developed methods, an artificial core melt event from the Loviisa nuclear power plant in southern Finland was considered.

The method described in this article is intended for source term estimation at the early stages of an accident, inspired by Saunier et al. (2020). However, the novelty of this study is to use a probabilistic inversion method to be able to quantify the uncertainties of the estimated source term. The method is applied to the artificial Loviisa case, using the same meteorological data, dispersion model, and gamma dose rate model for both the construction of the observation data and for the source term estimation. Hence, the article showcases the method in an idealized scenario, where model uncertainties are negligible.

As DMI's contribution to the SOCHAOTIC project, this method was applied to a few additional cases, most importantly, to the same artificial Loviisa case but where the measurement data set is created using different meteorological forecast data, as well as a different dispersion model and gamma dose rate model. Thus, this study demonstrates the performance of the method under more realistic conditions where model uncertainties are no longer negligible. Selected results from the SOCHAOTIC report are presented in Chapter 3.3.

3.2.   PAPER 2: BAYESIAN INVERSE MODELLING FOR PROBABILISTIC MULTI-NUCLIDE SOURCE TERM ESTIMATION USING OBSERVATIONS OF AIR CONCEN-TRATION AND GAMMA DOSE RATE

Bayesian Inverse Modelling for Probabilistic Multi-Nuclide Source Term Estimation Using Observations of Air Concentration and Gamma Dose Rate

Kasper Skjold Tølløse [1,2,*] and **Jens Havskov Sørensen** [1]

1   Danish Meteorological Institute, DK-2100 Copenhagen, Denmark
2   Niels Bohr Institute, University of Copenhagen, DK-2100 Copenhagen, Denmark
*   Correspondence: ktoe@dmi.dk

Abstract: In case of a release of hazardous radioactive matter to the atmosphere from e.g., a nuclear power plant accident, atmospheric dispersion models are used to predict the spatial distribution of radioactive particles and gasses. However, at the early stages of an accident, only limited information about the release may be available. Thus, there is a need for source term estimation methods suitable for operational use shortly after an accident. We have developed a Bayesian inverse method for estimating the multi-nuclide source term describing a radioactive release from a nuclear power plant. The method provides a probabilistic source term estimate based on the early available observations of air concentration and gamma dose rate by monitoring systems. The method is intended for operational use in case of a nuclear accident, where no reliable source term estimate exists. We demonstrate how the probabilistic formulation can be used to provide estimates of the released amounts of each radionuclide as well as estimates of future gamma dose rates. The method is applied to an artificial case of a radioactive release from the Loviisa nuclear power plant in southern Finland, considering the most important dose-contributing nuclides. The case demonstrates that only limited air concentration measurement data may be available shortly after the release, and that to a large degree one will have to rely on gamma dose rate observations from a frequently reporting denser monitoring network. Further, we demonstrate that information about the core inventory of the nuclear power plant can be used to constrain the release rates of certain radionuclides, thereby decreasing the number of free parameters of the source term.

Keywords: source characterization; atmospheric dispersion modelling; inverse modelling; Bayesian inference

1. Introduction

In case of a nuclear accident, radioactive particles and gasses may be released to the atmosphere. Consequently, an important part of emergency preparedness is to run simulations with atmospheric dispersion models, thereby predicting the atmospheric distribution as well as deposition of radioactive particles and gasses on the surface of the Earth. However, such models are subject to a number of uncertainties, the most important being the uncertainties of the meteorological predictions, inaccurate physics parameterizations in the dispersion model, and uncertainties of the estimated source term. Immediately after an accident in a nuclear power plant, only limited information about the release may be available. Thus, at the early stages of the accident, the dominating source of uncertainty is most likely the source term. If this is the case, inverse modelling can be used to obtain a source term estimate, which in turn can be used for running the atmospheric dispersion model. The aim of this study is to develop an inverse method for source term estimation, which is suited for operational use for emergency preparedness at the early stages of an accident, i.e., providing a source term estimate based on the limited data available shortly after the accident.

In the early phase of a nuclear power plant accident, a limited number of air concentration observations will be available, and these will typically have a low spatial and temporal resolution, e.g., the filters in such measurement stations may be changed every 24 h or even less frequently. In addition, there may exist gamma dose rate observations at much higher resolution, both spatially and temporally. However, since such measurements are the sum of contributions from all the different radionuclides, it is not clear a priori if they are useful for source term estimation.

Previous studies have used inverse methods for source term estimation. Lately, the still unaccounted for release of Ru-106 in the fall of 2017, was subject to several studies, e.g., [1–4]. However, since the release location has still not been confirmed, the main focus of these studies is localization of the source. The Fukushima Daiichi nuclear disaster in 2011, on the other hand, demonstrated that in-plant monitoring systems may not be working during a severe accident. Thus, different inverse methods have been applied in order to assess the source term. Some studies have estimated the release of certain radionuclides based solely on air concentration measurements [5,6], other include surface deposition measurements [7,8], while other again also include gamma dose rates [9]. Saunier et al. [9] demonstrate that information about ratios between the amounts of certain radionuclides can be used to further constrain the release rates. They use a variational approach to assess the source term, thereby providing a deterministic estimate. However, by using different Bayesian approaches, Liu et al. [6] show that significant uncertainties are associated with the estimated source term, indicating that probabilistic methods are better suited for this type of problem.

Most previous studies in this field aim at estimating the source term associated with accidents a long time after they occurred. However, for emergency preparedness, it is also important to be able to estimate source terms during the early stages, where especially air concentration measurement data are limited. This was addressed by Saunier et al. [9], who further developed their method to be applicable in real-time in case of an accident [10]. Our method is inspired by Saunier et al. [9,10], but instead we use a Bayesian inference method to be able to realistically account for uncertainties of the estimated source term, similar to Liu et al. [6].

The method is applied to an idealized artificial release case from the Finnish Loviisa nuclear power plant. A set of simulated air concentration measurements and gamma dose rate measurements have been created as described in Section 2.1. The same meteorological data and dispersion model have been used for data creation and for the source term estimation. Thus, the study demonstrates the uncertainties of the estimated source term arising only from the information loss due to the limited measurement capabilities. Due to the idealized nature of our study, our results apply to a situation, where model errors are negligible. In reality, meteorological uncertainties and model errors will further increase the uncertainty of the estimated source term.

Section 2 describes the data and methodology; Section 2.1 describes the synthetic measurement data set, Sections 2.2 and 2.3 describe the meteorological data and the dispersion model used, while Sections 2.4–2.7 describe the methodology. Next, the results are presented and discussed in Section 3. Finally, Section 4 presents a summary and the conclusions of the study.

2. Materials and Methods

2.1. Artificial Loviisa Release Case

For the artificial release from the Loviisa nuclear power plant in south Finland, the selected source term describes a core melt event without functioning mitigation systems. The initial event is a total loss of all power systems without battery back-up. The filtered containment venting system is assumed disconnected, and instead comprises an exhaust pathway from the reactor containment. It is postulated that the exhaust pathway was open at the time of melt-through of the reactor vessel. The released activity was corrected for decay and ingrowth for the time period between the emergency shutdown of the nuclear

reactor (SCRAM) and the time of the release starting three hours later. It is assumed that there was no significant heat release associated with the accident, and therefore all material is released from a fixed height of 27 m above ground.

The time evolution is given in one-hour time steps starting at the onset of the accident (time of the SCRAM) and the following 12 h, intended to represent the first part of the release to undergo subsequent detection by the gamma monitoring stations and capture by the air filter stations. The source term was developed for the research project SOurce CHAracterizatiOn accounting for meTeorologIcal unCertainties (SOCHAOTIC), for further details, see [11].

Figure 1 shows the gamma dose field at the end of the simulation, 63 h after the release starts, as well as the locations of gamma dose rate stations and filter stations. The source term is given in Section 3.
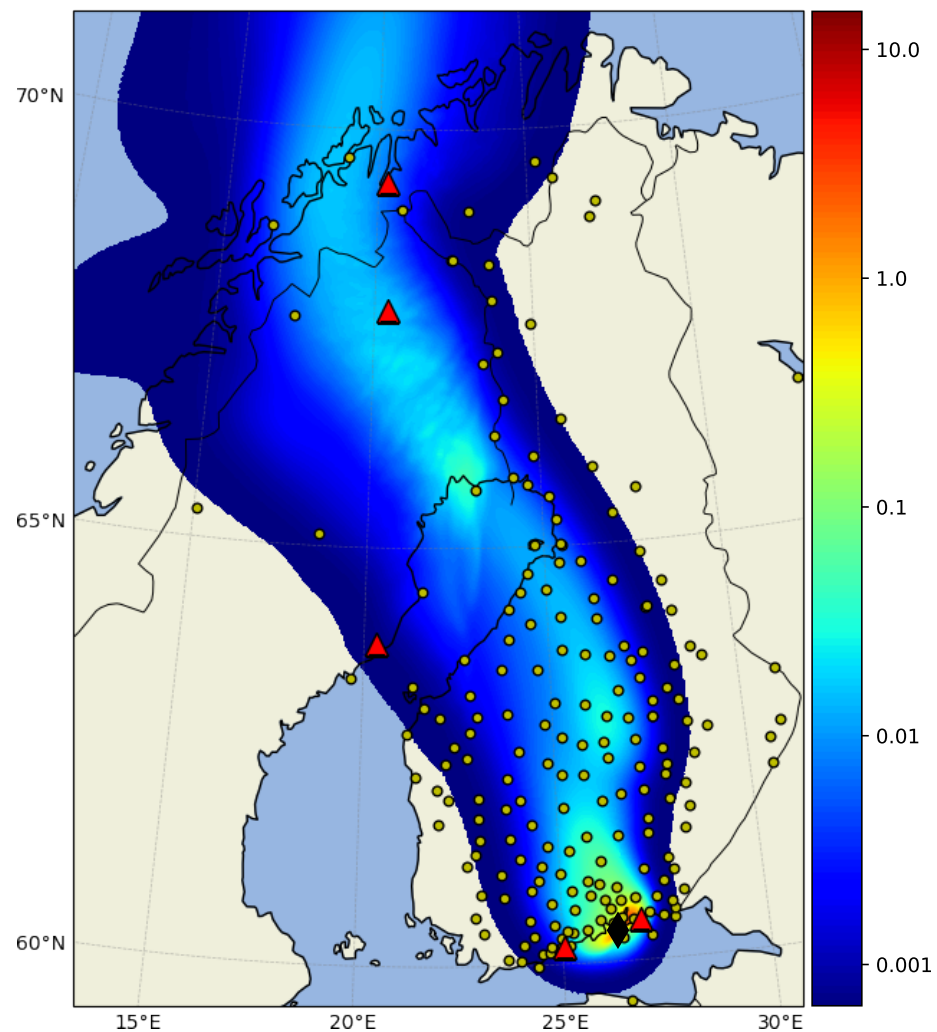
Figure 1. Total gamma dose in units of mSv at 63 h after the release start. Areas only influenced by background radiation are left uncolored. The black diamond shows the release location, the yellow circles show the locations of the gamma stations, and the red triangles show the locations of the filter stations.

2.1.1. Simulated Gamma and Filter Station Measurements

The total dose rate at the gamma monitoring stations is the sum of the contributions from cloud and ground since the stations are not shielded from activity deposited on the ground. Over time, the contamination of the station itself will also contribute to the measurements.

A set of 11 nuclides was selected to represent the most important nuclides for human doses: Kr-88*, Xe-133*, Xe-135*, Xe-135m*, Cs-134#, Cs-137, I-131#, I-132*#, I-133#, I-135# and Te-132. The list consists of the expected top five for the gamma monitoring stations (denoted by *), and top five for the air filter stations (denoted by #), expected to represent more than 90% of the dose rate contribution in the first 12 h of the postulated event. Moreover, two nuclides from the top ten list, Cs-137 and Te-132, were included since they represent key nuclides as seen from historical releases. For further details, see [11].

The artificial scenario consisting of simulated filter station and gamma station measurements was derived by predicting the atmospheric dispersion of radionuclides from a 9-hour release at the Loviisa nuclear power plant starting at 08:00 UTC on 22 September 2021. The DERMA atmospheric dispersion model was applied to the release scenario described above and using Harmonie data, cf. Sections 2.2 and 2.3, thereby providing average concentration values at existing filter stations, and gamma dose rates at gamma stations by using the ARGOS gamma dose model [12,13]. The filter concentration values are computed as 24 h averages from 08:00 UTC to 08:00 UTC the next day. Further, the filter measurement stations are assumed to have a detection limit of $0.1\,\mathrm{mBq\,m^{-3}}$. For the gamma dose rates, we have assumed a background radiation of $0.1\,\mathrm{\mu Sv\,h^{-1}}$, which has been added to all modelled dose rates.

2.2. Meteorological Data

The simulations have been carried out using meteorological data derived by the non-hydrostatic convection-permitting limited-area numerical weather prediction model Harmonie [14]. The horizontal grid resolution is approximately 2.5 km, and the vertical dimension is resolved by 65 levels with a terrain-influenced hybrid coordinate. The lowest model level is about 12 m above ground, and the highest at approximately 10 hPa. The model is configured with three-hourly data assimilation cycling. For the Loviisa case, the model simulation starts on 22 September 2021, at 00:00 UTC and runs until 24 September 2021, at 23:00 UTC.

2.3. Dispersion Modelling

The atmospheric dispersion is modelled by using the Danish Emergency Response Model of the Atmosphere (DERMA) [15,16]. DERMA is used operationally for a number of Danish emergency preparedness purposes [17–21] including nuclear [13]. The three-dimensional model is of Lagrangian type making use of a hybrid stochastic particle-puff diffusion description [15,16]. The model uses aerosol size dependent dry and wet deposition parameterizations as described by [22].

DERMA is interfaced with the nuclear decision-support system ARGOS (Accident Reporting and Guidance Operational System) [12,13], where the integration is accomplished through automatic online exchange of data between ARGOS and the DMI High Performance Computing (HPC) facility. The dose calculation modules are incorporated in ARGOS.

2.4. Problem Description

The temporal release profiles of the radionuclides considered are estimated by using observations of both air concentration and gamma dose rate combined with a series of forward runs by the dispersion model DERMA. We assume an overall start time t_0 and end time t_n of the release. We then separate the total release period into n time bins of duration Δt_{bin} and for each of these assume a unit release of each of the included radionuclides. The releases are assumed to be point releases at ground level. As described in Section 2.1.1, we assume that only a selection of all released radionuclides contributes significantly to the gamma dose rates, while other radionuclides will be ignored. Let C^{o}_{ik} be the k'th observed average concentration of the i'th radionuclide, measured over a specified time period at a specified filter station. Similarly, let $\Gamma^{\mathrm{o}}_{\kappa}$ be the κ'th observed gamma dose rate measured at a specified time and gamma station.

　　3.2.　PAPER 2: BAYESIAN INVERSE MODELLING FOR PROBABILISTIC MULTI-NUCLIDE SOURCE TERM ESTIMATION USING OBSERVATIONS OF AIR CONCENTRATION AND GAMMA DOSE RATE

The atmospheric dispersion model DERMA is run forward in time for each of the unit releases, and for the j'th release of the i'th radionuclide the average activity concentrations $\bar{c}_{ijk}$ are calculated, where the k-index corresponds to the location and time of an existing filter measurement. Further, instantaneous activity concentrations $c_{ij\kappa}$ and deposition values $d_{ij\kappa}$ are calculated, where the κ-index corresponds to the location and time of an existing gamma dose rate observation. By using the gamma dose model as described in Section 2.3, the contributions to the gamma dose rates $\gamma_{ij\kappa} = \gamma_{ij\kappa}(c_{ij\kappa}, d_{ij\kappa})$ are calculated. For a given set of non-negative coefficients, λ_{ij}, the predicted average concentrations and gamma dose rates corresponding to existing measurements are calculated:

$$
C_{ik}^{m} = \sum_{j} \lambda_{ij} \bar{c}_{ijk}
$$
$$
\Gamma_{\kappa}^{m} = \sum_{i} \sum_{j} \lambda_{ij} \gamma_{ij\kappa}. \tag{1}
$$

2.5. Bayesian Inversion and Sampling Method

Given a set of observations, $(\mathbf{C}^{o}, \mathbf{\Gamma}^{o})$, the coefficients, $\boldsymbol{\lambda}$ can be determined by applying Bayes' theorem:

$$
P(\boldsymbol{\lambda}, \boldsymbol{\theta} | \mathbf{C}^{o}, \mathbf{\Gamma}^{o}, I) = \frac{P(\boldsymbol{\lambda}, \boldsymbol{\theta} | I) \, P(\mathbf{C}^{o}, \mathbf{\Gamma}^{o} | \boldsymbol{\lambda}, \boldsymbol{\theta}, I)}{P(\mathbf{C}^{o}, \mathbf{\Gamma}^{o} | I)}, \tag{2}
$$

where $\boldsymbol{\theta}$ denotes any so-called nuisance parameters, i.e., unknown parameters, which are not of direct interest. One way to account for these is to treat them just like the parameters of interest and consider $P(\boldsymbol{\lambda}, \boldsymbol{\theta} | \mathbf{C}^{o}, \mathbf{\Gamma}^{o}, I)$, which is the posterior probability distribution for the combined set of parameters $(\boldsymbol{\lambda}, \boldsymbol{\theta})$. $P(\boldsymbol{\lambda}, \boldsymbol{\theta} | I)$ is then the prior probability distribution for $(\boldsymbol{\lambda}, \boldsymbol{\theta})$, $P(\mathbf{C}^{o}, \mathbf{\Gamma}^{o} | \boldsymbol{\lambda}, \boldsymbol{\theta}, I)$ is the likelihood, and $P(\mathbf{C}^{o}, \mathbf{\Gamma}^{o} | I)$ is the evidence; a statistical constant independent of $(\boldsymbol{\lambda}, \boldsymbol{\theta})$. I is any background information that may be available, e.g., amount of material present in the core at the time of the accident.

To evaluate Equation (2), the quantities $P(\boldsymbol{\lambda}, \boldsymbol{\theta} | I)$ and $P(\mathbf{C}^{o}, \mathbf{\Gamma}^{o} | \boldsymbol{\lambda}, \boldsymbol{\theta}, I)$ must be estimated for a selection of realizations of $(\boldsymbol{\lambda}, \boldsymbol{\theta})$, and the resulting posterior probability distribution $P(\boldsymbol{\lambda}, \boldsymbol{\theta} | \mathbf{C}^{o}, \mathbf{\Gamma}^{o}, I)$ can then be estimated by normalizing the distribution. The posterior probability distribution for $\boldsymbol{\lambda}$ can then be determined by marginalizing:

$$
P(\boldsymbol{\lambda} | \mathbf{C}^{o}, \mathbf{\Gamma}^{o}, I) = \int_{\boldsymbol{\theta}} P(\boldsymbol{\lambda}, \boldsymbol{\theta} | \mathbf{C}^{o}, \mathbf{\Gamma}^{o}, I) \, d\boldsymbol{\theta}. \tag{3}
$$

To get a good estimate of the probability distribution, the relevant parts of the parameter space must be sampled. One option is to use random-walk based Markov Chain Monte Carlo (MCMC) methods, such as Metropolis-Hastings or Gibbs [23,24]. However, these methods generally require a large number of iterations, because the random-walk based model proposals do not sample the parameter space of the posterior probability distribution in the most efficient way. Further, parameters such as the step size of the random-walk typically need to be tuned to the specific case. Instead, we use the Hamiltonian Monte Carlo (HMC) method No U-Turn Sampling (NUTS) [25], implemented in the Python library PyMC3 [26]. HMC methods generally have an advantage over random-walk based MCMC methods, because the model proposals are not generated by a random-walk but instead based on estimated gradients of the posterior distribution. Thus, much fewer iterations are typically needed to sufficiently sample the probability distribution. However, the efficiency of HMC algorithms strongly depends on the step size parameter. The NUTS algorithm uses adaptive step sizing such that the step size does not need to be set by the user. Further, as the name suggests, the algorithm is constructed such that trajectories in the parameter space avoid making "U-turns", i.e., retracing their own steps. Thus, it should produce more independent samples in fewer iterations. When the aim is to use Bayesian inverse modelling operationally, the NUTS algorithm is ideal, since very little parameter tuning is necessary [25]. In addition, when using the PyMC3 implementation [26], Gelman-Rubin convergence diagnostics [27] are automatically calculated, when sampling with two

or more chains. This makes it easy to control that the sampler has converged. For further details on the NUTS algorithm, see [25].

2.6. Prior Probability Distributions

Defining useful prior probability distributions for the release rates is challenging, since the magnitude of the release is unknown. To allow for variation over several orders of magnitude while ensuring non-negative values, we use log-normal prior distributions. Assuming a normal distributed variable $x \sim \mathcal{N}(\mu, \sigma)$, then the variable $z = e^x \sim \text{Lognormal}(\mu, \sigma)$ is log-normal distributed with parameters μ and σ. Thus, these denote the mean and standard deviation of x and not of the log-normal distributed variable z. The prior probability distribution for the coefficients λ_{ij} can be written as:

$$P(\lambda_{ij}|I) = \text{Lognormal}(\mu_i, \sigma_i), \tag{4}$$

where μ_i and σ_i are parameters to be determined for the specific radionuclide. Given that total amount of the i'th radionuclide in the core inventory is S_i in units of Bq, the upper limit for λ_{ij} is $S_i/\Delta t_{\text{bin}}$, where Δt_{bin} is the duration in seconds of each assumed unit release. To allow for release rates approaching the upper limit with reasonable probability, we set $\mu_i + 2\sigma_i = \log(S_i/\Delta t_{\text{bin}})$, where $\log()$ denotes the natural logarithm. The lower limit must be small compared the "typical" release rate, μ_i. Since the typical release rate is unknown, we assume $\mu_i = \log(fS_i/\Delta t_{\text{bin}})$, where f is some (small) fraction. Assuming a sufficiently low value for f will result in a conservative prior distribution, which allows for a broader range than necessary. In this study, we use $f = 10^{-3}$, which means that $\mu_i \pm 2\sigma_i$ includes six orders of magnitude for each release rate. Thus, the mean and standard deviations for the prior probability distributions are given as:

$$\mu_i = \log(10^{-3}S_i/\Delta t_{\text{bin}}) \quad \text{and} \quad \sigma_i = \frac{1}{2}\log(10^3). \tag{5}$$

Further, we can use information about the core inventory to reduce the parameter space by imposing correlations between release rates of certain radionuclides, inspired by the method by Saunier et al. [9,10]. For example, two different isotopes of the same element will largely behave similarly during a release. Thus, if the half-lives of two such isotopes are long compared to the duration of the release and if there is no significant ingrowth from other processes, the ratio of the release rates between two isotopes can be assumed constant and equal to the ratio of the amounts in the core inventory. For example, ^{134}Cs and ^{137}Cs have half-lives of approximately 2 and 30 years, respectively, and thus, the ratio of their activity concentrations in the core inventory can be considered constant during the release. Accordingly, based on the amounts of the two isotopes in the core, we can assume the ratio of their release rates to be constant.

For other isotope pairs, it is necessary to take into account the difference in half-lives in order to set realistic constraints on the release rates. In this case, knowing the amount of the two isotopes at the time of SCRAM gives one limit for the isotopic ratios, while estimating the activity concentration n hours later will provide an estimate of the other limit, assuming no significant ingrowth. An example is the isotope pair ^{131}I and ^{133}I, which has half-lives of approximately 8 days and 20.8 h, respectively. Let the release rates of these isotopes be $q_{^{131}\text{I}}$ and $q_{^{133}\text{I}}$, respectively. Based on their activity concentrations in the core at the time of the accident, we have $\frac{q_{^{133}\text{I}}}{q_{^{131}\text{I}}} < 2.1$. Assuming that the duration of the main release is less than 24 h, we can determine the other limit. Due to radioactive decay during these 24 h, the amount of ^{133}I is decreased by a factor of 0.45, while we assume that the amount of ^{131}I is unchanged due to its relatively long half-life. Thus, a lower limit can be determined $\frac{q_{^{133}\text{I}}}{q_{^{131}\text{I}}} > 0.9$. Following this approach, we determine the following constraints:

$$\frac{q_{^{134}\text{Cs}}}{q_{^{137}\text{Cs}}} = 1.4, \quad 0.001 < \frac{q_{^{132}\text{I}}}{q_{^{131}\text{I}}} < 1.5, \quad 0.9 < \frac{q_{^{133}\text{I}}}{q_{^{131}\text{I}}} < 2.1 \quad \text{and} \quad 0.15 < \frac{q_{^{135}\text{I}}}{q_{^{131}\text{I}}} < 2.0. \tag{6}$$

3.2.   PAPER 2: BAYESIAN INVERSE MODELLING FOR PROBABILISTIC MULTI-NUCLIDE SOURCE TERM ESTIMATION USING OBSERVATIONS OF AIR CONCENTRATION AND GAMMA DOSE RATE

For ^{134}Cs and ^{137}Cs, this effectively means that only one release rate needs to be determined instead of two, and that the combined set of measurements of the two isotopes can be used. For the other isotope pairs, the constraints allow us to define log-normal distributions with upper and lower bounds, which depend on the release rate of one of the other nuclides. Let $\lambda_{\mathrm{m}j}$ and $\lambda_{\mathrm{n}j}$ be the coefficients for two release rates, which are related by the flexible constraints $r_{\mathrm{lower}} < \lambda_{\mathrm{n}j}/\lambda_{\mathrm{m}j} < r_{\mathrm{upper}}$. Then, the prior probability distribution for $\lambda_{\mathrm{m}j}$ will be defined as in Equation (4), while the prior probability distribution for $\lambda_{\mathrm{n}j}$ can be written as:

$$
P(\lambda_{\mathrm{n}j}|I, \text{constraints}) \propto \begin{cases} P(\lambda_{\mathrm{n}j}|I) & r_{\mathrm{lower}} < \frac{\lambda_{\mathrm{n}j}}{\lambda_{\mathrm{m}j}} < r_{\mathrm{upper}} \\ 0 & \text{otherwise} \end{cases}. \tag{7}
$$

It might be possible to impose further constraints, i.e., across the type of element, such that the release rates of the iodine isotopes can also be related to the release rates of the caesium isotopes, Te-132 and the noble gasses. However, the underlying assumptions in this case are less trivial.

2.7. Likelihood and Uncertainty Quantification

The likelihood is the probability of observing the set of measurements $(\mathbf{C}^{\mathrm{o}}, \boldsymbol{\Gamma}^{\mathrm{o}})$, given a proposed source term, $\boldsymbol{\lambda}$. The likelihood is evaluated by assuming a probability distribution for the residuals $C^{\mathrm{o}}_{ik} - C^{\mathrm{m}}_{ik}(\lambda_{ij})$ and $\Gamma^{\mathrm{o}}_{\kappa} - \Gamma^{\mathrm{m}}_{\kappa}(\lambda_{ij})$. In this study, we use a log-normal likelihood, which is less sensitive to outliers than the Gaussian distribution and automatically gives a higher weight to measurements/predictions of low values. This makes it useful when dealing with measurement values over several orders of magnitude [6]. One practical challenge when dealing with log-normal distributions is that only positive values are mathematically allowed, while the physical quantity may in principle be zero. For the gamma dose rates, this is not an issue, since we add background radiation to the modelled measurements, thereby ensuring that values are always positive. For the air concentration measurements, on the other hand, modelled predictions may be zero, while the measured predictions may be below the detection limit. Assume that for a given measurement, C^{o}_{ik}, the detection limit is ϵ_{ik}. To avoid zero-values, we use these altered observations and model predictions $\widetilde{C^{\mathrm{o}}_{ik}} = \max(\epsilon_{ik}, C^{\mathrm{o}}_{ik})$ and $\widetilde{C^{\mathrm{m}}_{ik}} = \max(\epsilon_{ik}, C^{\mathrm{m}}_{ik})$. These altered forms have the additional benefit that they provide a theoretically sound way of using non-detections, since these will only contribute to the likelihood, when the modelled concentration is above the detection limit. Thus, there is no risk of falsely interpreting a low value as a zero. The likelihood is given as:

$$
P\left(\widetilde{\mathbf{C}^{\mathrm{o}}}, \boldsymbol{\Gamma}^{\mathrm{o}}|\boldsymbol{\lambda}, I\right) = \prod_k \prod_i \text{Lognormal}\left(\widetilde{C^{\mathrm{m}}_{ik}}, \sigma_{\mathrm{f}}\right) \prod_{\kappa} \text{Lognormal}\left(\Gamma^{\mathrm{m}}_{\kappa}, \sigma_{\mathrm{g}}\right), \tag{8}
$$

where C^{m}_{ik} and $\Gamma^{\mathrm{m}}_{\kappa}$ are as defined in Equation (1). σ_{f} and σ_{g} are related to the uncertainty of the measurements as well as the unknown model errors. In this study, both are negligible as discussed in Section 1. However, in order to make the method as general as possible, the uncertainty parameters are treated as nuisance parameters, i.e., they are kept as free parameters and sampled by the Monte Carlo algorithm. In practice, a wide uniform distribution has been used as prior distribution for the nuisance parameters $\sigma_{\mathrm{f}}, \sigma_{\mathrm{g}} \sim U(0, 10)$, which allows for a broad range of shapes of log-normal distributions.

3. Results and Discussions

As described in Section 2.5, the results are obtained by using the NUTS algorithm [25], which is implemented in the PyMC3 python library [26]. The algorithm is constructed in such a way that almost no parameter tuning is necessary. To ensure convergence, the target acceptance rate was increased from the default 0.8 to 0.99. Aside from this, everything was kept at PyMC3's default values; two simultaneously running chains, each with 1000 tuning steps and 1000 draws from the target distribution. This provides a total of 2000 realizations

of the posterior probability distribution. For further details on the NUTS parameters, see [25,26].

In our analysis, we include 10 of the 11 radionuclides described in Section 2.1.1, excluding Xe-135m based on the rationale that its short half-life of approximately 15 min makes it unimportant on longer temporal, and thus also spatial scales. This means that there is not enough information in the measurement data to sufficiently constrain the release rate of Xe-135m. The other three noble gasses are included, although there are no filter measurements to help constrain their release rates. However, as long as their half-lives are sufficiently different, we expect the gamma dose rate patterns to differ enough to be able to distinguish between their contributions. The prior probability distributions for the release rates of Kr-88, Xe-133, Xe-135, Cs-137, I-131 and Te-132 were defined as log-normal distributions, Equation (4) with mean and standard deviations given by Equation (5). The release rate for Cs-134 was defined as a deterministic variable, equal to the release rate for Cs-137 multiplied by the fixed ratio 1.4. Finally, the prior distributions for the release rates of I-132, I-133 and I-135 were defined as bound log-normal distributions Equation (7), where the bounds are given by the flexible constraints, Equation (6).

We assume that the time of the emergency shutdown of the nuclear reactor (SCRAM), 22 September, 05:00 UTC, is known. We therefore consider this as the first possible time of release. We then consider the release during the following 24 h by assuming twelve 2-h constant releases, i.e., $\Delta t_{\text{bin}} = 7200$ s. The source term estimation is based on the simulated measurements described in Section 2.1.1, but only measurements until 23 September, 08:00 UTC are used for the source term estimation, leaving the remaining measurements for validation of model predictions based on the estimated source term. Thus, for all particles, only two 24-h filter measurements from each of the five filter stations are available, i.e., ten filter measurements per particle. However, first, all measurements without any information are discarded; if a given measurement is not influenced by any of the time-binned unit releases, it is removed from the data set. After this automatic removal of data, only one filter measurement per particle from each of the two filter stations in southern Finland are left. Thus, even when using the additional constraints described in Section 2.6, the amount of filter measurement data is very limited.

The gamma dose rates, on the other hand, are measured every hour at 214 different locations, see Figure 1. Thus, from 22 September, 05:00 UTC to 23 September, 08:00 UTC, a total of 5778 measurements. After the automatic removal of data without information, 1918 measurements are left.

Given the high dimensionality of the parameter space, it is not possible to visualize all elements of the actual posterior distribution. Instead the individual release rates are shown in Figure 2. The plots show the median release rates as well as the 10th and 90th percentiles based on marginal distributions for each 2-h release period. Further, Figure 3 shows histograms of the marginal distributions of time integrated releases for all radionuclides. The only release rate, which is well determined for most time bins is that of Xe-133. This makes sense, since it is the only relatively long-lived noble gas; the half-life is approximately five days, while Xe-135 and Kr-88 have half-lives of roughly nine and three hours, respectively. Further, since the noble gasses do not deposit, the gamma dose rate pattern of Xe-133 will also be easy to distinguish from those of the long-lived particles. For the particles, the estimated release rates clearly indicate the effects of the constraints in Equation (6); the release rates of the four iodine isotopes, which are all "tied together", are better estimated than those of both the caesium isotopes and of Te-132. Since the release rates of the two caesium isotopes are forced to differ only by a factor, we also expect these to be better estimated than the release rate of Te-132. While it is not easy to see that this is the case, it is clear from Figure 3 that the released amounts of the two caesium isotopes are better estimated than Te-132.
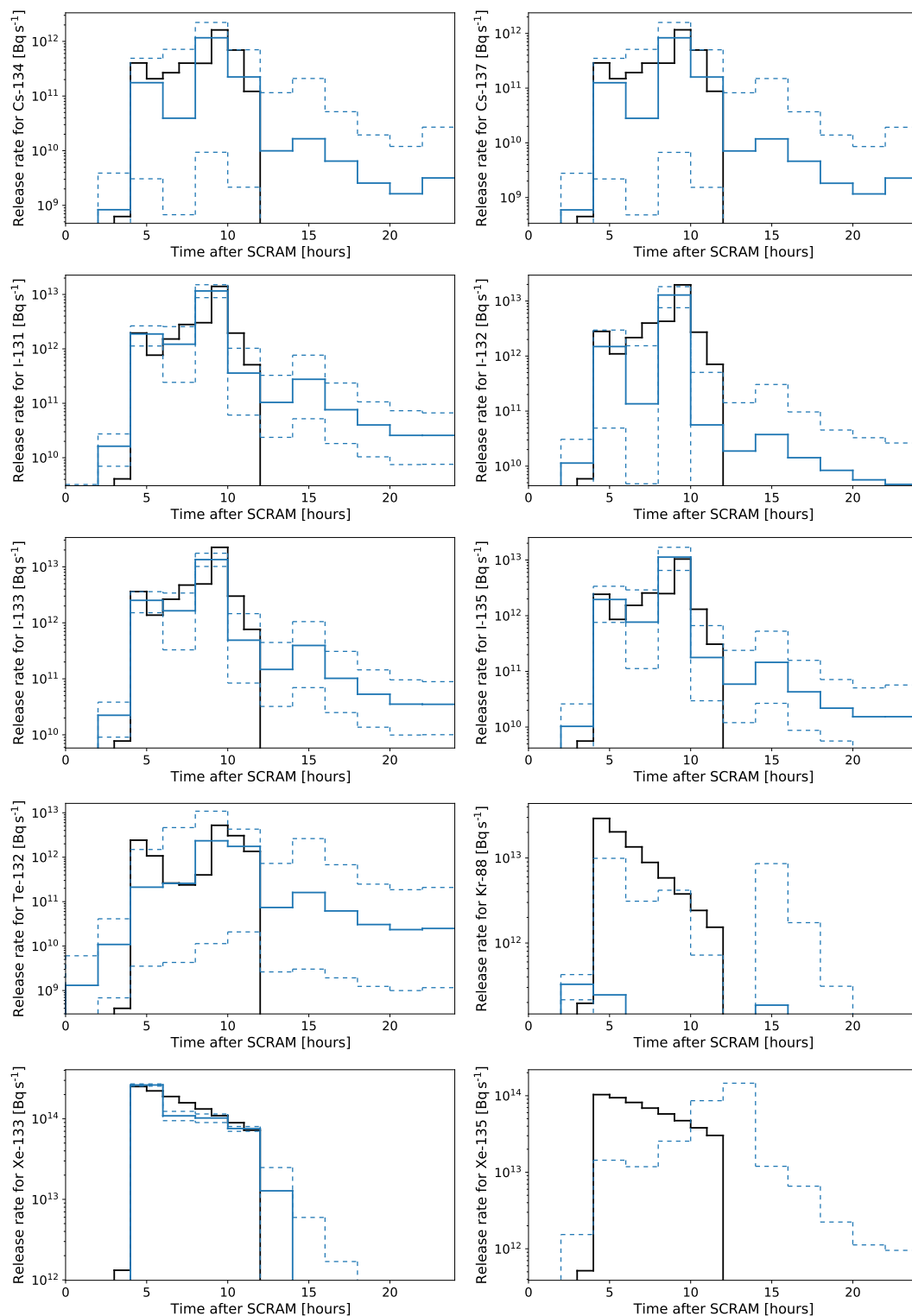
　　　3.2. PAPER 2: BAYESIAN INVERSE MODELLING FOR PROBABILISTIC MULTI-NUCLIDE SOURCE TERM ESTIMATION USING OBSERVATIONS OF AIR CONCEN-TRATION AND GAMMA DOSE RATE

Figure 2. Release rates for each radionuclide in each 2-h time bin. The solid blue lines show the medians of the marginal distributions, while the dashed blue lines show the 10th and 90th percentiles. For comparison, the solid black lines show the true release profile. To focus on the release rates of high magnitude, we have set the minimum value on the *y*-axis to 10% of the lowest true release rate. Thus, predicted release rates below this limit are not shown in the plot, e.g., the predicted release rate of Xe-135 only shows the 90th percentile, while both the 10th percentile and the median are below the axis limit.
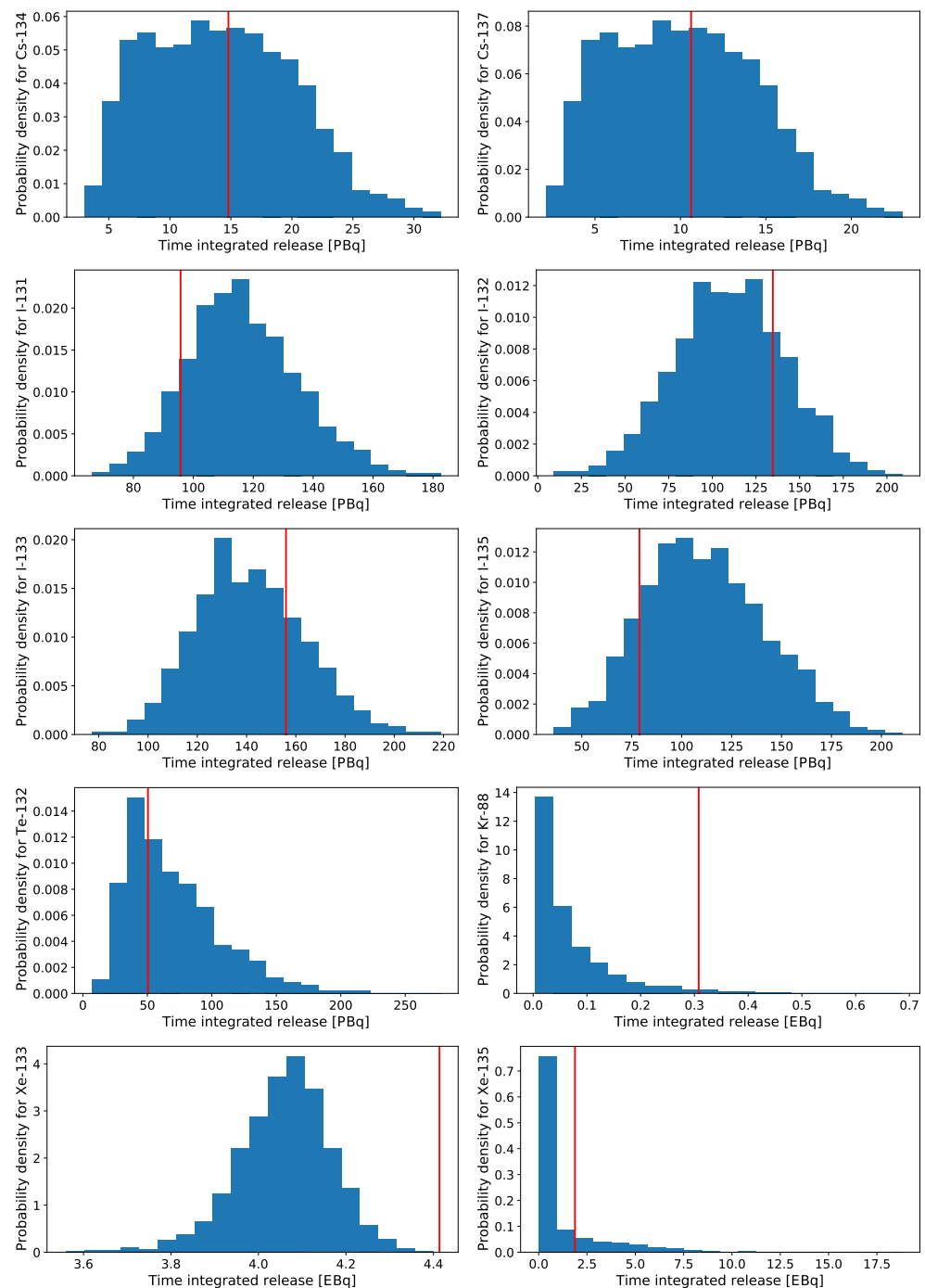
Figure 3. Probability density for each radionuclide as a function of time-integrated release. The vertical red lines show the actual released amounts.

The histograms in Figure 3 show that for some radionuclides, the amounts are quite well constrained, e.g., the release of I-131, which varies from roughly 70 PBq to 180 PBq, and Xe-133, which varies from roughly 3.6 EBq to 4.4 EBq. The latter, however, only barely include the true released amount in the probability distribution. For the remaining radionuclides, the released amounts are not very accurately estimated, especially not for Kr-88 and Xe-135. Given the limited amount of measurement data, this result is not surprising. Further, it is important to note that the log-normal prior distribution ensures release rates of positive values. Hence, the estimated release will necessarily have the same duration as the considered release period, 24 h in this case. However, we see from Figure 2 that most release rates drop significantly in magnitude after 12 h from SCRAM.

3.2. PAPER 2: BAYESIAN INVERSE MODELLING FOR PROBABILISTIC MULTI-NUCLIDE SOURCE TERM ESTIMATION USING OBSERVATIONS OF AIR CONCEN-TRATION AND GAMMA DOSE RATE

From Figures 2 and 3, it may seem that the source term is not sufficiently constrained by the data. Clearly, release rates for some nuclides are poorly estimated, e.g., Kr-88 and Xe-135, and it may therefore be tempting to exclude these from the source term. However, we found that when excluding these, the estimated release rates of the remaining nuclides are less accurate. Thus, it seems that the release of some of the other nuclides compensate for their lacking contribution. On the other hand, it is important to note that including Kr-88 and Xe-135 in the source term does not seem to compromise the release rates of the remaining nuclides. Thus, when it is not known a priori which nuclides constitute the best possible source term, the safer choice seems to be to include more nuclides than necessary. Further, the marginal distributions are obtained by integrating over the remaining parameters of the multi-nuclide source term, and therefore all correlations between parameters are ignored. As demonstrated below, though the marginal distributions of individual releases might be uncertain, the gamma dose rate patterns of different realizations of the multi-nuclide source term vary significantly less.

Figure 4 shows predicted air concentrations and gamma dose rates as function of observations. The upper plots show filter measurements, and the lower plots show gamma dose rates. The left plots show measurements before 23 September, 08:00 UTC, i.e., the measurements that are used for the source term estimation. The right plots show measurements after 23 September, 08:00 UTC and therefore show a prediction of future values based on the estimated source term. The percentiles are estimated by first calculating the concentrations and gamma dose rates from all source terms in the posterior distribution and then finding the percentiles in the calculated values. The plots with the gamma dose rates show a randomly selected subset of 300 observations, since more data in the plot makes it impossible to distinguish the different data points. The figure shows that the average activity concentrations at the filter stations are generally estimated to match the observations within the uncertainties, although some allow for a wide variation. On the other hand, the predicted gamma dose rates fit very well with the observed even for the predicted values. Considering the fact that a total of 1918 gamma measurements and only 2 filter measurements for each nuclide are used for the inversion, it is not surprising that the gamma dose rates are more accurately estimated.
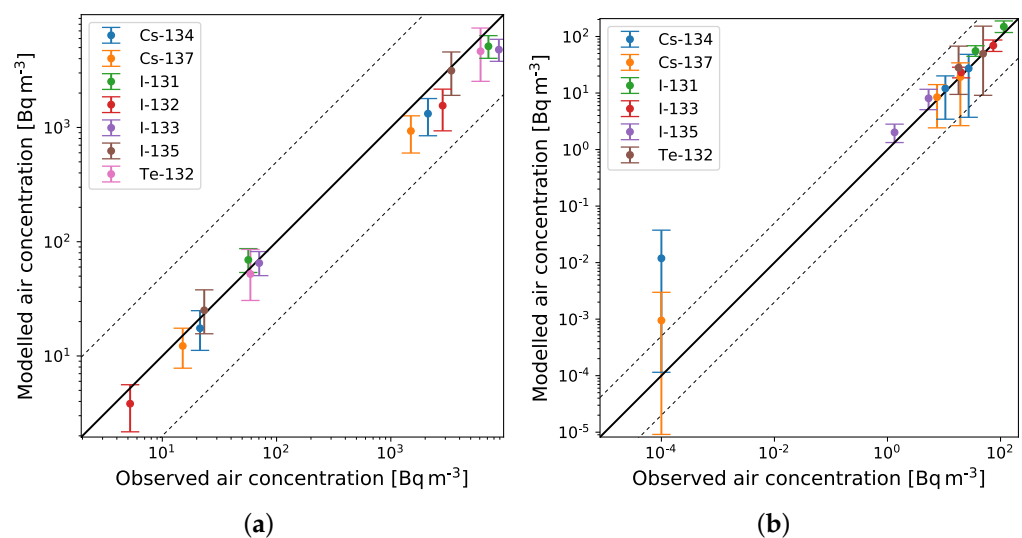

(a)   (b)

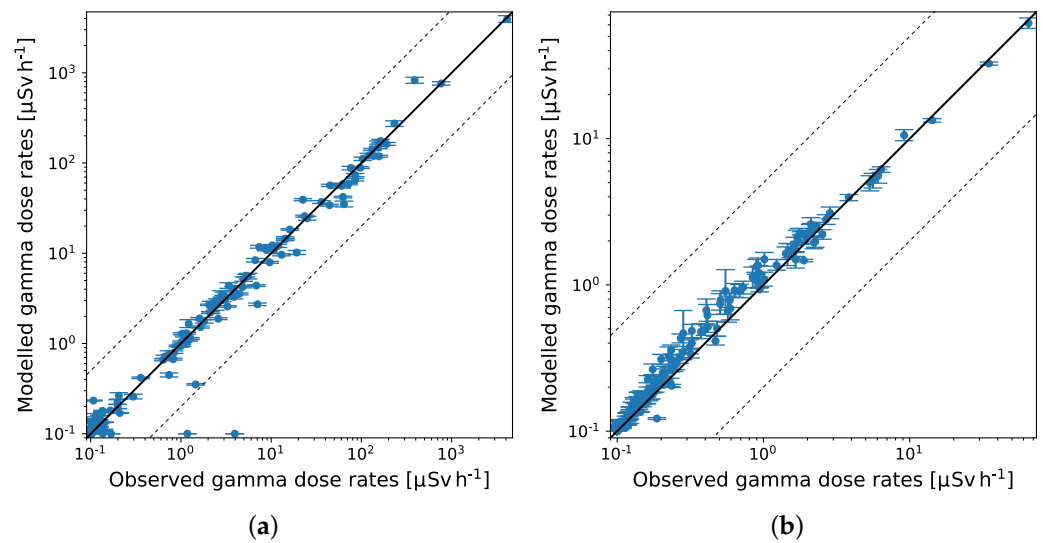**Figure 4.** *Cont.*

(**a**) (**b**)

Figure 4. Model predictions with uncertainties (median and 10th and 90th percentile) on the *y*-axis, and observations on the *x*-axis. The solid black lines indicate a perfect correlation, while the dashed black lines indicate a factor of 5 between model and observation. (**a**) shows the filter measurements until 23 September, 08:00 UTC, i.e., the measurements that are used for the source term estimation, whereas (**b**) shows the filter measurements after 23 September, 08:00 UTC, i.e., predicted future air concentrations. (**c**) similarly shows the gamma dose rates until 23 September, 08:00 UTC, and (**d**) shows the gamma dose rates after 23 September, 08:00 UTC.

Figure 5 shows the predicted gamma dose rates at the locations of six selected gamma stations, viz. the six stations that measured the highest values. The plots show that there is good agreement between modelled observed gamma dose rates and that even the time evolution is captured very well.
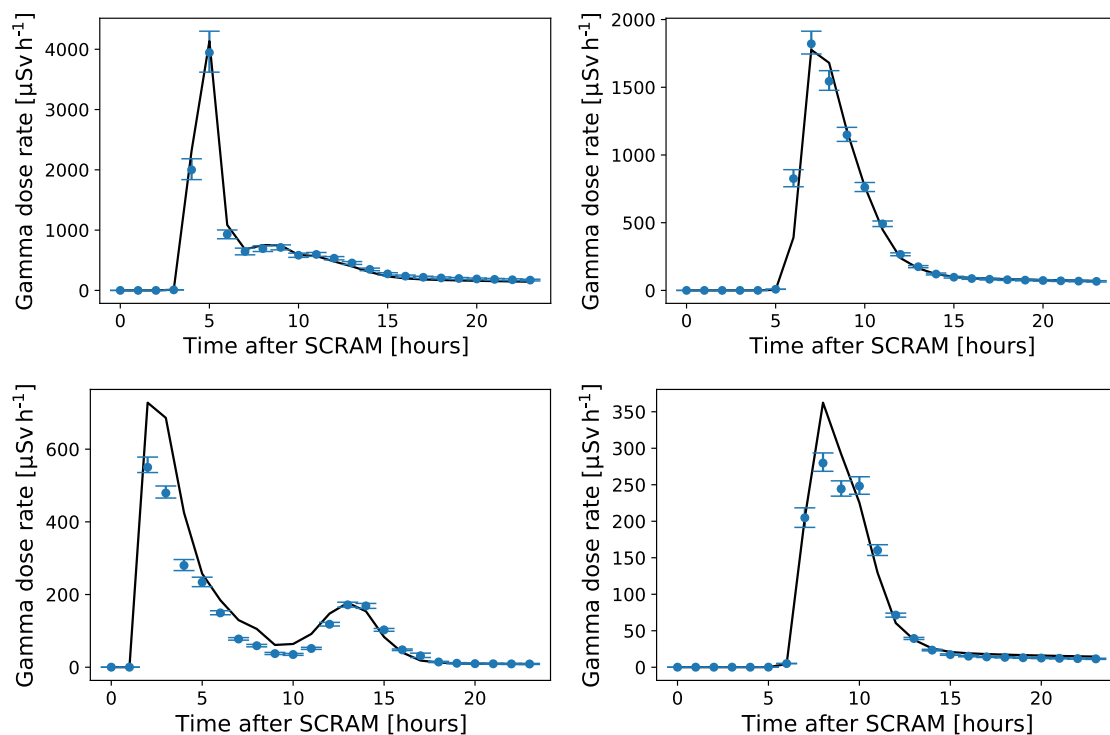

Figure 5. *Cont.*

3.2. PAPER 2: BAYESIAN INVERSE MODELLING FOR PROBABILISTIC MULTI-NUCLIDE SOURCE TERM ESTIMATION USING OBSERVATIONS OF AIR CONCEN-TRATION AND GAMMA DOSE RATE
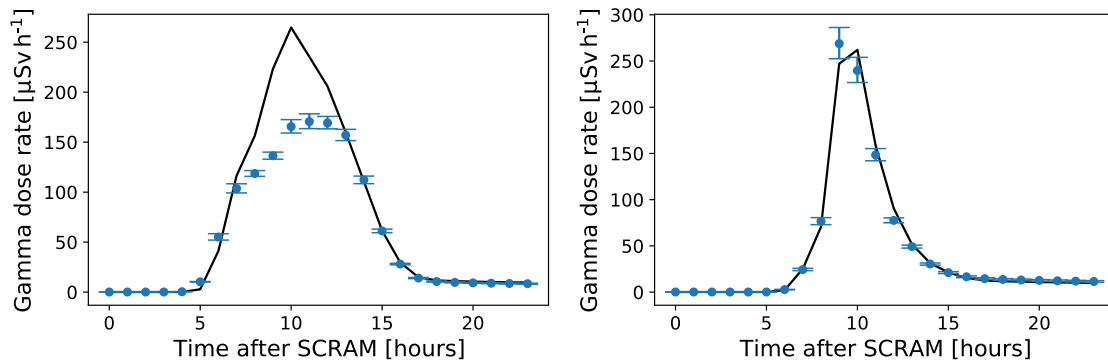
Figure 5. Gamma dose rates at locations of gamma stations during the first 24 h after the accident. Model predictions with uncertainties (median and 10th and 90th percentile) are shown by the blue dots and error bars, while the true gamma dose rates are shown by the black solid line. The selected gamma stations are all close to release locations, viz. the six stations that measured the highest values during the first 24 h.

Finally, Figure 6 shows the probability distributions of the two uncertainty parameters σ_f and σ_g; both parameter distributions indicate relatively narrow log-normal distributions, which is expected given that model errors are negligible.
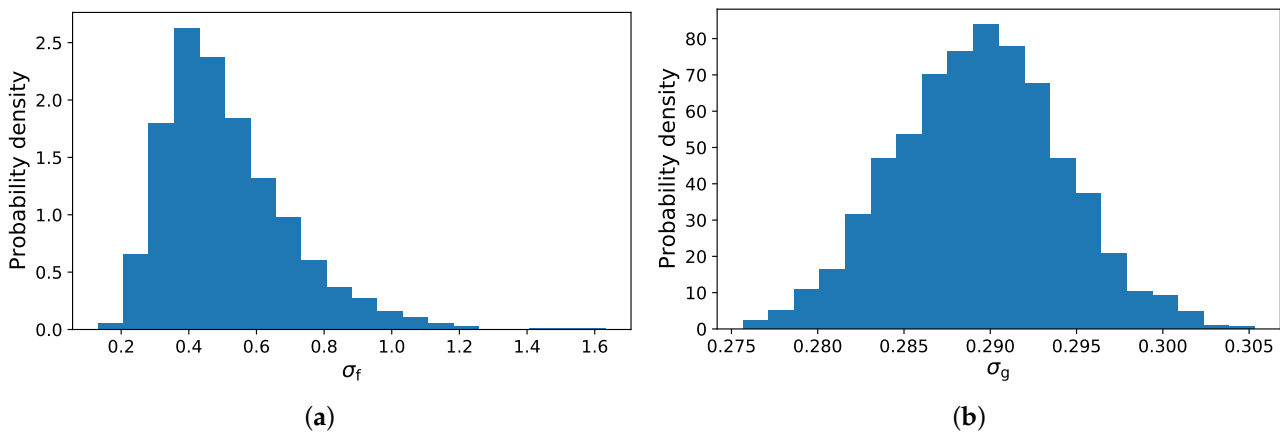

(**a**) (**b**)

Figure 6. Marginal probability distributions of the uncertainty parameters, (**a**) σ_f and (**b**) σ_g.

3.1. Including All Data

For comparison, we show the estimated source term when including all measurements. Figure 7 shows the release rates and probability densities of released amounts for three selected nuclides, Cs-134, I-131 and Xe-133. Interestingly, the release rates are all better defined than the previous result, i.e., the distributions are narrower. However, the release rate estimates are not necessarily more accurate. On the other hand, comparison with Figure 2 shows that the use of later measurements allows for a better estimate of the duration, as all release rates are very low after 16 h from the SCRAM.

As discussed previously, there are not many filter measurements available, and therefore the gamma dose rates are dominant; thus, the estimated source term is more likely to match the gamma dose rates than the filter measurements. This is apparent from Figure 8, which shows the modelled air concentrations and gamma dose rates as function of observations, similar to Figure 4. There is a very good agreement for gamma dose rates, while for air concentrations, the discrepancy is somewhat larger.
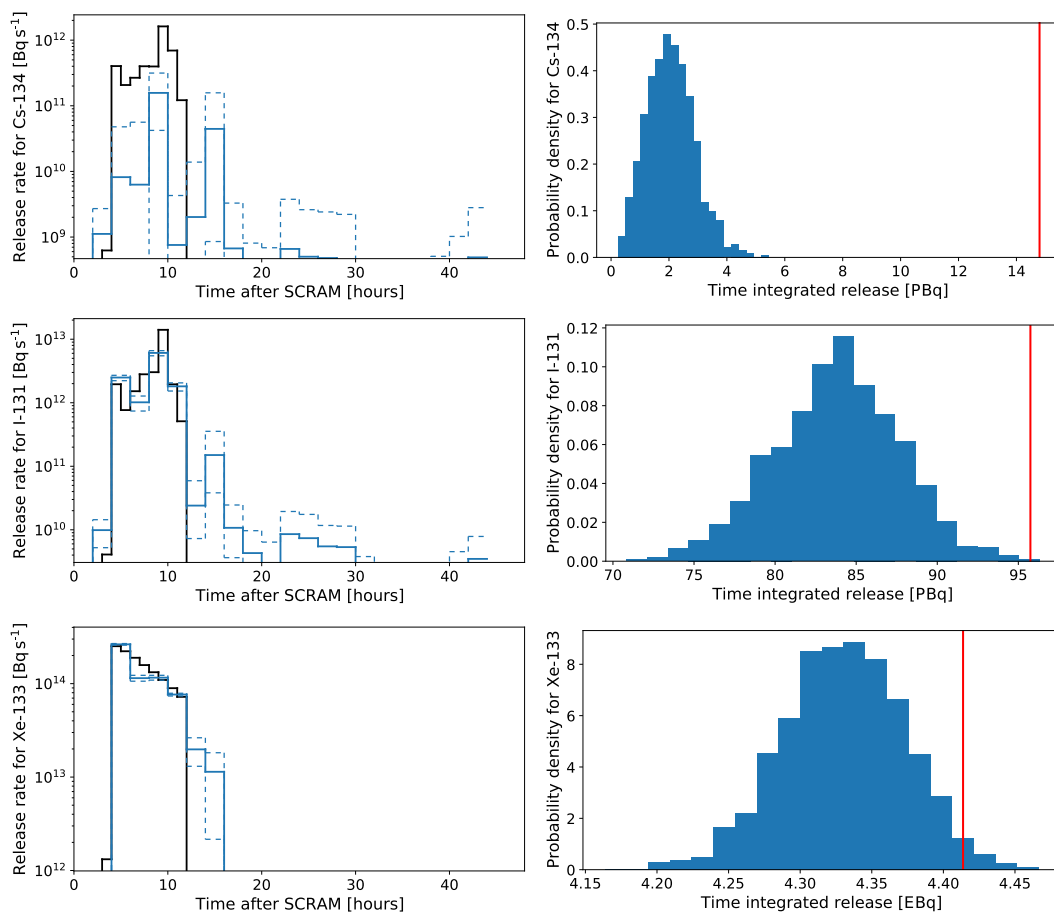
Figure 7. Release rates and probability densities for selected nuclides. For further description of the plots, see captions of Figures 2 and 3.
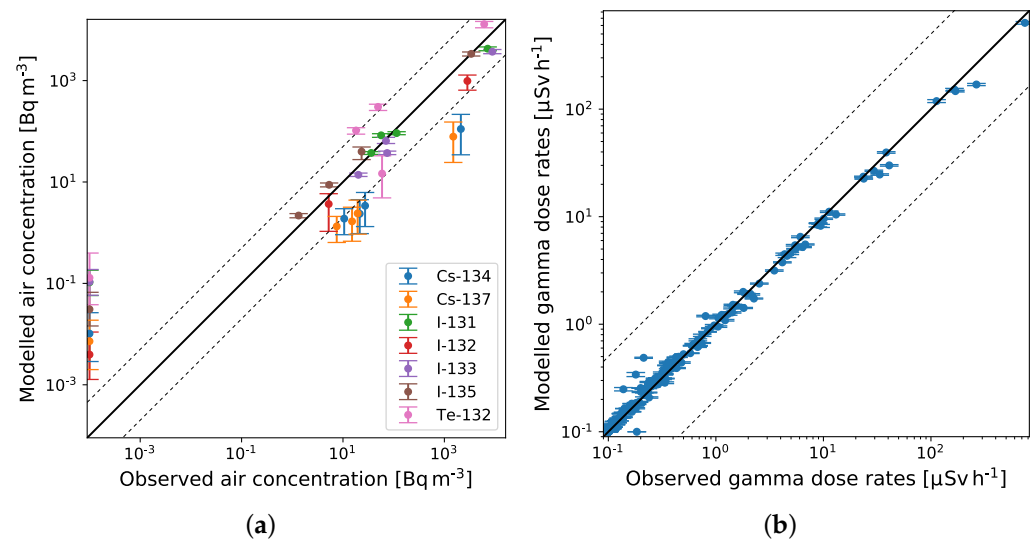

Figure 8. Model predictions with uncertainties (median and 10th and 90th percentile) on the *y*-axis, and observations on the *x*-axis. The solid black lines indicate a perfect correlation, while the dashed black lines indicate a factor of 5 between model and observation. (**a**) shows the filter measurements, whereas (**b**) shows the gamma dose rates.

3.2.   PAPER 2: BAYESIAN INVERSE MODELLING FOR PROBABILISTIC MULTI-NUCLIDE SOURCE TERM ESTIMATION USING OBSERVATIONS OF AIR CONCENTRATION AND GAMMA DOSE RATE

3.2. Efficiency

Regarding efficiency, we only have rough estimates of the computation time. However, we see that the time depend strongly on the amount of data included. The computation time for the first result, using data from only the first 24 h, was approximately half an hour. When including all data, the computation time was approximately 3.5 h. These estimates are the wall times of the runs of the NUTS algorithm, when running the algorithm in parallel on two CPUs on a standard modern laptop. In addition, some time is of course required for running the dispersion model and restructuring the data.

When operationalized, the code should be adapted to run on an HPC facility to further decrease computation time. In addition, the total set of gamma dose rate observations constitute 8953 measurements from a relatively dense network sampling at every hour. We suspect that there is a lot of redundant information in this data set, so instead using a subsample of this data set might be sufficient and would reduce computation time significantly.

4. Summary and Conclusions

We have developed a Bayesian inverse method for probabilistic source term estimation to be used for accidental nuclear releases to the atmosphere. The source term probability distribution is sampled using the Hamiltonian Monte Carlo algorithm NUTS, which is robust and needs only limited parameter tuning. In theory, this makes it directly applicable to other cases without making significant changes to the method.

The method is applied to a synthetic data set derived by running an atmospheric dispersion model for a realistic accident at a nuclear power plant. The data set consists of air concentration measurements at existing filter stations as well as gamma dose rates at gamma stations. We have shown that even with a limited set of air concentration measurements, realistic source term estimation is possible based on early observations of gamma dose rates. Further, the results indicate that additional constraints on the release rates based on information on the nuclear reactor core inventory can be used to improve the accuracy of the predictions. The estimated released amounts of most individual radionuclides are described by relatively wide probability distributions. However, the gamma dose rates predicted using the probabilistic source term correspond well with observations.

Of course, when applied to a real-world case, we expect that model errors will reduce the accuracy of the predictions to some extent. However, if the models used are unbiased, we anticipate that the predicted gamma dose rates will still be more accurately estimated than the release rates of the individual radionuclides. Further, to make the method as generally applicable as possible, we treat the uncertainty parameters as nuisance parameters. Hence, no assumptions about the magnitude of the uncertainties are made; the only assumption is that the residuals are log-normal distributed.

In conclusion, we have developed a method that performs well applied to the simulated release case, and the results indicate that even with limited measurement data available, it is possible to construct a probabilistic source term that provides accurate predictions of gamma dose rates and reasonable estimates of the released amounts of most of the radionuclides considered. Due to the few assumptions made and the robust theoretical foundation, we expect the method to generalize well. However, in order to fully examine the performance of the method, future application to real-world cases is necessary.

Author Contributions: Conceptualization, K.S.T. and J.H.S.; methodology, K.S.T.; software, K.S.T.; validation, K.S.T.; formal analysis, K.S.T.; investigation, K.S.T.; writing—original draft preparation, K.S.T.; writing—review and editing, K.S.T. and J.H.S.; visualization, K.S.T.; supervision J.H.S.; funding acquisition, K.S.T. and J.H.S. All authors have read and agreed to the published version of the manuscript.

SOCHAOTIC (SOurce CHAracterizatiOn accounting for meTeorologIcal unCertainties) project, grant number AFT/B(22)1.

Institutional Review Board Statement: Not applicable

Informed Consent Statement: Not applicable

Conflicts of Interest: The authors declare no conflict of interest.

Abbreviations

The following abbreviations are used in this manuscript:

DERMA	Danish Emergency Response Model of the Atmosphere
MCMC	Markov Chain Monte Carlo
HMC	Hamiltonian Monte Carlo
NUTS	No U-Turn Sampling
SOCHOTIC	SOurce CHAracterizatiOn accounting for meTeorologIcal unCertainties

References

1. Sørensen, J.H. Method for source localization proposed and applied to the October 2017 case of atmospheric dispersion of Ru-106. *J. Environ. Radioact.* **2018**, *189*, 221–226. [CrossRef] [PubMed]
2. Saunier, O.; Didier, D.; Mathieu, A.; Masson, O.; Le Brazidec, J.D. Atmospheric modeling and source reconstruction of radioactive ruthenium from an undeclared major release in 2017. *Proc. Natl. Acad. Sci. USA* **2019**, *116*, 24991–25000. [CrossRef] [PubMed]
3. Le Brazidec, J.D.; Bocquet, M.; Saunier, O.; Roustan, Y. MCMC methods applied to the reconstruction of the autumn 2017 Ruthenium-106 atmospheric contamination source. *Atmos. Environ. X* **2020**, *6*, 100071. [CrossRef]
4. Tølløse, K.S.; Kaas, E.; Sørensen, J.H. Probabilistic Inverse Method for Source Localization Applied to ETEX and the 2017 Case of Ru-106 including Analyses of Sensitivity to Measurement Data. *Atmosphere* **2021**, *12*, 1567. [CrossRef]
5. Winiarek, V.; Bocquet, M.; Saunier, O.; Mathieu, A. Estimation of errors in the inverse modeling of accidental release of atmospheric pollutant: Application to the reconstruction of the cesium-137 and iodine-131 source terms from the Fukushima Daiichi power plant. *J. Geophys. Res. Atmos.* **2012**, *117*, D05122. [CrossRef]
6. Liu, Y.; Haussaire, J.M.; Bocquet, M.; Roustan, Y.; Saunier, O.; Mathieu, A. Uncertainty quantification of pollutant source retrieval: Comparison of Bayesian methods with application to the Chernobyl and Fukushima Daiichi accidental releases of radionuclides. *Q. J. R. Meteorol. Soc.* **2017**, *143*, 2886–2901. [CrossRef]
7. Stohl, A.; Seibert, P.; Wotawa, G.; Arnold, D.; Burkhart, J.F.; Eckhardt, S.; Tapia, C.; Vargas, A.; Yasunari, T.J. Xenon-133 and caesium-137 releases into the atmosphere from the Fukushima Dai-ichi nuclear power plant: Determination of the source term, atmospheric dispersion, and deposition. *Atmos. Chem. Phys.* **2012**, *12*, 2313–2343. [CrossRef]
8. Terada, H.; Nagai, H.; Tsuduki, K.; Furuno, A.; Kadowaki, M.; Kakefuda, T. Refinement of source term and atmospheric dispersion simulations of radionuclides during the Fukushima Daiichi Nuclear Power Station accident. *J. Environ. Radioact.* **2020**, *213*, 106104. [CrossRef]
9. Saunier, O.; Mathieu, A.; Didier, D.; Tombette, M.; Quélo, D.; Winiarek, V.; Bocquet, M. An inverse modeling method to assess the source term of the Fukushima Nuclear Power Plant accident using gamma dose rate observations. *Atmos. Chem. Phys.* **2013**, *13*, 11403–11421. [CrossRef]
10. Saunier, O.; Korsakissok, I.; Didier, D.; Doursout, T.; Mathieu, A. Real-time use of inverse modeling techniques to assess the atmospheric accidental release of a nuclear power plant. *Radioprotection* **2020**, *55*, 107–115. [CrossRef]
11. Sørensen, J.H.; Feddersen, H.; Tølløse, K.S.; Kouznetsov, R.; Sofiev, M.; Uppstu, A.; Klein, H.; Ulimoen, M.; Robertson, L.; Pehrsson, J.; et al. *NKS-458: SOurce CHAracterizatiOn Accounting for meTeorologIcal unCertainties (SOCHAOTIC)—First-Year Report*; Technical Report; Nordic Nuclear Safety Research (NKS): Roskilde, Denmark, 2021; ISBN 978-87-7893-551-9.
12. Hoe, S.; Sørensen, J.H.; Thykier-Nielsen, S. The nuclear decision support system ARGOS NT and early warning systems in some countries around the Baltic sea. In Proceedings of the 7th Topical Meeting on Emergency Preparedness and Response, Santa Fe, NM, USA, 14–17 September 1999.
13. Hoe, S.; Müller, H.; Gering, F.; Thykier-Nielsen, S.; Sørensen, J.H. ARGOS 2001 a decision support system for nuclear emergencies. In Proceedings of the Radiation Protection and Shielding Division Topical Meeting. Santa Fe, NM, USA, 14–17 April 2002.
14. Bengtsson, L.; Andrae, U.; Aspelien, T.; Batrak, Y.; Calvo, J.; de Rooy, W.; Gleeson, E.; Hansen-Sass, B.; Homleid, M.; Hortal, M.; et al. The HARMONIE–AROME Model Configuration in the ALADIN–HIRLAM NWP System. *Mon. Weather. Rev.* **2017**, *145*, 1919–1935. [CrossRef]
15. Sørensen, J.H. Sensitivity of the DERMA long-range Gaussian dispersion model to meteorological input and diffusion parameters. *Atmos. Environ.* **1998**, *32*, 4195–4206. [CrossRef]
16. Sørensen, J.H.; Baklanov, A.; Hoe, S. The Danish emergency response model of the atmosphere (DERMA). *J. Environ. Radioact.* **2007**, *96*, 122–129. [CrossRef] [PubMed]

17. Sørensen, J.H.; Mackay, D.K.J.; Jensen, C.Ø.; Donaldson, A.I. An integrated model to predict the atmospheric spread of foot-and-mouth disease virus. *Epidemiol. Infect.* **2000**, *124*, 577–590. [CrossRef]

18. Sørensen, J.H.; Jensen, C.Ø.; Mikkelsen, T.; Mackay, D.; Donaldson, A.I. Modelling the atmospheric spread of foot-and-mouth disease virus for emergency preparedness. *Phys. Chem. Earth* **2001**, *26*, 93–97. [CrossRef]

19. Mikkelsen, T.; Alexandersen, S.; Astrup, P.; Champion, H.J.; Donaldson, A.I.; Dunkerley, F.N.; Gloster, J.; Sørensen, J.H.; Thykier-Nielsen, S. Investigation of airborne foot-and-mouth disease virus transmission during low-wind conditions in the early phase of the UK 2001 epidemic. *Atmos. Chem. Phys* **2003**, *3*, 2101–2110. [CrossRef]

20. Gloster, J.; Jones, A.; Redington, A.; Burgin, L.; Sørensen, J.H.; Turner, R. International approach to atmospheric disease dispersion modelling. *Vet. Rec.* **2010**, *166*, 369. [CrossRef]

21. Gloster, J.; Jones, A.; Redington, A.; Burgin, L.; Sørensen, J.H.; Turner, R.; Hullinger, P.; Dillon, M.; Astrup, P.; Garner, G.; et al. Airborne spread of foot-and-mouth disease – model intercomparison. *Vet. J.* **2010**, *183*, 278–286. [CrossRef]

22. Baklanov, A.; Sørensen, J.H. Parameterisation of radionuclide deposition in atmospheric dispersion models. *Phys. Chem. Earth* **2001**, *26*, 787–799. [CrossRef]

23. Hastings, W.K. *Monte Carlo Sampling Methods Using Markov Chains and Their Applications*; Oxford University Press: Oxford, UK, 1970.

24. Casella, G.; George, E.I. Explaining the Gibbs sampler. *Am. Stat.* **1992**, *46*, 167–174.

25. Hoffman, M.D.; Gelman, A. The No-U-Turn sampler: Adaptively setting path lengths in Hamiltonian Monte Carlo. *J. Mach. Learn. Res.* **2014**, *15*, 1593–1623.

26. Salvatier, J.; Wiecki, T.V.; Fonnesbeck, C. Probabilistic programming in Python using PyMC3. *PeerJ Comput. Sci.* **2016**, *2*, e55. [CrossRef]

27. Gelman, A.; Rubin, D.B. Inference from iterative simulation using multiple sequences. *Stat. Sci.* **1992**, *7* , 457–472. [CrossRef]

3.2. PAPER 2: BAYESIAN INVERSE MODELLING FOR PROBABILISTIC MULTI-NUCLIDE SOURCE TERM ESTIMATION USING OBSERVATIONS OF AIR CONCEN-TRATION AND GAMMA DOSE RATE

3.3 Supplementary results

The results presented in the article in the previous section demonstrated that the methodology gives an accurate source term estimate when model errors are negligible. The next step is then to test the capabilities of the method in a more realistic setup, where model uncertainties are no longer negligible. Therefore, the method is applied to the same release scenario as studied in the article but using a different measurement data set.

3.3.1 Data and methods

The observational data set was created by the Finnish Meteorological Institute (FMI) by running their operational dispersion model SILAM (Sofiev et al., 2015) driven with Harmonie NWP model forecast data of 5 km horizontal resolution. The simulation had a duration of 48 hours from the time of the SCRAM, i.e. shutdown of the nuclear reactor, and hourly average concentrations were provided at the locations of the filter stations, as well as hourly gamma dose rates at the locations of gamma stations. For further details, see Sørensen et al. (2023).

As in the article, the hourly average concentrations at the filter stations were used to estimate 24-hour average concentrations for a more realistic data set. Further, average concentrations below a threshold value of $0.1 \, \mathrm{m \, Bq \, m^{-3}}$ are interpreted as non-detectable. It should be noted that the simulation period is shorter than the period selected in the article, where the model was run for 63 hours. As discussed in the article, it will take some time before the released particles and gasses are measured by the monitoring system. Thus, when attempting to estimate the source term for the entire 48-hour period, the release rates in the latest time bins should not be expected to be constrained by any data.

The method described in Section 2 of the article was then applied to the SILAM-generated data set, using the same configurations of the NUTS algorithm (Hoffman et al., 2014) as described in Section 3 of the article. However, to reduce the number of free parameters in the source term model and hopefully allow for easier convergence, we here used six-hour time bins instead of the two-hour bins used in the article. Further, we again exclude Xe-135m from the analysis due to its short half-life of roughly 15 minutes.

3.3.2 Source term estimation, including gamma dose rates

Figures 3.1 and 3.2 show the estimated release rates and marginal distributions of time-integrated releases, respectively (similar to Figures 2 and 3 in the article). The results given in Figure 3.1 show that essentially none of the release rates are estimated correctly. The release rate of Kr-88 is very well constrained from 6 to 12 hours, but to a much lower value than the actual release. Moreover, certain iodine isotopes appear to be somewhat constrained; however, once again, the values do not align with the actual release rates. Overall, the estimated release rates exhibit no noticeable pattern, and the values are consistently far too low.

The marginal distributions of the time-integrated releases, shown in Figure 3.2, confirm that none of the releases are accurately estimated. Further, they support the conclusion that all releases are significantly underestimated. To understand these results, we take a closer look at the predicted air concentrations and gamma dose rate patterns obtained by applying the estimated source term. These are shown in Figure 3.3 (similar
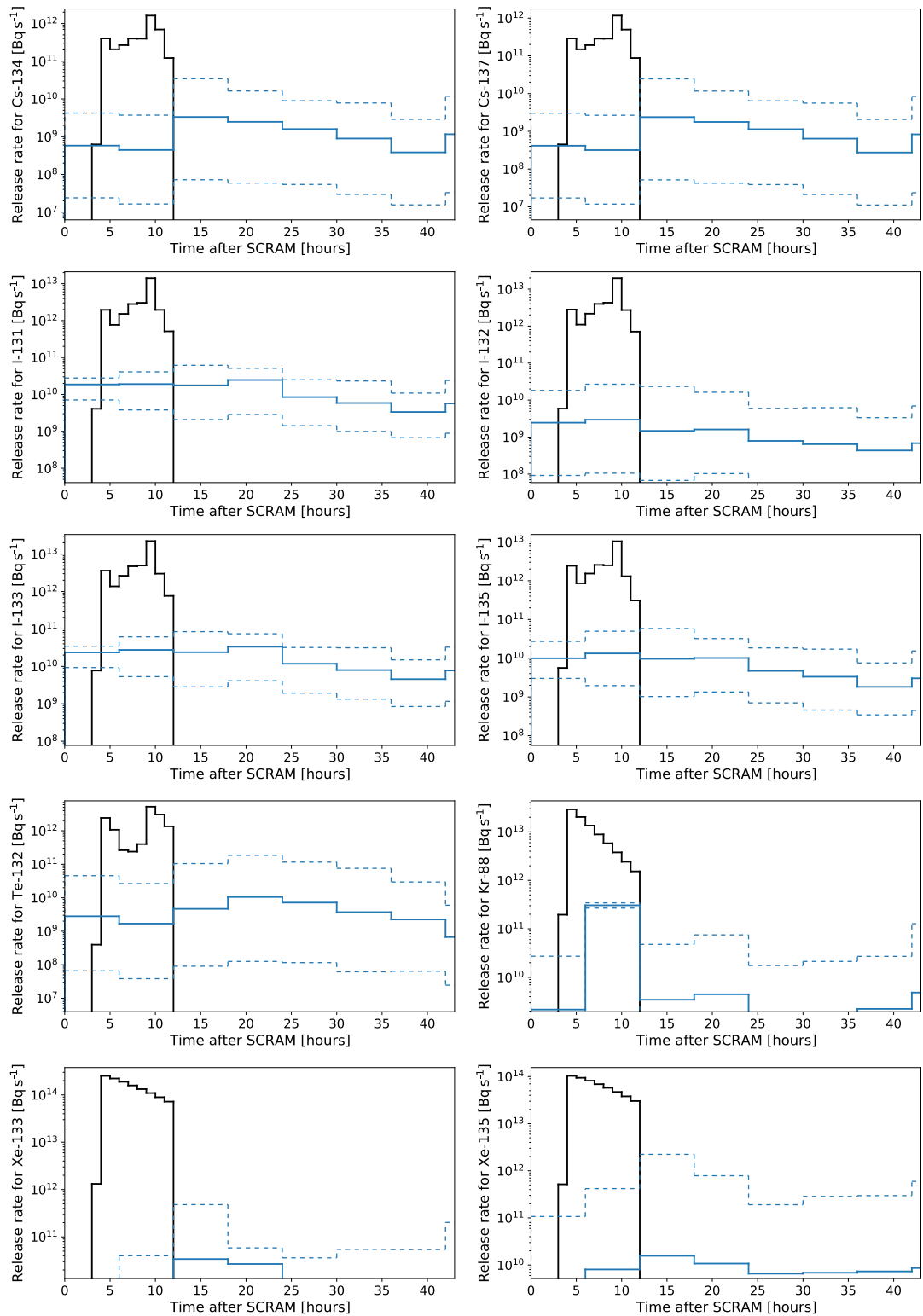
Figure 3.1: Release rates for each radionuclide in each 6-hour time bin (including gamma dose rates). The solid blue lines show the medians of the marginal distributions, while the dashed blue lines show the 10th and 90th percentiles. For comparison, the solid black lines show the true release profile. The minimum value on the y-axis is set to 10% of the lowest true release rate, which means that predicted release rates below this limit are not shown in the plot. The figure is from Sørensen et al. (2023).
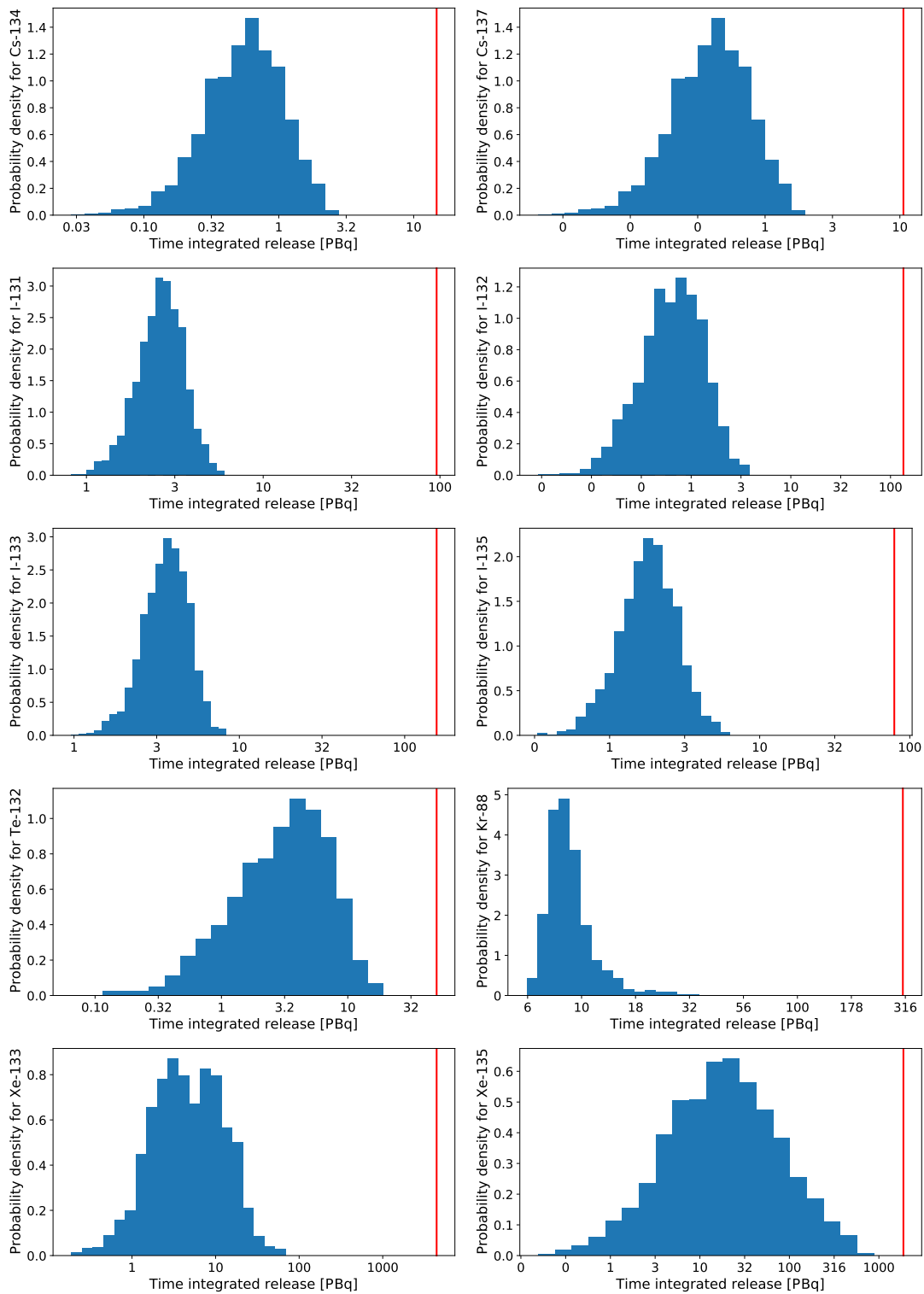
Figure 3.2: Probability density for each radionuclide as a function of time-integrated release (including gamma dose rates). The vertical red lines show the actual released amounts. The figure is from Sørensen et al. (2023).
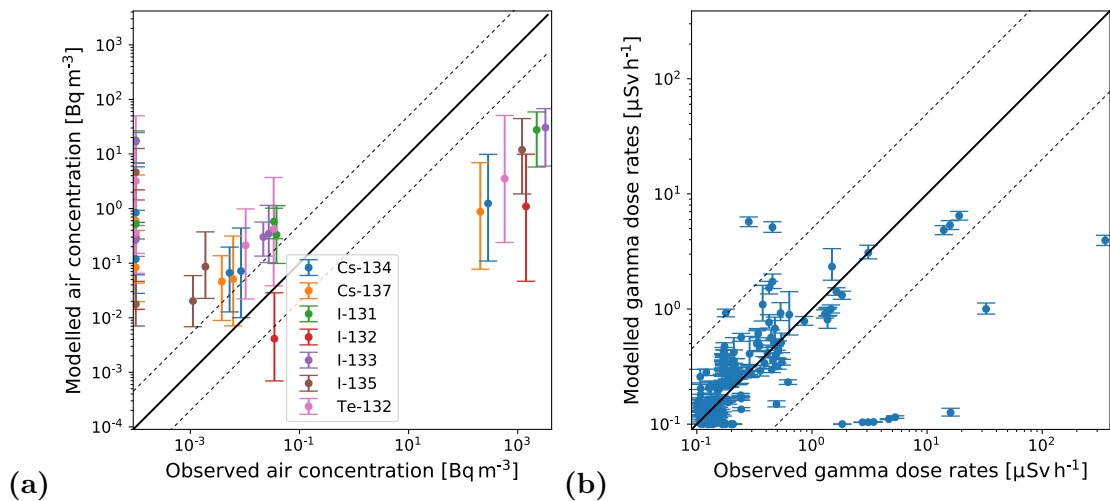
Figure 3.3: Model predictions based on the estimated source term on the y-axis (median and 10th and 90th percentile), and observations on the x-axis (including gamma dose rates). The solid black lines indicate a perfect correlation, while the dashed black lines indicate a factor of 5 between model and observation. **(a)** shows the filter measurements, and **(b)** shows the gamma dose rates. The figure is from Sørensen et al. (2023).

to Figure 8 in the article). There appears to be little or no correlation between the modelled air concentrations and the observed values. However, given the small number of filter measurements and the large number of gamma dose rates, it seems reasonable that the likelihood will be dominated by the latter. This interpretation is supported by the fact that the observed gamma dose rates are, at least to some extent, replicated by the model as seen in Figure 3.3b.

It seems that to reproduce the observed gamma dose rates, the estimated source term must comprise release rates that are systematically underestimated. This suggests a significant discrepancy between the gamma dose rates generated by the two different model systems. This is further investigated in Chapter 3.3.4, but first, we will attempt to apply the same method for source term estimation but based only on the filter measurements.

3.3.3 Source term estimation, not including gamma dose rates

When using filter measurements only, gasses cannot be included in the source term because they are not captured by the filters. Further, as discussed in the article, one of the main reasons for including gamma dose rates in the first place is that very few filter measurements will be available at this early stage. During the simulation period, only two measurements are available from each of the five filter stations. This provides ten 24-hour average air concentrations for each particle, of which most are below the assumed detection limit. In practice, the effective number of observations is higher for some nuclides, because of the constraints imposed by the isotopic ratios. However, in any case, the amount of data is very limited, and the problem is likely to be ill-conditioned.

Figure 3.4 and 3.5 show the estimated release rates and the corresponding histograms of the total released amounts. Compared to Figures 3.1 and 3.2, the estimated release rates based only on filter measurements are much better constrained for all nuclides from 6 to 12 hours. Thus, the timing of the release seems to be described reasonably well,
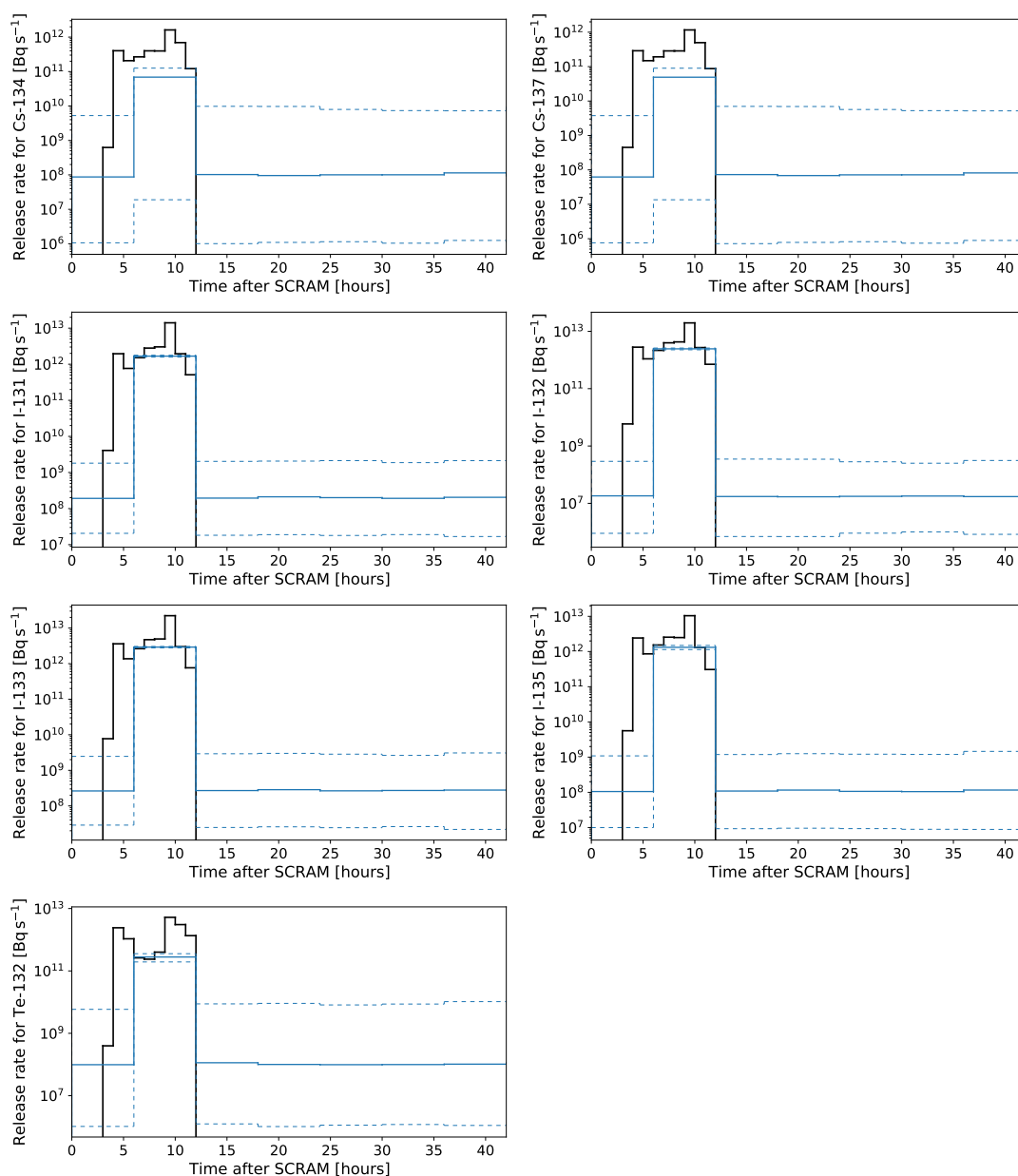
Figure 3.4: Release rates for each radionuclide in each 6-hour time bin (not including gamma dose rates). The solid blue lines show the medians of the marginal distributions, while the dashed blue lines show the 10th and 90th percentiles. For comparison, the solid black lines show the true release profile. The minimum value on the y-axis is set to 10% of the lowest true release rate, which means that predicted release rates below this limit are not shown in the plot. The figure is from Sørensen et al. (2023).

although the magnitude of the release is still underestimated as seen from the histograms in Figure 3.5. The release rates in the remaining time bins are entirely unconstrained, resulting in the posterior distribution being essentially identical to the prior distribution for each nuclide. However, this outcome is expected when there is insufficient data to constrain the source term.
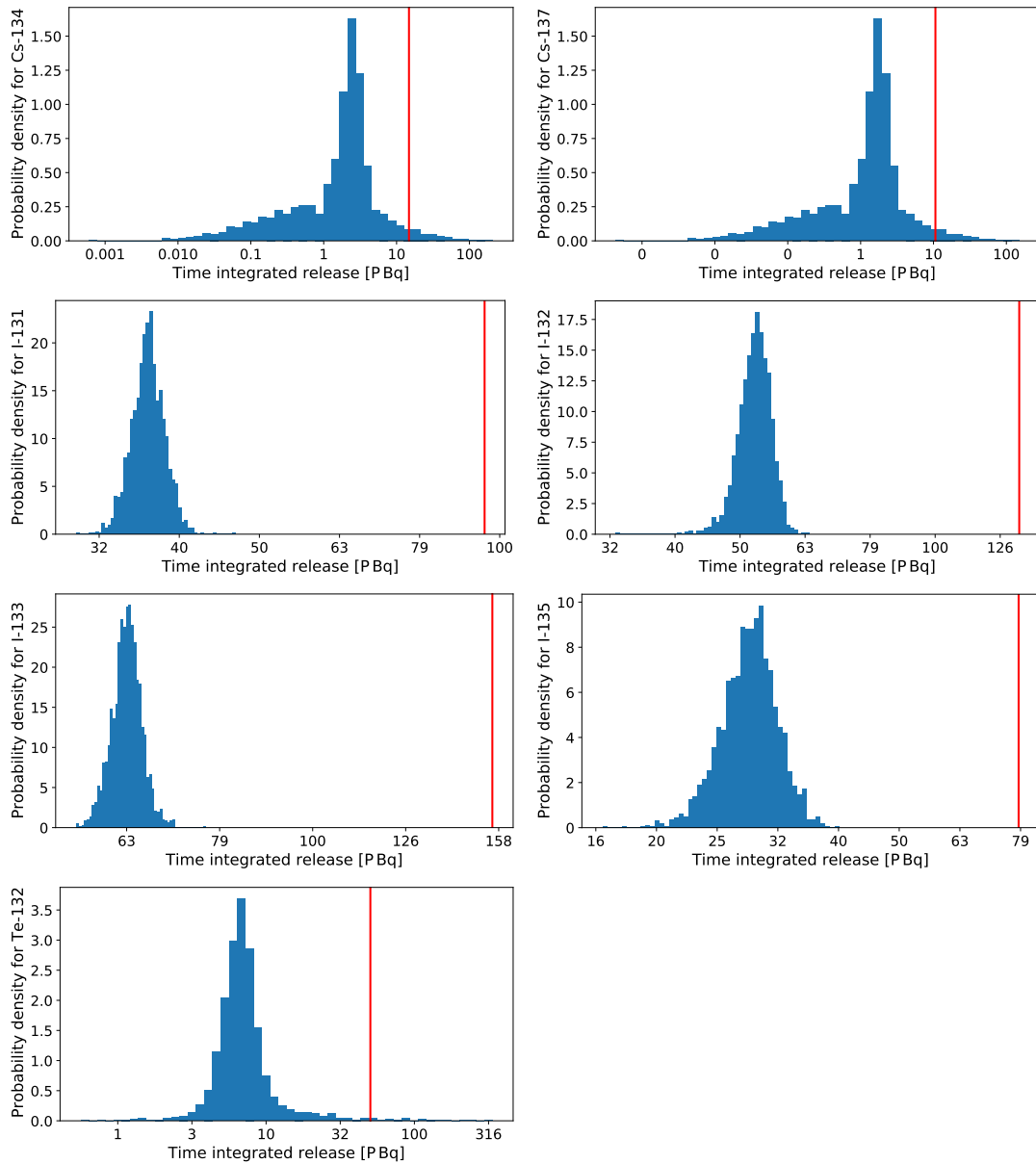
Figure 3.5: Probability density for each radionuclide as a function of time-integrated release (not including gamma dose rates). The vertical red lines show the actual released amounts. The figure is from Sørensen et al. (2023).

Figure 3.6 shows the predicted concentrations as a function of observations. It shows that for most nuclides, there is exactly one measurement that is predicted almost perfectly, while the remaining are quite far from the true values. Further, the measurements that are determined well are several orders of magnitude larger than the remaining. Thus, this suggests that the method has effectively estimated each release rate to match the single high-value observation available for each nuclide. The pattern looks slightly different for the caesium-nuclides, because of the prior distribution defined in Eq. (7) based on the constraints in Eq. (6) in the article. As discussed previously, these constraints effectively increase the number of measurements for nuclides connected via the isotopic ratios.
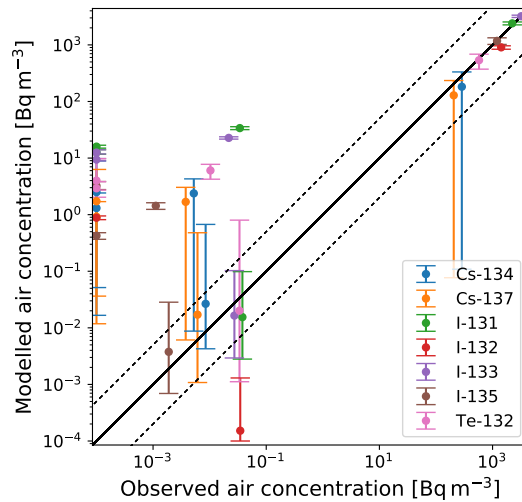
Figure 3.6: Model predictions based on the estimated source term on the y-axis (median and 10th and 90th percentile), and observations on the x-axis (not including gamma dose rates). The solid black lines indicate a perfect correlation, while the dashed black lines indicate a factor of 5 between model and observation. The figure is from Sørensen et al. (2023).

3.3.4 Discrepancy between models

To further investigate why the gamma dose rates do not seem to be useful for source term estimation when using the SILAM-generated observations, we compare the predicted gamma dose rates from the two model systems when imposing the true source term. Figure 3.7 shows two different comparisons of the gamma dose rates from the two model systems; 3.7a shows the DERMA+ARGOS gamma dose rates as a function of those predicted by the SILAM model, and 3.7b shows the histograms of the two distributions. It is evident from these plots that the gamma dose rates predicted by DERMA+ARGOS are consistently much higher than those predicted by the SILAM model. In fact, there appears to be an average difference of two orders of magnitude between them.

This naturally explains why the predicted source term systematically underestimates all releases, but the magnitude of the difference is also somewhat concerning. However, further exploring the causes of this difference is beyond the scope of this thesis. Instead, a few discussion points and possible explanations are listed below, and based on that we can attempt to formulate suggestions that can help avoid this in future work or, at least, help better understand the cause.

- The two meteorological data sets use different horizontal resolutions, 2.5 km for DERMA+ARGOS and 5 km for SILAM. Since the Loviisa nuclear power plant is located near the coast, it is not unlikely that local sea breeze effects play a role, and these might not be resolved equally well by the two models.

- The dispersion models might have different tendencies to either overestimate or underestimate diffusion. The different concentration fields will then cause different gamma dose rate patterns. Further, for reasons that will be discussed extensively in Chapter 4, the current version of DERMA does not always perform well in the short-range regime and it is therefore not unlikely that the model has biases near

the source.

- The gamma dose rate models make different assumptions and may therefore also, in principle, produce different gamma dose rates, even provided the exact same concentration field.

Thus, the bias in the gamma dose rates may either be caused by differences in the meteorological data, differences in the dispersion models used, differences in the gamma dose rate models used, or any combination thereof. Although there are large sources of uncertainty in essentially all parts of the modelling, it does not seem likely that any of the explanations above can explain a mean bias this large on its own.

To investigate the cause, a comprehensive comparison should be conducted, altering only one model variable between the two data sets. For instance, variations in meteorological data, dispersion models, or gamma dose rate models could be examined independently. Ideally, all three combinations should be explored to examine if a systematic bias exists in any of the models. If the observed bias can only be explained by the combined effect of several model biases, then releasing the same source under different weather conditions could help determine if the pattern is persistent.

Regardless of the explanation, it is evident that under these specific conditions, emergency preparedness authorities in Denmark and Finland would predict significantly different levels of gamma doses, provided the same source term and start time.
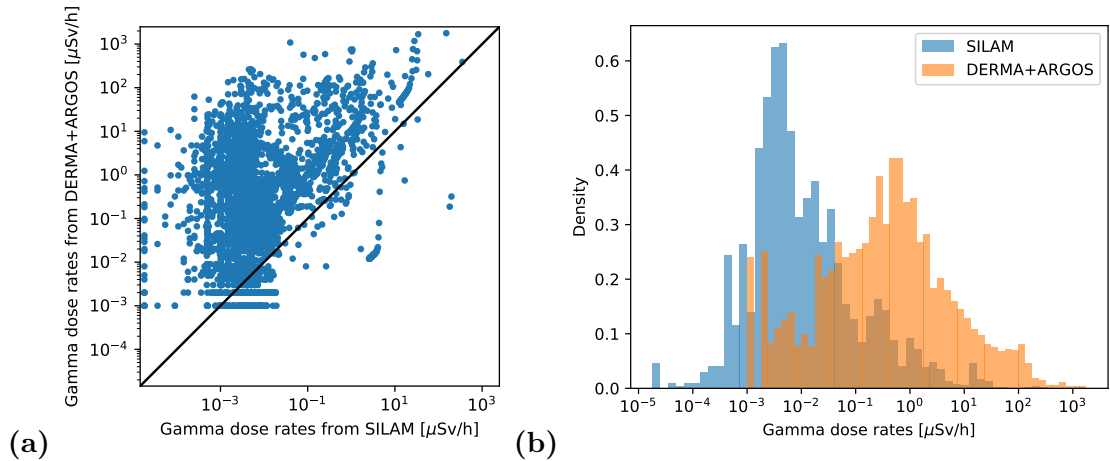

Figure 3.7: The plots show two different comparisons of the gamma dose rates from the two models, where the DERMA+ARGOS gamma dose rates are obtained by imposing the true source term. **(a)** gamma dose rates from DERMA+ARGOS vs gamma dose rates from SILAM. **(b)** histograms showing gamma dose rates from both models. The figure is from Sørensen et al. (2023).

References

Hoffman, M. D., Gelman, A., et al. (2014). The no-u-turn sampler: adaptively setting path lengths in hamiltonian monte carlo. *J. Mach. Learn. Res.*, 15(1):1593–1623.

Koo, Y.-H., Yang, Y.-S., and Song, K.-W. (2014). Radioactivity release from the fukushima accident and its consequences: A review. *Progress in Nuclear Energy*, 74:61–70.

Kovalets, I. V., Romanenko, O., and Synkevych, R. (2020). Adaptation of the rodos system for analysis of possible sources of ru-106 detected in 2017. *Journal of environmental radioactivity*, 220:106302.

Le Brazidec, J. D., Bocquet, M., Saunier, O., and Roustan, Y. (2020). Mcmc methods applied to the reconstruction of the autumn 2017 ruthenium-106 atmospheric contamination source. *Atmospheric Environment: X*, 6:100071.

Liu, Y., Haussaire, J.-M., Bocquet, M., Roustan, Y., Saunier, O., and Mathieu, A. (2017). Uncertainty quantification of pollutant source retrieval: comparison of bayesian methods with application to the chernobyl and fukushima daiichi accidental releases of radionuclides. *Quarterly Journal of the Royal Meteorological Society*, 143(708):2886–2901.

Saunier, O., Didier, D., Mathieu, A., Masson, O., and Le Brazidec, J. D. (2019). Atmospheric modeling and source reconstruction of radioactive ruthenium from an undeclared major release in 2017. *Proceedings of the National Academy of Sciences*, 116(50):24991–25000.

Saunier, O., Korsakissok, I., Didier, D., Doursout, T., and Mathieu, A. (2020). Realtime use of inverse modeling techniques to assess the atmospheric accidental release of a nuclear power plant. *Radioprotection*, 55:107–115.

Saunier, O., Mathieu, A., Didier, D., Tombette, M., Quélo, D., Winiarek, V., and Bocquet, M. (2013). An inverse modeling method to assess the source term of the fukushima nuclear power plant accident using gamma dose rate observations. *Atmospheric Chemistry and Physics*, 13(22):11403–11421.

Sofiev, M., Vira, J., Kouznetsov, R., Prank, M., Soares, J., and Genikhovich, E. (2015). Construction of the silam eulerian atmospheric dispersion model based on the advection algorithm of michael galperin. *Geoscientific Model Development*, 8(11):3497–3522.

Sørensen, J., Feddersen, H., Tølløse, K., Uppstu, A., Klein, H., Ulimoen, M., Robertson, L., Pehrsson, J., Lauritzen, B., Hac-Heimburg, A., Roed, H., Améen, E., Syed, N., Blixt Buhr, A., Lindgren, J., and Peltonen, T. (2023). *SOurce CHAracterizatiOn accounting for meTeorologIcal unCertainties (SOCHAOTIC) – final report: Final report of the NKS-B SOCHAOTIC activity*. NKS Secretariat. Report no NKS-470.

Sørensen, J. H. (2018). Method for source localization proposed and applied to the october 2017 case of atmospheric dispersion of ru-106. *Journal of environmental radioactivity*, 189:221–226.

Stohl, A., Seibert, P., Wotawa, G., Arnold, D., Burkhart, J. F., Eckhardt, S., Tapia, C., Vargas, A., and Yasunari, T. J. (2012). Xenon-133 and caesium-137 releases into the atmosphere from the fukushima dai-ichi nuclear power plant: determination of the source term, atmospheric dispersion, and deposition. *Atmospheric Chemistry and Physics*, 12(5):2313–2343.

Terada, H., Nagai, H., Tsuduki, K., Furuno, A., Kadowaki, M., and Kakefuda, T. (2020). Refinement of source term and atmospheric dispersion simulations of radionuclides during the fukushima daiichi nuclear power station accident. *Journal of environmental radioactivity*, 213:106104.

Tomas, J. M., Peereboom, V., Kloosterman, A., and van Dijk, A. (2021). Detection of radioactivity of unknown origin: Protective actions based on inverse modelling. *Journal of environmental radioactivity*, 235:106643.

Tølløse, K. S., Kaas, E., and Sørensen, J. H. (2021). Probabilistic inverse method for source localization applied to etex and the 2017 case of ru-106 including analyses of sensitivity to measurement data. *Atmosphere*, 12(12).

Tølløse, K. S. and Sørensen, J. H. (2022). Bayesian inverse modelling for probabilistic multi-nuclide source term estimation using observations of air concentration and gamma dose rate. *Atmosphere*, 13(11).

Winiarek, V., Bocquet, M., Saunier, O., and Mathieu, A. (2012). Estimation of errors in the inverse modeling of accidental release of atmospheric pollutant: Application to the reconstruction of the cesium-137 and iodine-131 source terms from the fukushima daiichi power plant. *Journal of Geophysical Research: Atmospheres*, 117(D5).

Chapter 4

Improved description of turbulent diffusion in DERMA

4.1 Paper 3: A New Hybrid Particle-Puff Approach to Atmospheric Dispersion Modelling, Implemented in the Danish Emergency Response Model of the Atmosphere (DERMA)

The manuscript describes the developments made to enable DERMA's application in short-range dispersion modelling. It is intended for submission after the hand-in of the PhD thesis.

The most important part of the work presented in this manuscript is a reformulation of the turbulence description in DERMA. This new description features a more advanced stochastic transport scheme that divides the turbulent diffusion into two parts: puff-growth, and stochastic displacement. This serves multiple purposes; for small puffs, it ensures that the puffs only grow due to eddies smaller than the puff itself, while larger eddies instead advect the puffs. For large puffs, on the other hand, the stochastic displacement allows puffs to be exposed to vertical wind shear. In addition, two plume rise algorithms have been implemented in order to better estimate the effective initial height in scenarios involving heat release.

Although this new hybrid formulation is developed with the existing framework of DERMA in mind, the methodology is generally applicable and could be implemented in any similar puff model. Hence, in this study, the implementation in DERMA serves as a case study, demonstrating the capabilities of this new turbulence description.

In addition, the new turbulence description is evaluated by comparing model predictions to observations from three different tracer gas experiments, specifically selected to

pose different challenges to the model: ETEX, the Øresund experiment, and the Kincaid experiment. The results show that the new version of DERMA consistently performs better than the currently operational version, especially in the short-range regime.

4.1. PAPER 3: A NEW HYBRID PARTICLE-PUFF APPROACH TO ATMOSPHERIC DISPERSION MODELLING, IMPLEMENTED IN THE DANISH EMERGENCY RESPONSE MODEL OF THE ATMOSPHERE (DERMA)

A New Hybrid Particle-Puff Approach to Atmospheric Dispersion Modelling, Implemented in the Danish Emergency Response Model of the Atmosphere (DERMA)

Kasper Skjold Tølløse[1,2] and **Jens Havskov Sørensen**[1]

[1]Danish Meteorological Institute
[2]Niels Bohr Institute, University of Copenhagen

Correspondence: Kasper Skjold Tølløse (ktoe@dmi.dk)

Abstract. The Danish Emergency Response Model of the Atmosphere (DERMA) is a Lagrangian puff model originally developed for long-range dispersion modelling, on distances longer than roughly 50 km from the source, e.g. in case of nuclear disasters. The model is used operationally as part of Danish emergency preparedness for the prediction of atmospheric dispersion in case of nuclear accidents, airborne spread of animal diseases, and ash from volcanic eruptions. To be able to simulate dispersion on shorter spatial scales, a new description of turbulent diffusion has been developed and implemented in DERMA, combining a stochastic particle approach with a classic puff model. Further, updates have been made to the parameterizations of the turbulent wind fluctuations and Lagrangian time scales, the boundary layer height, and the initial plume rise due to heat release. This allows for a more realistic description of turbulent diffusion near the release location, while an updated version of the existing turbulence description is still used at longer distances. DERMA is then evaluated against three different tracer gas experiments: the European Tracer Experiment (ETEX), the Øresund experiment, and the Kincaid experiment. The comparison shows that the new hybrid approach gives more accurate predictions, especially on shorter spatial scales, but a small improvement is also observed for long-range dispersion.

1 Introduction

Lagrangian atmospheric dispersion models can be divided into two categories, stochastic particle models and puff models. Both rely on modelling the positions of particles following Lagrangian trajectories. In stochastic particle models, each particle follows a turbulent trajectory estimated using stochastic differential equations, and the resulting concentration field is then determined by the spread of particles. These models typically make as few assumptions as possible and therefore their behavior should in principle be the most physically accurate. Some examples are the models FLEXPART (Stohl et al., 2005; Pisso et al., 2019), NAME (Jones et al., 2004), and HYSPLIT (Draxler and Hess, 1997). However, Jones et al. (2004) argues that the stochastic particle formulation is not ideal near the release location, because the very fine three-dimensional structures of the plume require a large number of particles to be resolved sufficiently, and too few particles may instead introduce statistical noise. Thus, NAME uses a hybrid particle-puff description for short-range modelling, while on longer distances the particles are assumed to be point concentrations (Jones et al., 2004). In any case, however, a large number of particles is needed, which makes this type of model computationally expensive. Further, as discussed by Stohl et al. (2005), short advection time steps, on the order of a few seconds, may be necessary in order to correctly resolve the turbulent trajectories in all conditions.

Lagrangian puff models are a computationally cheaper alternative, where each puff instead follows the average wind field, and turbulent diffusion is assumed to follow a Gaussian distribution locally around each puff's centroid. Some examples are the models CALPUFF (Scire et al., 2000), DIPCOT (Andronopoulos et al., 2009), RIMPUFF (Thykier-Nielsen et al., 1999), and DERMA (Sørensen et al., 2007). In this type of model, much fewer particles are used compared to the stochastic particle models, and the Gaussian concentration distributions then "fill the gaps" between particle locations. For relatively young puffs, this assumption works quite

well, but when the puffs grow beyond a certain size, the vertical wind shear may cause puffs to stretch over different flow regimes, which would in reality distort the Gaussian shape (Jones et al., 2004). A typical solution for this problem, used in e.g. NAME, CALPUFF, and RIMPUFF, is the use of puff splitting, i.e. a puff that grows too large is split into several smaller puffs at different heights (Jones et al., 2004; Scire et al., 2000; Thykier-Nielsen et al., 1999). This ensures a more physical behavior, but it introduces new challenges due to the continuously increasing number of puffs (Draxler and Hess, 1997).

Some puff models such as DIPCOT and DERMA also combine the puff approach with a stochastic displacement of puffs (Andronopoulos et al., 2009; Sørensen et al., 2007). Another example of a hybrid formulation is the Puff-Particle-Model (PPM) suggested by De Haan and Rotach (1998). In this approach, the turbulent effects are separated into two distinct physical processes, a meandering part (larger scale than the puff) and a relative dispersion around each puff centroid, represented by the puff growth. However, in order to keep puffs smaller than the meandering scales, PPM uses more puffs and more frequent puff splitting than in regular puff models and should be thought of as something halfway between a stochastic particle model and a puff model (De Haan and Rotach, 1998).

In the current version of DERMA, complete mixing throughout the boundary layer is assumed, which means that the concentration field of a puff is only assumed Gaussian horizontally, while it is described by a uniform distribution vertically for puffs inside the PBL. Thus, according to the arguments above, the puffs in DERMA are likely to stretch over different flow regimes. However, a vertical stochastic transport scheme inside the PBL is used as an alternative to puff splitting, i.e. randomly moving the centroid of the puff to a new vertical position will allow the puff to experience the vertical wind shear over time (Sørensen, 1998; Sørensen et al., 2007). Despite the relatively simple formulation, DERMA was part of the ETEX model evaluation program, where it ranked as one of the best performing models (Graziani et al., 1998).

DERMA is currently used operationally for a number of purposes for Danish emergency preparedness including nuclear accidents, volcanic eruptions, and airborne animal diseases (Sørensen et al., 2000, 2001; Mikkelsen et al., 2003; Gloster et al., 2010; Hoe et al., 2002). In recent years, the model has further been used in different research projects about inverse modelling for source localization and source term reconstruction from a nuclear accident (Sørensen, 2018; Tølløse et al., 2021; Tølløse and Sørensen, 2022).

The current version of DERMA is specifically designed for long-range dispersion modelling, and some assumptions are not applicable on shorter scales. Thus, the aim of this study is to develop a new description of turbulent diffusion, which enables DERMA to accurately predict dispersion closer to the release location.

In this study, we develop a new hybrid particle-puff approach, which separates the turbulent diffusion in a stochastic part and a puff part. On shorter scales, the separation is based on the size of the puff compared to the length scale associated with the largest turbulent eddies. This is conceptually similar to the approach by De Haan and Rotach (1998) used in the PPM. However, on longer scales, the stochastic part works as compensation for the fact that the puff assumption fails for physically large puffs, similar to the formulation in the current version of DERMA. In addition to the new description of turbulent diffusion, several updates have been made to DERMA, which are described in detail in Section 2. Further, the new particle-puff approach has been evaluated against three tracer gas experiments; the European Tracer Experiment (ETEX), the Øresund experiment, and the Kincaid experiment. Details on the evaluation process and the results are presented in Section 3. Finally, a summary and the conclusions are presented in Section 4.

2   Model description

In this section, a detailed description of all the new elements in DERMA is given. For a more general description of the current version of DERMA, see Sørensen (1998); Baklanov and Sørensen (2001); Sørensen et al. (2007). In Section 2.1, the new hybrid particle-puff formulation is described. Next, Section 2.2 describes the updates made to the PBL parameterization including a new parameterization of turbulent wind fluctuations, Lagrangian time scales, and PBL height. Finally, Section 2.3 describes the Concawe and Briggs plume rise algorithms, which have also been implemented.

2.1   Hybrid particle-puff description

As discussed previously, one of the shortcomings of the puff model approach is that puffs will eventually grow larger than the characteristic length scale of the vertical wind shear, causing the puff assumption to fail. Further, the smallest puffs may be smaller than the largest turbulent eddies in some conditions. Therefore, theoretically, at the early stages, the puffs should be displaced by these, until they grow larger than the eddies themselves. In this study, we develop a simple hybrid approach, which attempts to target both of these issues. For small puffs, the hybrid approach is designed such that puffs are displaced by the largest eddies, while smaller eddies cause the puffs to grow, and for large puffs, the stochastic part will expose puffs to the wind shear without the need for puff splitting.

As in the current version of DERMA, the puffs grow according to the formulation by (Gifford, 1984)

$$\sigma_i^2 = 2K_i t_{L_{u_i}} \left\{ \tau_i - \left(1 - e^{-\tau_i}\right) - \frac{1}{2}\left(1 - e^{-\tau_i}\right)^2 \right\}, \qquad (1)$$

where σ_i is the puff's standard deviation along the x_i-axis, K_i is the turbulent diffusivity, $t_{L_{u_i}}$ is the Lagrangian time

scale, i.e. the auto-correlation time for the velocity fluctuations, t is the age of the puff, and $\tau_i = t/t_{L_{u_i}}$. However, to allow K_i and $t_{L_{u_i}}$ to be time-dependent, we instead consider the time derivative of Equation (1)

$$\frac{\partial}{\partial t}\sigma_i^2 = 2\sigma_{u_i}^2 t_{L_{u_i}}\left(1 - e^{-\tau_i}\right)^2,$$

where we have used the relation between the diffusivity and the turbulent velocity scale $K_i = \sigma_{u_i}^2 t_{L_{u_i}}$. This can be written in the numerical form

$$\Delta\sigma_i^2(t + \Delta t/2) = 2\sigma_{u_i}^2(t)t_{L_{u_i}}(t)\Delta t\left(1 - \exp\left(-\frac{t + \Delta t/2}{t_{L_{u_i}}(t)}\right)\right)^2,$$
(2)

which is evaluated at the time $t + \Delta t/2$, i.e. halfway between the two neighboring time steps. However, to avoid double-counting the effects of turbulence, Eq. (2) should describe the combined effects of the puff growth and stochastic parts of the turbulent diffusion.

To find a suitable formulation, we consider the case where puffs have been dispersed around a point following mean wind trajectory $\mathbf{x}_t$ and assume that the puff centroids, $\mathbf{x}_p$, are distributed according to Gaussian particle distributions in all three spatial dimensions. Thus, along the x_i-axis puff centroids are distributed as $f(x_i) = \mathcal{N}(x_{i,t}, \sigma_{i,part})$. Further, the concentration field from each puff around its centroid is assumed to follow the Gaussian distribution $g(x_i) = \mathcal{N}(0, \sigma_{i,puff})$. The resulting concentration distribution can be obtained by calculating the convolution of the two distributions

$$f(x_i) \circledast g(x_i) = \int\limits_{-\infty}^{\infty} f(x_i')g(x_i - x_i')\mathrm{d}x_i'.$$

Further, it can be shown that (Bromiley, 2003)

$$f(x_i) \circledast g(x_i) = \mathcal{N}\left(x_{i,t}, \sqrt{\sigma_{i,part}^2 + \sigma_{i,puff}^2}\right).$$

Now, we want to impose the requirement that the resulting concentration distribution is identical to the Gaussian distribution $\mathcal{N}(x_{i,t}, \sigma_i)$, with σ_i from Eq. (1), in accordance with the formulation by Gifford (1984). To ensure this, the increment of the variances for the distributions $f(x_i)$ and $g(x_i)$ must fulfill the following requirement at every numerical time step

$$\Delta\sigma_{i,puff}^2 = \beta_i^2 \Delta\sigma_i^2,$$
$$\Delta\sigma_{i,part}^2 = (1 - \beta_i^2)\Delta\sigma_i^2,$$
(3)

where $\Delta\sigma_i^2$ is given by Eq. (2), and $\beta_i \in [0,1]$ is a parameter determining how much stochastic movement is used. If $\beta_i = 1$, the model is a classical puff model, while in the case $\beta_i = 0$, the turbulent diffusion is described purely by the stochastic transport and the puffs keep their initial sizes.

For the variance of the Gaussian particle distribution $f(x_i)$ to increase with $\Delta\sigma_{i,part}^2$ for each iteration, the step size of the random walk must be $\Delta\sigma_{i,part}$.

If the turbulence is Gaussian and if there is no vertical wind shear, the two approaches (puff vs particle) are equivalent, and any combination of the two (i.e. any value of β_i) should be valid, given of course that there is a sufficient number of particles. However, since vertical wind shear is a very fundamental feature of the atmosphere, especially in the PBL, adding a stochastic element to the turbulence description should improve the performance by exposing puffs to the winds at different heights.

2.1.1 Determining β_i

Early in the life of a puff, the puff might be smaller than the turbulent eddies themselves, and therefore we can make a physical distinction between the particle part and the puff part. Although our approach is different, this is conceptually similar to the approach by De Haan and Rotach (1998). Here, we use the fraction of the turbulent kinetic energy (TKE) on larger scales than the puff itself. Thus, we first consider the TKE spectrum (Kolmogorov, 1941)

$$TKE(k) \propto \varepsilon^{2/3}k^{-5/3},$$
(4)

where ε is the TKE dissipation rate, $k = \frac{2\pi}{\lambda}$ is the wave number, and the wavelength λ corresponds to the length scale associated with the turbulent eddies. In reality, $k = |\mathbf{k}|$, where $\mathbf{k}$ is the three-dimensional wave number, which is of course not necessarily equal in all physical dimensions. However, for this purpose, we assume that the relation (4) holds in each spatial dimension individually. Thus, assuming that the puff has the spatial extent σ_i along the x_i-axis, we can estimate the fraction of the TKE accounted for by eddies on smaller spatial scales than the puff itself

$$\frac{TKE_{puff}}{TKE} = \frac{\int_{\frac{2\pi}{\sigma_i}}^{\infty} TKE(k_i)\mathrm{d}k_i}{\int_{\frac{2\pi}{l_i}}^{\infty} TKE(k_i)\mathrm{d}k_i} = \left(\frac{\sigma_i}{l_i}\right)^{2/3},$$
(5)

where l_i is the length scale associated with the largest eddies along the i'th physical dimension, which is estimated as $l_i = \sigma_{u_i}t_{L_{u_i}}$.

The fraction in Eq. (5) seems like a natural choice for the value of β_i^2, except that when the puff grows larger than the largest eddies, the particle part will then naturally die out. Thus, to ensure that the stochastic part does not vanish, we define

$$\beta_i = \max\left(\beta_{\min}, \left(\frac{\sigma_i}{l_i}\right)^{1/3}\right),$$
(6)

where $\beta_{\min} \in [0,1]$ is a hyperparameter that needs to be determined to find the ideal balance between the particle and puff parts. We have found that $\beta_{\min} = \sqrt{1/2}$, which divides

the turbulence evenly between the particle part and the puff part, gives good results.

It is assumed that puffs inside the boundary layer are reflected both at the surface and at the PBL top. Further, for puffs above the boundary layer, the stochastic part will automatically be turned off by setting $\beta_i = 1$.

2.1.2   Short-range and long-range formulations

The concentration field from a puff in a point (x_p, y_p, z_p) can be written as

$$C_p = \frac{Q_p}{2\pi\sigma_y^2\sigma_z}\exp\left\{-\frac{1}{2}\left(\frac{x-x_p}{\sigma_y}\right)^2 - \frac{1}{2}\left(\frac{y-y_p}{\sigma_y}\right)^2 - \frac{1}{2}\left(\frac{z-z_p}{\sigma_z}\right)^2\right\}, \tag{7}$$

where Q_p is the mass/activity carried by the puff. However, when a puff has grown to a certain size compared to the PBL height, the current DERMA assumption of complete mixing is adapted, i.e. a uniform distribution is assumed vertically. This happens whenever $\sigma_z \geq h/\alpha$, where h is the PBL height, and α is another hyperparameter determining how fast a puff is assumed to fill out the boundary layer. We found that $\alpha = 2$ gives good results, which means that complete mixing is assumed when $2\sigma_z$ exceeds the PBL height. Whenever a puff fulfills this requirement, the concentration field becomes

$$C_p = \frac{Q_p}{2\pi\sigma_y^2 h}\exp\left\{-\frac{1}{2}\left(\frac{x-x_p}{\sigma_y}\right)^2 - \frac{1}{2}\left(\frac{y-y_p}{\sigma_y}\right)^2\right\}\delta(z,h), \tag{8}$$

where $\delta(z,h) = \begin{cases} 1 & \text{if } z \leq h \\ 0 & \text{if } z > h \end{cases}$.

When the complete mixing state is reached, the puff is assumed to fill out the boundary layer at all later times, even when the boundary layer grows. Further, since the puff is no longer growing vertically, all turbulence is assumed to go to the stochastic movement, i.e. we set $\beta_z = 0$. Only if the center of a completely mixed puff escapes the boundary layer, it will transform back to a Gaussian form in the vertical dimension.

This long-range formulation is similar to that of the current version of DERMA but with the improved stochastic transport scheme described above, whereas the existing version simply assigns a new random height to each puff inside the PBL at every time step (Sørensen et al., 2007).

2.2   Parameterization of boundary layer parameters

The calculation of both the puff part and particle part described above depends on $\sigma_{u_i}^2$ and $t_{L_{u_i}}$, which in turn depend on several boundary layer parameters that are either imported or calculated in DERMA.

From the output of the numerical weather prediction (NWP) model, DERMA imports instantaneous turbulent fluxes of momentum, τ, and sensible and latent heat, Q_s and Q_l. From these, the following parameters are calculated

(Zannetti, 2013, Ch. 3)

$$L = -\frac{u_*^3 T_v}{\kappa g \left(\overline{w'\theta_v'}\right)_0}, \tag{9}$$

$$u_* = \sqrt{\frac{\tau}{\rho}}, \tag{10}$$

$$w_* = \left(\frac{hg\left(\overline{w'\theta_v'}\right)_0}{T_v}\right)^{1/3}, \tag{11}$$

where L is the Obukhov length, which is related to the static stability of the boundary layer, and the friction velocity u_* is assumed the fundamental velocity scale of the non-convective turbulent boundary layer, whereas w_* is the convective velocity scale. Further, ρ is the air density, $g = 9.81$ ms^{-2} is the gravitational acceleration constant, $\kappa = 0.4$ is the von Karman constant, T_v is the surface virtual temperature, and h is the PBL height, which is calculated as described in Section 2.2.1. Finally, $\left(\overline{w'\theta_v'}\right)_0$ is the surface buoyancy flux, i.e. the flux of virtual potential temperature, which can be estimated directly from the imported heat fluxes as $\left(\overline{w'\theta_v'}\right)_0 = (Q_s + 0.07Q_l)/(\rho c_p)$, where c_p is the heat capacity at constant pressure (Zannetti, 2013, Ch. 3).

2.2.1   PBL height

The PBL height parameterization is based on the approach by Vogelezang and Holtslag (1996), where the inversion layer is reached when a modified form of the Bulk Richardson number exceeds the critical value of 0.25.

$$Ri(z) = \frac{(g/\Theta_{v,s})(\Theta_v(z) - \Theta_{v,s})z}{U(z)^2 + V(z)^2 + 100u_*^2}, \tag{12}$$

where $\Theta_{v,s}$ is the surface virtual potential temperature, $\Theta_v(z)$ is the virtual potential temperature at height z, and $U(z)$ and $V(z)$ are the horizontal wind components at height z. The PBL height h is set equal to the height z where the following requirement is obtained for the first time moving upwards from the ground, $Ri(z) = 0.25$.

2.2.2   Turbulent wind fluctuations

As in the current version of DERMA, the constant turbulent diffusivity $K_y = 6 \cdot 10^3 \text{m}^2\text{s}^{-1}$ and corresponding Lagrangian time scale $\tau_{L_v} = 10^4$ s are assumed for the horizontal diffusion (Sørensen et al., 2007). The vertical component of turbulent velocity fluctuations and the corresponding Lagrangian time scale is parameterized based on Hanna (1984). The formulas are given below for the different stability regimes and are valid for puffs within the PBL. For puffs above the boundary layer, we instead use the constant values $\sigma_w = 0.1$ ms^{-1} and $\tau_{L_w} = 100$ s. In the following, z is the particle's height above the ground, and $f = 10^{-4}$ s^{-1} is the Coriolis parameter, assumed constant with the typical value valid for midlatitudes.

Stable conditions

$$\sigma_w = 1.3u_* \left(1 - \frac{z}{h}\right) \tag{13}$$

$$t_{L_w} = 0.1\frac{h}{\sigma_w}\left(\frac{z}{h}\right)^{0.8} \tag{14}$$

Neutral conditions

$$\sigma_w = 1.3u_*\exp\left(-2\frac{fz}{u_*}\right) \tag{15}$$

$$t_{L_w} = \frac{0.5z/\sigma_w}{1 + 15fz/u_*} \tag{16}$$

Unstable conditions

If $\frac{z}{h} < 0.03$:

$$\frac{\sigma_w}{w_*} = 0.96\left(3\frac{z}{h} - \frac{L}{h}\right)^{1/3} \tag{17}$$

If $0.03 \leq \frac{z}{h} < 0.4$:

$$\frac{\sigma_w}{w_*} = \min\left[0.96\left(3\frac{z}{h} - \frac{L}{h}\right)^{1/3}, 0.763\left(\frac{z}{h}\right)^{0.175}\right] \tag{18}$$

If $0.4 \leq \frac{z}{h} < 0.96$:

$$\frac{\sigma_w}{w_*} = 0.722\left(1 - \frac{z}{h}\right)^{0.207} \tag{19}$$

If $0.96 \leq \frac{z}{h} < 1$:

$$\frac{\sigma_w}{w_*} = 0.37 \tag{20}$$

If $\frac{z}{h} < 0.1$ and $z > -L$:

$$t_{L_w} = \frac{0.1z}{\sigma_w[0.55 - 0.38z/L]} \tag{21}$$

If $\frac{z}{h} < 0.1$ and $z \leq -L$:

$$t_{L_w} = 0.59\frac{z}{\sigma_w} \tag{22}$$

If $\frac{z}{h} \geq 0.1$:

$$t_{L_w} = 0.15\frac{h}{\sigma_w}\left[1 - \exp\left(-5\frac{z}{h}\right)\right] \tag{23}$$

2.3 Plume rise algorithm

Two different plume rise algorithms have been implemented in the DERMA model; the Concawe formula and the Briggs formula. The former has the advantage that it is compatible with the current operational setup of DERMA, while the latter takes into account more meteorological considerations. A good overview and a comparison of the algorithms are given by (Korsakissok and Mallet, 2009). All quantities in the equations below are in SI units.

2.3.1 Concawe formula

The Concawe formula only takes the heat release as input and is, therefore, more general than the Briggs formulas described below. Further, its formulation makes it particularly interesting in the context of the DERMA model, because it can be directly implemented in the current operational setup. The plume rise Δh is calculated as (Brummage, 1968)

$$\Delta h = 0.071\frac{Q_h^{0.55}}{U^{0.67}}, \tag{24}$$

where Q_h is the heat release, and U is the model's horizontal wind speed at the height of the release, i.e. the stack height z_s. In the Kincaid experiment, however, the heat release needs to be calculated from the measurements of the exhaust velocity v_g, the gas temperature T_g, and the temperature of the ambient air T. The heat release is calculated as (Korsakissok and Mallet, 2009)

$$Q_h = 228.19v_gd_s^2(T_g - T), \tag{25}$$

where d_s is the stack diameter.

2.3.2 Briggs formulas

The Briggs formulas are specifically developed for gas being exhausted from a stack, and therefore both the exhaust velocity and the gas temperature are considered explicitly. Further, different formulations are used for different stability conditions. The formulas presented here are from (Briggs, 1965).

First, the static stability parameter s_p and the initial buoyancy flux parameter F_b are defined:

$$s_p = \frac{g}{T}\frac{d\Theta}{dz}, \quad F_b = gv_gd_s^2\frac{T_g - T}{T_g}, \tag{26}$$

where g is the gravitational acceleration constant, and $d\Theta/dz$ is the gradient of the mean potential temperature. Since the algorithm is implemented in DERMA, the ambient air temperature T is here the model temperature instead of the observed as used for calculation of Q_h in Eq. (25).

In all cases, the plume rise is given by

$$\Delta h = \min(\Delta h_1, \Delta h_2), \tag{27}$$

where the stability dependent formulas for Δh_1 and Δh_2 are given below.

Stable conditions

$$\Delta h_1 = 2.6\left(\frac{F_b}{Us_p}\right)^{1/3}$$

$$\Delta h_2 = 4F_b^{1/4}s_p^{-3/8} \tag{28}$$

Unstable and neutral conditions

$$
\Delta h_1 = \left\{ \begin{array}{ll} 21.4 \frac{F_b^{3/4}}{U} & \text{if } F_b < 55 \\[2mm] 38.71 \frac{F_b^{3/5}}{U} & \text{if } F_b \geq 55 \end{array} \right.
$$

$$
\Delta h_2 = \left\{ \begin{array}{ll} 4.3 \left(\frac{F_b}{U w_*^2} \right)^{3/5} h^{2/5} & \text{unstable} \\[2mm] 1.54 \left(\frac{F_b}{U u_*^2} \right)^{2/3} z_s^{1/3} & \text{neutral} \end{array} \right. \qquad (29)
$$

2.3.3 Partial penetration of inversion layer

5 If the plume rise is large enough, or the PBL shallow enough, the plume may be lifted above the inversion layer at the top of the PBL. However, in some cases, the plume may also partially penetrate the inversion layer and leave a part of the plume trapped in the PBL. The formulas presented here are
10 from Hanna and Paine (1989).

The penetration factor P, i.e. the fraction of the plume that penetrates the inversion layer is calculated as

$$
P = 1.5 - \frac{\Delta z}{\Delta h}, \qquad (30)
$$

where Δh is the calculated plume rise and $\Delta z = h - z_s$.
15 Note that the formulation of P allows for negative values as well as values larger than 1. However, as long as $P \leq 0$, the plume stays below the inversion layer, and when $P \geq 1$, the entire plume is above the inversion layer. Thus, only when $\Delta z/1.5 < \Delta h < 2\Delta z$, we need to account for partial pene-
20 tration. When this is the case, the altered plume rise of the part trapped in the boundary layer is given by

$$
\Delta h_{\text{below}} = (0.62 + 0.38P)\Delta z, \qquad (31)
$$

and the effective release rate is $Q_{\text{below}} = Q(1 - P)$. However, Hanna and Paine (1989) do not provide a formula for
25 calculating the height of the penetrating part of the plume. Instead, we assume

$$
\Delta h_{\text{above}} = (1 + 0.38P)\Delta z, \qquad (32)
$$

and the effective release rate $Q_{\text{above}} = QP$, which gives a symmetric behavior around the boundary layer inversion. In
30 practice, this is implemented by releasing the fraction $(1-P)$ of the puffs according to Eq. (31) and the fraction P of the puffs according to Eq. (32).

2.3.4 Initial puff size

Finally, the puffs' initial sizes will also be influenced by the
35 plume rise. These are calculated as (Hanna and Paine, 1989)

$$
\sigma_{y0} = \frac{\Delta h}{3.5},
$$
$$
\sigma_{z0} = \frac{\Delta h}{2}. \qquad (33)
$$

3 Model evaluation

The DERMA model with the new elements described in Section 2 is evaluated against three different tracer gas experi-
40 ments. For comparison, the model performance is compared to that of the current version of DERMA. For simplicity, we will refer to these as the "new" and "old" model versions throughout this section. First, the models are evaluated against the first European Tracer Experiment (ETEX), which
45 has also previously been used for evaluation of DERMA (Graziani et al., 1998). Next, to evaluate the models' performances on shorter spatial scales, we use the Øresund experiment and the Kincaid experiment, which both consist of several releases on different days using varying measurement se-
50 tups. In both experiments, the tracer concentrations are measured at ground level within the first 50 km downstream. The Kincaid experiment further provides a test case for the plume rise algorithms due to the large heat release associated with the release of the tracer. More details on the experiments and
55 the data used are given in Section 3.1, 3.2, and 3.3. Next, Section 3.4 describes the experimental setup, and Section 3.4 presents and discusses the evaluation results.

3.1 The European tracer experiment

The European tracer experiment (ETEX) consisted of two
60 releases, ETEX-1 and ETEX-2 (Graziani et al., 1998; Nodop et al., 1998). In the ETEX-1, which is used in this study, the non-decaying and non-depositing gas perfluoromethylcyclohexane (PMCH) was used as a tracer, and a total of 340 kg of the gas was released to the atmosphere with a constant re-
65 lease rate during a 12-hour period starting at 16.00 UTC on 23 October 1994.

The gas was released near Monterfil in Brittany, France, from 8 meters above the ground, see Figure 1. The gas was then sampled over 30 three-hour intervals by a network of
70 168 ground-level sampling stations distributed in 17 European countries. The ETEX observation data set is available via https://remon.jrc.ec.europa.eu/past_activities/etex/site/index.html (latest access March 12, 2024).

3.2 The Øresund experiment
75

The Øresund experiment consisted of nine non-buoyant sulfur hexafluoride (SF6) releases on different days from 16 May to 14 June 1984 (Mortensen and Gryning, 1989). Six releases were made from Barsebäck in Sweden (from 95 m above the ground), and three from the Gladsaxe mast in Den-
80 mark (from 115 m above the ground), release locations are shown in Figure 1. In each of the releases, the release location was chosen based on the wind direction, such that the tracer was released near the upwind coast of Øresund and was sampled by a network of ground-based stations on the
85 opposite coast. The sampling stations were typically configured in an arc near the coast and one or more arcs further inland. The dataset is thoroughly described by Mortensen and

Gryning (1989) and is publicly available from https://doi.org/10.5281/zenodo.161966 (latest access March 12, 2024).

In this study, we use all the available ground-based measurements, but when possible, measurements adjacent in time are averaged to provide average concentrations over longer time periods. This was done to reduce noise from the relatively short sampling periods (down to 15 m).

3.3 The Kincaid experiment

The Kincaid experiment consists of a series of SF6 releases spread out over three roughly one-month-long periods in 1980 and 1981 (Bowne and Londergan, 1983). The gas was released from the 187 m high stack of the Kincaid power plant, located in Illinois, USA, see Figure 1. In the surrounding area, primarily consisting of flat farmland with some lakes, air concentrations were sampled over one-hour periods by a network consisting of roughly 1500 potential sampling locations distributed in 12 arcs in varying distances from 0.5 km up to 50 km downwind of the source. Not all samplers are active at all times, so the number of measurement locations varies. The SF6 tracer was released through the stack of the power plant, and the high gas temperatures often resulted in a substantial effective plume rise. The gas temperature as well as the exhaust velocity were measured and are available together with relevant meteorological observations from a nearby weather mast (Bowne and Londergan, 1983).

The data is distributed as part of the Model Validation Kit (MVK) described by Olesen (2005), which is available via https://www.harmo.org/kit.php (latest access March 12, 2024). As discussed by Olesen (2005), the concentration patterns are often irregular, with high and low values simultaneously occurring along the same arc. To provide a more robust foundation for model evaluation, arcwise maxima have been estimated along with a quality indicator ranging from 0-3, which indicates how reliable each arcwise maximum is.

However, there exists a different version of the Kincaid data set by John Irving, which was distributed via his website now maintained by the Harmo organization, https://www.harmo.org/jsirwin (latest access March 12, 2024). The two data sets differ slightly due to different algorithms used for assigning sampling stations to arcs as well as to assessing the quality of measurements, see discussion https://www.harmo.org/jsirwin/KincaidHourlyDiscussion.html (latest access March 12, 2024). In this study, we use the version from John Irving, and both the entire set of SF6 measurements and the quality-controlled arcwise maximum values are used for the validation.

3.4 Experimental setup

For all three experiments, the simulations have been carried out using meteorological data from the limited-area NWP model Harmonie (Bengtsson et al., 2017). We use a horizontal grid resolution of approximately 2 km and a terrain-influenced hybrid vertical coordinate with 65 levels. The domains used for the simulations are shown in Figure 1. For initial conditions and spatial boundary conditions, we use the ERA5 reanalysis (Hersbach et al., 2020).

Both the current version of DERMA and the version described in Section 2 have then been run for all three experiments. For the Kincaid experiment, the new model was run with both of the plume rise algorithms described in Section 2.3. In all experiments, we use advection time steps of three minutes, and the sources have been discretized by releasing 50 puffs at every time step during the release period.

The resulting concentration fields have been interpolated in space using bilinear interpolation, and integrated in time to obtain a list of modelled average concentrations corresponding to the set of observations. Denoting the observations $\mathbf{x}$ and the predictions $\mathbf{y}$, we define the following statistical parameters used for model validation (cf. Draxler et al., 2001)

$$\text{rmse} = \sqrt{\frac{1}{N}\sum_i (y_i - x_i)^2},$$

$$\text{nmse} = \frac{1}{N\mu_{\mathbf{x}}\mu_{\mathbf{y}}}\sum_i (y_i - x_i)^2,$$

$$\text{r} = \frac{(\mathbf{x} - \mu_{\mathbf{x}})\cdot(\mathbf{y} - \mu_{\mathbf{y}})}{\sigma_{\mathbf{x}}\sigma_{\mathbf{y}}},$$

$$\text{b} = \frac{1}{N}\sum_i y_i - x_i,$$

$$\text{fb} = \frac{2b}{\mu_{\mathbf{x}} + \mu_{\mathbf{y}}}, \tag{34}$$

$$\text{fms} = 100\frac{N(y > 0) \cap N(x > 0)}{N(y > 0) \cup N(x > 0)},$$

$$\text{foex} = 100\left(\frac{N_{(y_i > x_i)}}{N} - \frac{1}{2}\right),$$

$$\text{fa}_2 = 100\left(\frac{N_{(1/2 < y_i/x_i < 2)}}{N}\right),$$

$$\text{fa}_5 = 100\left(\frac{N_{(1/5 < y_i/x_i < 5)}}{N}\right),$$

where μ and σ are the mean and standard deviation, rmse is the root mean square error, nmse is the normalized mean square error, r is the Pearson correlation coefficient, and b mean bias. Further, fb is the fractional bias, which is a normalized measure of the mean bias, fms is the figure of merit in space, which is defined as the percentage of overlap between the measured and predicted areas, foex is a measure of how many predictions are over-/underestimated, it is centered around zero and ranges from -50% to 50%. Finally, fa_α is the fraction of the predictions that are within a factor of $1/\alpha$ to α from the observation. For the calculation of foex and fa_α, the 0-0 pairs are excluded. Due to the infinite nature of Gaussian distributions, a puff model technically always has non-zero predictions everywhere. For that reason,

Figure 1. The three modelling domains used for the Harmonie simulations are indicated by the red squares in each plot. The upper plot shows the domain used for ETEX. The lower left plot shows the domain used for the Øresund experiment. The lower right plot shows the domain used for the Kincaid experiment. In all three plots, the red (and green in the case of the Øresund experiment) diamond shows the release location, and the black x's indicate the locations of sampling stations.

model predictions lower than the detection limit for each experiment are interpreted as non-detections.

3.5 Evaluation results

For all three experiments, the statistical parameters Eq. (34) have been calculated and are shown in the tables 1-3. In Figures 2-4, scatter plots of the model predictions as a function

of the observed values are shown, as well as quantile-quantile plots of predictions vs observations. For the Kincaid experiment, the model is further evaluated using the arcwise maximum values with quality indicator 3 (best quality), shown in Table 4 and Figure 5.

From Table 1, we see that the performances of the old and new models are quite similar for the ETEX experiment. The new model does show a slight improvement for the parame-
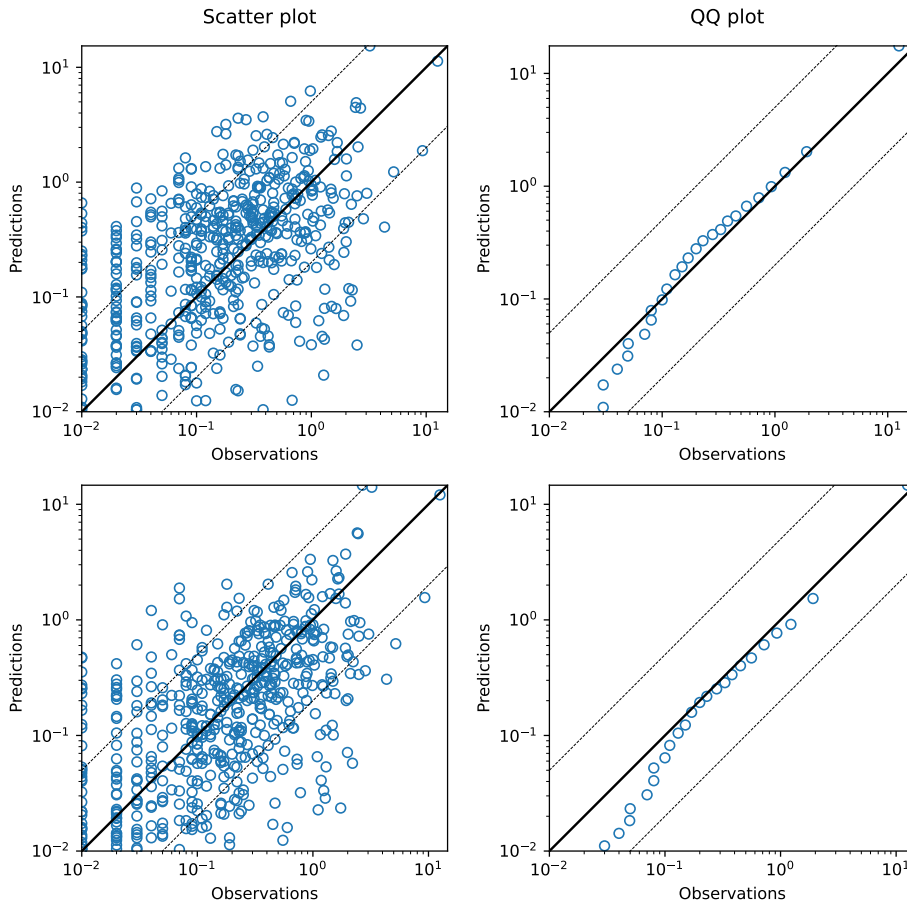
Figure 2. Results for the evaluation against ETEX. (left) scatter plot of model predictions as a function of observations, and (right) Quantile-quantile plot. Concentrations are in $[\mathrm{ng\,m^{-3}}]$. The upper figures are for the current version of DERMA, and the lower figures are for the new version.

Table 1. Statistical parameters Eq. (34) calculated for ETEX.

	mean	std	rmse	nmse	r	b	fb	fms	foex	$\mathrm{fa_2}$	$\mathrm{fa_5}$
Observations	0.10	0.44	0.00	0.00	1.00	0.000	0.00	100.0	0.0	100.0	100.0
Old	0.13	0.63	0.57	24.42	0.47	0.023	0.19	55.8	-4.0	20.8	40.5
New	0.10	0.60	0.53	26.78	0.52	-0.005	-0.05	55.8	-14.5	23.8	43.6

ters r, b and fb, $\mathrm{fa_2}$ and $\mathrm{fa_5}$. For the other parameters, the old model performs slightly better, but the differences are very small in general, which is expected because the long-range formulation of the new hybrid approach is similar to that of the current DERMA model, and there are few measurement stations close to the release point. From the scatter plots in Figure 2, it does look like the new model has slightly less spread for higher values, while the quantile-quantile plots are very similar.

The improved performance for long-range dispersion can likely be explained by the new random walk based on Eq. (3),

where the step size of the random walk depends on the local turbulence as well as the duration of the numerical time step. On the other hand, the current version of DERMA assigns a new random height to all puffs inside the PBL at every time step. For this reason, the new formulation should also generalize better for different durations of advection time step, whereas the physical behavior of the old formulation will change with the advection time step.

From Table 2, we see that the ground concentrations predicted by the old DERMA model are systematically underestimated for the Øresund experiment. This is in accor-
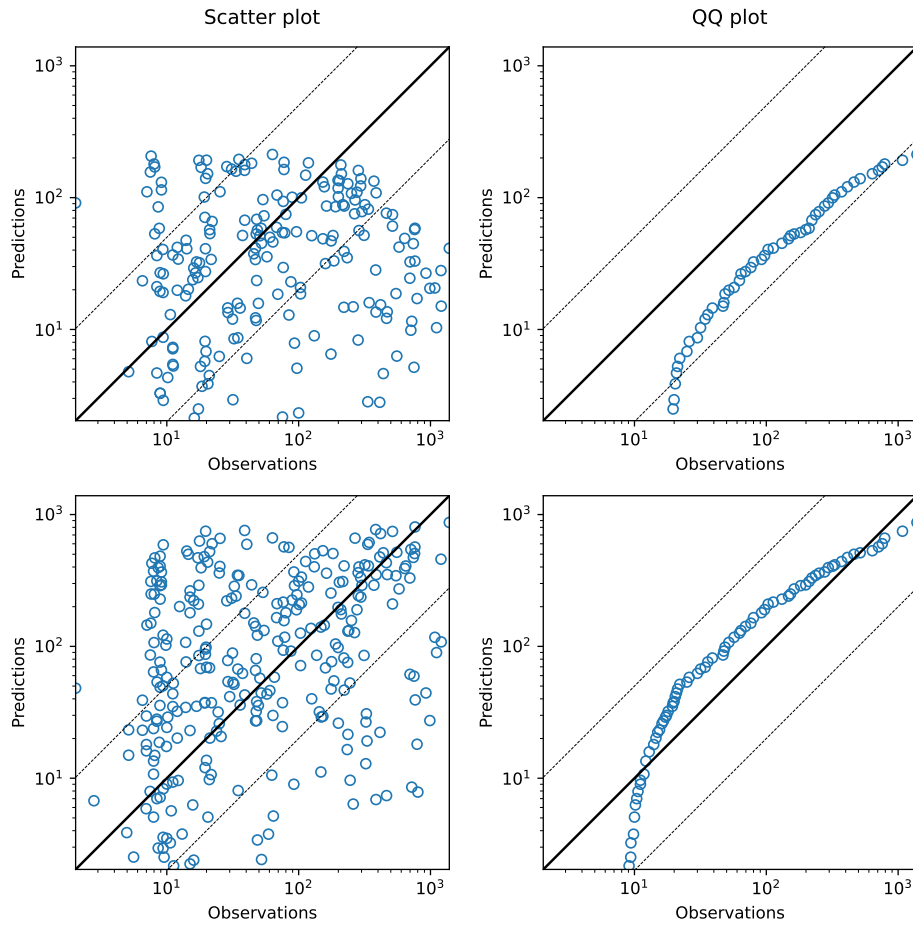
Figure 3. Results for the evaluation against the Øresund experiment. (left) scatter plot of model predictions as a function of observations, and (right) Quantile-quantile plot. Concentrations are in $[\mathrm{ng\,m^{-3}}]$. The upper figures are for the current version of DERMA, and the lower figures are for the new version.

Table 2. Statistical parameters Eq. (34) calculated for the Øresund experiment. When possible, longer time averages have been calculated to reduce the noise arising from the very short sampling periods, see Section 3.2 for further details.

	mean	std	rmse	nmse	r	b	fb	fms	foex	fa$_2$	fa$_5$
Observations	114.30	213.80	0.00	0.00	1.00	0.00	0.00	100.0	0.0	100.0	100.0
Old	29.31	48.53	231.09	15.94	0.09	-84.99	-1.18	51.5	-31.2	14.5	32.5
New	131.46	186.30	229.13	3.49	0.35	17.16	0.14	74.1	-6.4	24.9	47.7

dance with the expectations due to the instantaneous vertical mixing throughout the PBL, which will cause lower concentrations near the source. In reality, the gas was released quite close to the ground, and we would therefore expect the ground concentrations to be high near the source. Essentially, the new model performs better across all statistical parameters, and the same is indicated by Figure 3. Although none of the models correlate particularly well with the observations, the new model does predict high observed concentrations better, whereas the old model underestimates all the higher

concentrations. The quantile-quantile plot also indicates that the new model is better on average, although it overestimates lower values and underestimates the highest observations.

For the Kincaid experiment, we first consider the results based on the full measurement data set. Table 3 shows that the old model systematically overestimates the ground concentrations with a mean concentration of $360.44\ \mathrm{ng\,m^{-3}}$, whereas the mean of the observations is $53.87\ \mathrm{ng\,m^{-3}}$. This is again in accordance with the expectations; due to the plume rise, the effective release height is often quite high
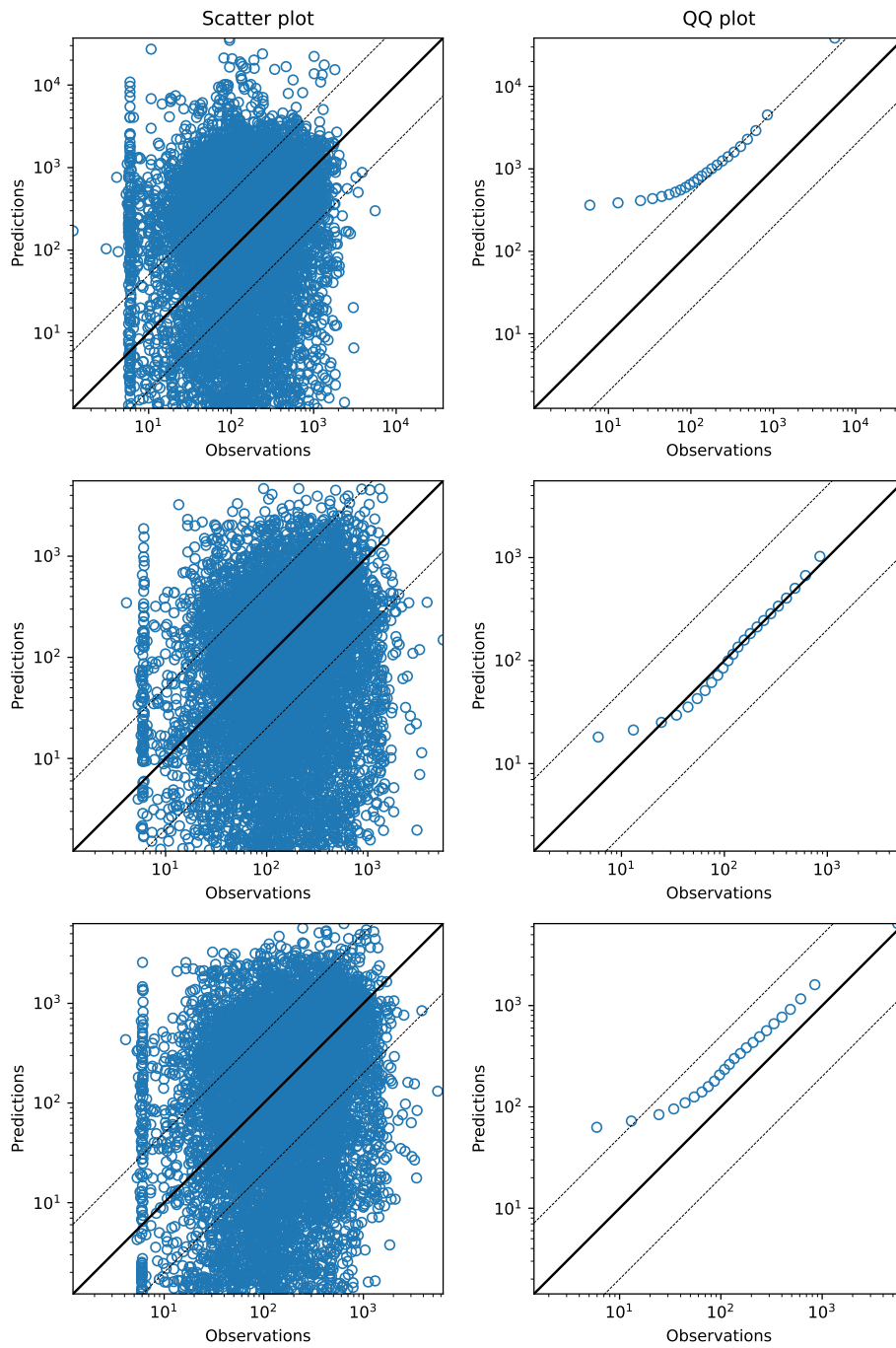
Figure 4. Results for the evaluation against the Kincaid experiment using all available measurements. (left) scatter plot of model predictions as a function of observations, and (right) Quantile-quantile plot. Concentrations are in $[\mathrm{ng\,m^{-3}}]$. The upper figures are for the current version of DERMA, the middle figures are for the new version using the Briggs plume rise formula, and the lower figures are for the new version using the Concawe formula.

above the surface, and therefore the ground concentrations should be low near the source, whereas the old model mixes the tracer down to the surface from the start. The new version also has a positive bias, but the magnitude depends strongly on the plume rise algorithm used. The results ob-

tained by using Briggs' formula give only a very small bias (average concentration of 60.29 $\mathrm{ng\,m^{-3}}$), while the results obtained by using the Concawe formula have an average of 112.05 $\mathrm{ng\,m^{-3}}$. The remaining statistics are quite similar for the two new models, and for rmse, nmse, r, b and fb the per-
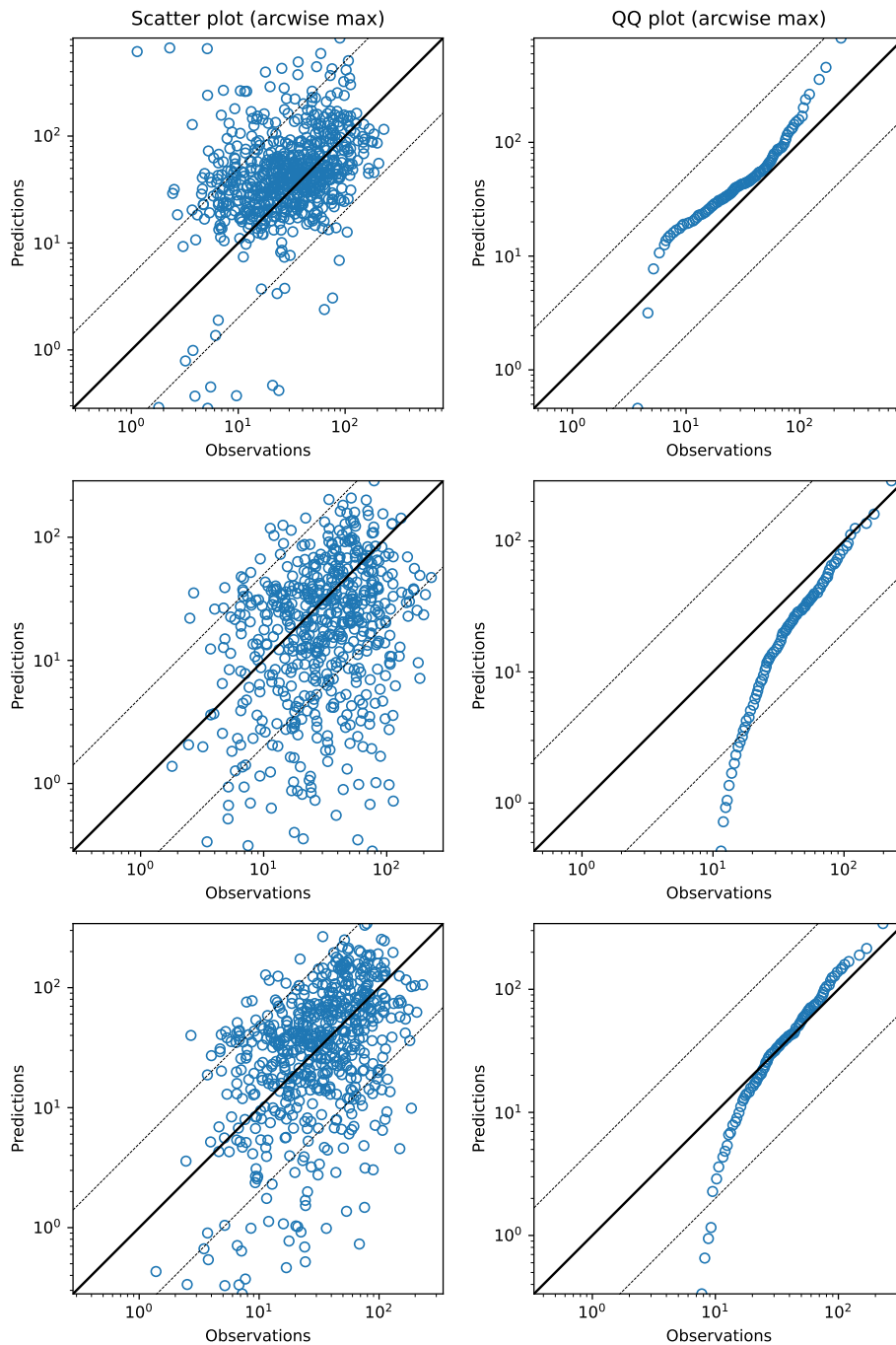
Figure 5. Results for the evaluation against the Kincaid experiment using arcwise maximum values with quality flag 3. (left) scatter plot of model predictions as a function of observations, and (right) Quantile-quantile plot. Further, concentrations have been divided by the mean release rate for the given release. The upper figures are for the current version of DERMA, the middle figures are for the new version using the Briggs plume rise formula, and the lower figures are for the new version using the Concawe formula.

formance is significantly better than for the old model, while for the remaining statistics, there seems to be only a small improvement. Figure 4 also shows that there is a very large spread in the scatter plots for all three models. However, the quantile-quantile plots do suggest a significantly better representation of the concentration field with the new model, especially when using the Briggs plume rise scheme.

It should be noted that this comparison method is very sensitive to even small errors in the meteorological model data; since the spatial and temporal resolution of the measurements

Table 3. Statistical parameters Eq. (34) calculated for the Kincaid experiment using all available measurements.

	mean	std	rmse	nmse	r	b	fb	fms	foex	fa_2	fa_5
Observations	53.87	171.12	0.00	0.00	1.00	0.00	0.00	100.0	0.0	100.0	100.0
Old	360.44	1160.86	1205.80	74.89	0.04	306.58	1.48	29.2	29.9	8.1	16.9
New (Briggs)	60.29	216.25	246.82	18.76	0.20	6.43	0.11	31.9	11.7	8.7	18.4
New (Concawe)	112.05	326.12	332.81	18.35	0.25	58.19	0.70	32.9	21.0	9.4	19.5

Table 4. Statistical parameters Eq. (34) calculated for the Kincaid experiment using the arcwise maximum values with quality flag 3.

	mean	std	rmse	nmse	r	b	fb	foex	fa_2	fa_5
Observations	41.03	35.03	0.00	0.00	1.00	0.00	0.000	0.0	100.0	100.0
Old	66.30	84.99	89.06	2.92	0.19	25.27	0.471	13.5	53.3	85.1
New (Briggs)	27.37	35.41	47.16	1.98	0.18	-13.66	-0.399	-19.1	32.3	63.2
New (Concawe)	46.48	50.37	49.74	1.30	0.37	5.45	0.124	-1.3	43.6	76.6

is so high, an error in e.g. the wind direction may result in large errors. Therefore, the comparison with the arcwise maximum values might be a more robust way of evaluating the model. As described in Section 3.3, the observations from the Kincaid experiment were assigned to arcs with the same approximate distance to the source. There are up to 12 arcs at distances 0.5 km, 1 km, 2 km, 3 km, 5 km, 7 km, 10 km, 15 km, 20 km, 30 km, 40 km and 50 km (not all arcs exist for all release periods). For every one-hour sampling period, the maximum value in each arc has been determined and, by comparison with neighboring values, a quality indicator from 0 to 3 has been assigned. The predicted maximum concentration of an arc was estimated by first interpolating the concentration field to all sampling locations of that arc, and then calculating the maximum value. When comparing the model predictions to observations, only values with quality flag 3 are used.

From Table 4, the results are slightly more ambiguous than from the previous comparisons. The new model using Briggs' formula performs slightly better than the old model for the parameters nmse, b and fb, while the old model performs slightly better for foex, fa_2 and fa_5. However, the new model using the Concawe formula seems to stand out with better performance on all parameters except for fa_2 and fa_5, where the old model performs slightly better. Generally, all models perform much better on the arcwise maxima than when using the entire dataset, which confirms that this approach is less sensitive to, e.g., errors in the predicted wind direction. From Figure 5, we also see that all three scatter plots have a much smaller spread than in Figure 4.

There is quite a large difference in performance between the two new versions, which are identical except for the plume rise scheme used. This clearly indicates the impor-

tance of estimating the start height correctly in order to predict reliable ground concentrations near the source.

The Kincaid experiment has been used for evaluation by many different dispersion models. Thus, we can also compare the performance of DERMA to other models. However, most evaluations use the MVK version of the arcwise maxima, which means that direct comparison of the statistical parameters is perhaps not meaningful, but it can give an indication of the expected range of the parameters. We can see that DERMA performs similarly to other models as, see e.g. Bellasio et al. (2018, Table 4), which lists the performance of nine different dispersion models evaluated against the Kincaid experiment.

4 Summary and conclusions

This paper describes a new hybrid particle-puff formulation for dispersion modelling, making use of simple assumptions to separate turbulence into a stochastic particle part and a puff part, without the theoretical risk of double counting turbulent effects. This formulation allows for the use of a limited number of puffs and longer advection time steps compared to stochastic particle models. Further, compared to the classical puff approach, it allows for a more realistic description of turbulent diffusion for small puffs. For large puffs, on the other hand, the formulation allows puffs to be exposed to the vertical wind shear in the PBL without the need for puff splitting.

In addition, new parameterizations have been implemented in DERMA for turbulent wind fluctuation and Lagrangian time scales, for PBL height, and for plume rise. For the latter, both the Concawe formula and the Briggs formula have been implemented.

The model evaluation shows that implementation of the new hybrid approach improves the performance of DERMA for all three considered experiments. The evaluation method is not very robust, since the model predictions are very sensitive to meteorological errors. However, since our evaluation uses a large amount of measurement data sampled over many days during different times of the year, the overall trends in the results should give a good indication of the models' performances. Further, the use of the arcwise maxima from the Kincaid experiment provides a completely different way of comparing model predictions with observations, which again indicates improved performance when using the new hybrid formulation.

Further, a comparison of the two plume rise algorithms indicates how important it is to correctly estimate the initial plume height in order to predict the dispersion near the source. Unfortunately, there is no clear answer to which plume rise algorithm is best; in our evaluation, the Briggs formulas seem to give slightly better results when calculating statistics based on all data, while the Concawe formula performs better when compared to the arcwise maxima. However, the Concawe formula is somewhat more generally applicable, because it only needs the released heat, whereas the Briggs formulas are specifically developed for gas being exhausted from a stack and both gas temperature and exhaust velocity are necessary inputs.

In conclusion, the developed hybrid particle-puff formulation, in combination with the additional new implementations, has improved the performance of DERMA, especially for short-range dispersion modelling. Thus, the implementation of these improvements in the operational version of DERMA could pave the way for new applications of the model in the future.

References

Andronopoulos, S., Davakis, E., and Bartzis, J. G.: RODOS-DIPCOT model description and evaluation, Report RODOS (RA2)-TN (09), 1, 2009.

Baklanov, A. and Sørensen, J. H.: Parameterisation of radionuclide deposition in atmospheric dispersion models, Phys. Chem. Earth, 26, 787–799, 2001.

Bellasio, R., Bianconi, R., Mosca, S., and Zannetti, P.: Incorporation of numerical plume rise algorithms in the Lagrangian particle model LAPMOD and validation against the Indianapolis and Kincaid datasets, Atmosphere, 9, 404, 2018.

Bengtsson, L., Andrae, U., Aspelien, T., Batrak, Y., Calvo, J., de Rooy, W., Gleeson, E., Hansen-Sass, B., Homleid, M., Hortal, M., Ivarsson, K.-I., Lenderink, G., Niemelä, S., Nielsen, K. P., Onvlee, J., Rontu, L., Samuelsson, P., Muñoz, D. S., Subias, A., Tijm, S., Toll, V., Yang, X., and Ødegaard Køltzow, M.: The HARMONIE–AROME Model Configuration in the ALADIN–HIRLAM NWP System, Monthly Weather Review, 145, 1919–1935, https://doi.org/10.1175/MWR-D-16-0417.1, 2017.

Bowne, N. and Londergan, R.: Overview, results, and conclusions for the EPRI Plume-Model Validation and Development Project: plains site. Final report, Tech. rep., TRC Environmental Consultants, Inc., East Hartford, CT (USA), 1983.

Briggs, G. A.: A plume rise model compared with observations, Journal of the Air Pollution Control Association, 15, 433–438, 1965.

Bromiley, P.: Products and convolutions of Gaussian probability density functions, Tina-Vision Memo, 3, 1, 2003.

Brummage, K.: The calculation of atmospheric dispersion from a stack, Atmospheric Environment (1967), 2, 197–224, 1968.

De Haan, P. and Rotach, M. W.: A novel approach to atmospheric dispersion modelling: The Puff-Particle Model, Quarterly Journal of the Royal Meteorological Society, 124, 2771–2792, 1998.

Draxler, R. R. and Hess, G.: Description of the HYSPLIT4 modeling system, 1997.

Draxler, R. R., Heffter, J. L., and Rolph, G. D.: Data archive of tracer experiments and meteorology, Tech. rep., Citeseer, 2001.

Einstein, A.: Investigations on the Theory of the Brownian Movement, Courier Corporation, 1956.

Gifford, F.: The random force theory: Application to meso-and large-scale atmospheric diffusion, Boundary-Layer Meteorology, 30, 159–175, 1984.

Gloster, J., Jones, A., Redington, A., Burgin, L., Sørensen, J. H., Turner, R., Hullinger, P., Dillon, M., Astrup, P., Garner, G., D'Amours, R., Sellers, R., and Paton, D.: Airborne spread of foot-and-mouth disease – model intercomparison, Veterinary Journal, 183, 278–286, 2010.

Graziani, G., Klug, W., and Mosca, S.: Real-time long-range dispersion model evaluation of the ETEX first release, Office for Official Publications of the European communities, 1998.

Hanna, S.: Applications in air pollution modeling, in: Atmospheric Turbulence and Air Pollution Modelling: A Course held in The Hague, 21–25 September, 1981, pp. 275–310, Springer, 1984.

Hanna, S. R. and Paine, R. J.: Hybrid plume dispersion model (HPDM) development and evaluation, Journal of Applied Meteorology and Climatology, 28, 206–224, 1989.

Hersbach, H., Bell, B., Berrisford, P., Hirahara, S., Horányi, A., Muñoz-Sabater, J., Nicolas, J., Peubey, C., Radu, R., Schepers, D., et al.: The ERA5 global reanalysis, Quarterly Journal of the Royal Meteorological Society, 146, 1999–2049, 2020.

Hoe, S., Müller, H., Gering, F., Thykier-Nielsen, S., and Sørensen, J. H.: ARGOS 2001 a decision support system for nuclear emergencies, In: Proceedings of the Radiation Protection and Shielding Division Topical Meeting. April 14–17. Santa Fe, New Mexico, USA, 2002.

Jones, A., Thomson, D., Hort, M., and Devenish, B.: The UK Met Office's next-generation atmospheric dispersion model, NAME III, in: Air Pollution Modeling and its Application XVII, Pro-

ceedings of the 27th NATO/CCMS International Technical Meeting on Air Pollution Modelling and its Application, pp. 24–29, 2004.

Kolmogorov, A. N.: The local structure of turbulence in incompressible viscous fluid for very large Reynolds, Numbers. In Dokl. Akad. Nauk SSSR, 30, 301, 1941.

Korsakissok, I. and Mallet, V.: Comparative study of Gaussian dispersion formulas within the Polyphemus platform: evaluation with Prairie Grass and Kincaid experiments, Journal of applied meteorology and climatology, 48, 2459–2473, 2009.

Mikkelsen, T., Alexandersen, S., Astrup, P., Champion, H. J., Donaldson, A. I., Dunkerley, F. N., Gloster, J., Sørensen, J. H., and Thykier-Nielsen, S.: Investigation of airborne foot-and-mouth disease virus transmission during low-wind conditions in the early phase of the UK 2001 epidemic, Atmos. Chem. Phys, 3, 2101–2110, 2003.

Mortensen, N. G. and Gryning, S.-E.: The Øresund Experiment Data Bank Report, Department of Meteorology and Wind Energy, Risø National Laboratory, 1989.

Nodop, K., Connolly, R., and Girardi, F.: The field campaigns of the European Tracer Experiment (ETEX): Overview and results, Atmospheric Environment, 32, 4095–4108, 1998.

Olesen, H.: User´s guide to the Model Validation Kit, Research Notes from NERI, National Environmental Research Institute, 2005.

Pisso, I., Sollum, E., Grythe, H., Kristiansen, N. I., Cassiani, M., Eckhardt, S., Arnold, D., Morton, D., Thompson, R. L., Groot Zwaaftink, C. D., et al.: The Lagrangian particle dispersion model FLEXPART version 10.4, Geoscientific Model Development, 12, 4955–4997, 2019.

Scire, J. S., Strimaitis, D. G., Yamartino, R. J., et al.: A user's guide for the CALPUFF dispersion model, Earth Tech, Inc, 521, 1–521, 2000.

Sørensen, J. H.: Sensitivity of the DERMA long-range Gaussian dispersion model to meteorological input and diffusion parameters, Atmospheric Environment, 32, 4195–4206, 1998.

Sørensen, J. H.: Method for source localization proposed and applied to the October 2017 case of atmospheric dispersion of Ru-106, Journal of environmental radioactivity, 189, 221–226, 2018.

Sørensen, J. H., Mackay, D. K. J., Jensen, C. Ø., and Donaldson, A. I.: An integrated model to predict the atmospheric spread of foot-and-mouth disease virus, Epidemiol. Infect., 124, 577–590, 2000.

Sørensen, J. H., Jensen, C. Ø., Mikkelsen, T., Mackay, D., and Donaldson, A. I.: Modelling the atmospheric spread of foot-and-mouth disease virus for emergency preparedness, Phys. Chem. Earth, 26, 93–97, 2001.

Sørensen, J. H., Baklanov, A., and Hoe, S.: The Danish emergency response model of the atmosphere (DERMA), Journal of environmental radioactivity, 96, 122–129, 2007.

Stohl, A., Forster, C., Frank, A., Seibert, P., and Wotawa, G.: The Lagrangian particle dispersion model FLEXPART version 6.2, Atmospheric Chemistry and Physics, 5, 2461–2474, 2005.

Thykier-Nielsen, S., Deme, S., and Mikkelsen, T.: Description of the atmospheric dispersion module RIMPUFF, Riso National Laboratory, PO Box, 49, 1999.

Tølløse, K. S. and Sørensen, J. H.: Bayesian Inverse Modelling for Probabilistic Multi-Nuclide Source Term Estimation Using Observations of Air Concentration and Gamma Dose Rate, Atmosphere, 13, 1877, 2022.

Tølløse, K. S., Kaas, E., and Sørensen, J. H.: Probabilistic Inverse Method for Source Localization Applied to ETEX and the 2017 Case of Ru-106 including Analyses of Sensitivity to Measurement Data, Atmosphere, 12, https://doi.org/10.3390/atmos12121567, 2021.

Vogelezang, D. and Holtslag, A.: Evaluation and model impacts of alternative boundary-layer height formulations, Boundary-Layer Meteorology, 81, 245–269, 1996.

Zannetti, P.: Air pollution modeling: theories, computational methods and available software, Springer Science & Business Media, 2013.

4.1. PAPER 3: A NEW HYBRID PARTICLE-PUFF APPROACH TO ATMOSPHERIC DISPERSION MODELLING, IMPLEMENTED IN THE DANISH EMERGENCY RE-SPONSE MODEL OF THE ATMOSPHERE (DERMA)

Chapter 5

Discussion and Conclusions

The discussion presented here focuses on the findings in the context of the overall objectives of the PhD project, while detailed discussions of the different results are included in the previous chapters. First, Chapter 5.1 presents the conclusions of the first two articles and evaluates their readiness for potential operationalization. Next, Chapter 5.2 summarizes the conclusions of the third manuscript and discusses how the findings have shifted the perspectives for DERMA as a short-range dispersion model. Finally, Chapter 5.3 explores perspectives for future research.

5.1 Towards operational use of inverse methods for source term estimation

5.1.1 Source localization

In the first article, presented in Chapter 3.1, it is demonstrated that the developed methodology can efficiently predict a two-dimensional probability distribution for the release location given essentially no prior knowledge and only making the following assumptions:

1. the release comes from a stationary point source with a constant release rate,

2. the source is located at some height inside the PBL,

3. the source is located inside the selected model domain and the release happens during the selected simulation period.

The first two requirements of course put restrictions on the type of scenarios, we can consider with this method, but the latter is not very restrictive, since the model domain and simulation period can always be extended.

The sensitivity analyses show that the method provides consistent results both when observations are not available near the release location, and when the effective sampling frequency of the measurements is reduced to both 12 and 24 hours. Both of these changes made to the observation data reduce the precision of resulting posterior probability distribution, i.e. the high density regions cover larger geographical areas. However, the release location is consistently predicted inside the area of the highest probability density. Hence, in combination with a list of potential release locations in the area, the method can be used to point out the most likely candidates.

Applying the method to the Ru-106 case predicts an area of high probability density covering a relatively large area in Russia, south of the Ural mountains. Combining this result with the locations of nuclear facilities in the area, we conclude that the Mayak nuclear facility is the most likely release location.

In both of the cases considered, many observations sampled from a large geographical area were available. Thus, additional sensitivity analyses could be performed to determine the threshold at which the methodology becomes ineffective, specifically identifying the minimum amount of data required to ensure meaningful results. Aside from that, the methodology could in principle be made ready for operationalization without much extra work, if a standardized input format providing the relevant measurement information is defined.

5.1.2 Source term estimation during nuclear accident

In the second article, presented in Chapter 3.2, the developed method is demonstrated in an idealized case where model errors are negligible. While this study shows promising results, the supplementary results presented in Chapter 3.3 indicate the methodology does not have a robust performance when applied to more realistic scenarios. Thus, although the first important steps are made in the development of this method, more work is needed.

In theory, the problem of source term estimation for a known location should be much simpler to solve than localizing a source, where neither the location nor the source strength is known. To understand why this second problem seems to cause more challenges, there are a number of differences between the two studies that are worth pointing out.

In the source localization method, various simplifications and assumptions are made about the source term. These, when combined with the adjoint modelling approach, enable a highly efficient assessment of the likelihood of a proposed source term model. Further, the correlation-based likelihood, allows the probability of a proposed source location to be decoupled from the source strength. Consequently, the probability can quickly be evaluated for all grid points in the model domain without the need for a Monte Carlo method to sample the distribution.

On the other hand, when the source location is known, minimal assumptions are made about the source, permitting release rates to evolve over time. Further, the artificial Loviisa power plant release consisted of 11 dose-contributing radioactive nuclides, of which 4 are gasses, which are not captured by filter stations but instead only measured through their contribution to the nuclide-independent gamma dose rates. Finally, we observed a large discrepancy between the gamma dose rate patterns from the two modelling systems, DERMA+ARGOS and SILAM, rendering the gamma dose rates ineffective for source term estimation in this case. Considering these deficiencies, it is not surprising that the inverse problem may be ill-conditioned, i.e. the data are not sufficient to constrain the parameters describing the source term.

5.2 DERMA as a short-range dispersion model

In the manuscript for the third article, presented in Chapter 4.1, a new description of turbulent diffusion is provided. This new approach is a hybrid between a classical puff model and a stochastic particle model. The hybrid formulation gives a more realistic

description for small puffs by allowing advection by larger eddies. For large puffs, the stochastic displacement instead provides a way of exposing puffs to vertical wind shear without the need for puff splitting. In addition, the method is formulated such that the turbulent diffusion is not double-counted.

The simplified turbulence description in the currently operational version of DERMA poses one of the primary challenges in improving the model to enable short-range modelling. Thus, the work presented in this article is an important first step towards an operational short-range version of DERMA. Additionally, the implementation of the Briggs and Concawe plume rise algorithms greatly improves the realism of simulations near the release location in cases with heat release.

The model evaluation carried out as part of the project shows that the new turbulence description improves the performance of DERMA across all spatial scales, however, especially for short-range dispersion.

5.3   Future perspectives

One important future perspective is of course the potential operationalization of the developed methods. However, regardless of whether the methods can and will be operationalized in the future, there are of course still open research questions.

Most importantly, further research is required on methods for estimating source terms in the event of nuclear power plant accidents. Specifically concerning this project, a crucial aspect is understanding the large discrepancy between the gamma dose rates from the two model systems considered. Initially, it would be logical to employ the newly developed short-range version of DERMA to address the issue and achieve a more accurate dispersion pattern near the source. Next, it would be advisable to conduct comparisons between newly generated sets of gamma dose rates produced by the DERMA+ARGOS system utilizing various meteorological forecast data, e.g. data from several different members of a meteorological ensemble prediction system. Ideally, this should be applied to different cases regarding meteorological scenarios as well as release scenarios.

Further, it might be worth considering reformulating the problem slightly. The study aimed to provide a source term estimate given no other information than an estimated amount of each nuclide in the core inventory. However, permitting the release rate of each nuclide to vary independently within each time interval will introduce numerous degrees of freedom to the source term. Consequently, a substantial amount of data may be necessary to effectively constrain the parameters of the source term. Therefore, it may be beneficial to consider imposing additional constraints on the prior distribution of the source term. For example, using discrete source term ensembles for the prior distributions could greatly reduce the dimensionality of the problem.

Despite the discussions above, it is important to highlight the overall success achieved by employing a probabilistic inversion method to the source term estimation problem. We showed that when the inverse problem was not ill-conditioned, the method efficiently sampled the posterior probability distribution for the multi-nuclide source term. Moreover, this was accomplished without the need for parameter tuning, thanks to the NUTS algorithm.

Next, the developed source localization method showed promising results, and it is likely that the approach can be successfully applied in case of a new incident similar to the Ru-106 case. However, other categories of incidents might also occur, where the

measured particles/gasses are not captured by as large a sampling network as in the Ru-106 case. Thus, additional sensitivity studies should be carried out to test the limits of the method. Furthermore, our analysis exclusively incorporated air concentration measurements, while ground deposition measurements were also available. Hence, future research could explore the utilization of these measurements, thereby increasing the total amount of data available.

Finally, the new short-range version of DERMA is in principle ready to be put into use, as the advancements are directly integrated into the DERMA code. Nonetheless, the initial step will naturally involve running the new version in parallel with the currently operational model and monitoring the differences in model predictions across various scenarios. Moreover, as previously discussed, the model evaluation approach is highly susceptible to errors in the meteorological forecast data. One potential solution to address this issue could involve utilizing a meteorological ensemble prediction system to generate a probabilistic dispersion forecast. However, assessing probabilistic forecasts poses additional challenges, and novel evaluation techniques may need to be developed.

Bibliography

(2020). *IFS Documentation CY47R1 - Part III: Dynamics and Numerical Procedures.* IFS Documentation. ECMWF.

Andersson, E., Haseler, J., Undén, P., Courtier, P., Kelly, G., Vasiljevic, D., Brankovic, C., Gaffard, C., Hollingsworth, A., Jakob, C., Janssen, P., Klinker, E., Lanzinger, A., Miller, M., Rabier, F., Simmons, A., Strauss, B., Viterbo, P., Cardinali, C., and Thépaut, J.-N. (1998). The ecmwf implementation of three-dimensional variational assimilation (3d-var). iii: Experimental results. *Quarterly Journal of the Royal Meteorological Society*, 124(550):1831–1860.

Andronopoulos, S., Davakis, E., and Bartzis, J. G. (2009). Rodos-dipcot model description and evaluation. *Report RODOS (RA2)-TN (09)*, 1.

Baklanov, A. and Sørensen, J. H. (2001). Parameterisation of radionuclide deposition in atmospheric dispersion models. *Phys. Chem. Earth*, 26:787–799.

Beckett, F. M., Witham, C. S., Leadbetter, S. J., Crocker, R., Webster, H. N., Hort, M. C., Jones, A. R., Devenish, B. J., and Thomson, D. J. (2020). Atmospheric dispersion modelling at the london vaac: A review of developments since the 2010 eyjafjallajökull volcano ash cloud. *Atmosphere*, 11(4).

Bellasio, R., Bianconi, R., Mosca, S., and Zannetti, P. (2018). Incorporation of numerical plume rise algorithms in the lagrangian particle model lapmod and validation against the indianapolis and kincaid datasets. *Atmosphere*, 9(10):404.

Bengtsson, L., Andrae, U., Aspelien, T., Batrak, Y., Calvo, J., de Rooy, W., Gleeson, E., Hansen-Sass, B., Homleid, M., Hortal, M., Ivarsson, K.-I., Lenderink, G., Niemelä, S., Nielsen, K. P., Onvlee, J., Rontu, L., Samuelsson, P., Muñoz, D. S., Subias, A., Tijm, S., Toll, V., Yang, X., and Ødegaard Køltzow, M. (2017). The harmonie–arome model configuration in the aladin–hirlam nwp system. *Monthly Weather Review*, 145(5):1919–1935.

Betancourt, M. (2017). A conceptual introduction to hamiltonian monte carlo. *arXiv preprint arXiv:1701.02434*.

Bowne, N. and Londergan, R. (1983). Overview, results, and conclusions for the epri plume-model validation and development project: plains site. final report. Technical report, TRC Environmental Consultants, Inc., East Hartford, CT (USA).

Briggs, G. A. (1965). A plume rise model compared with observations. *Journal of the Air Pollution Control Association*, 15(9):433–438.

Bromiley, P. (2003). Products and convolutions of gaussian probability density functions. *Tina-Vision Memo*, 3(4):1.

Brummage, K. (1968). The calculation of atmospheric dispersion from a stack. *Atmospheric Environment (1967)*, 2(3):197–224.

Casella, G. and George, E. I. (1992). Explaining the gibbs sampler. *The American Statistician*, 46(3):167–174.

Chock, D. P. and Winkler, S. L. (1994). A particle grid air quality modeling approach: 1. the dispersion aspect. *Journal of Geophysical Research: Atmospheres*, 99(D1):1019–1031.

Courtier, P., Thépaut, J.-N., and Hollingsworth, A. (1994). A strategy for operational implementation of 4d-var, using an incremental approach. *Quarterly Journal of the Royal Meteorological Society*, 120(519):1367–1387.

Davoine, X. and Bocquet, M. (2007). Inverse modelling-based reconstruction of the chernobyl source term available for long-range transport. *Atmospheric Chemistry and Physics*, 7(6):1549–1564.

De Haan, P. and Rotach, M. W. (1998). A novel approach to atmospheric dispersion modelling: The puff-particle model. *Quarterly Journal of the Royal Meteorological Society*, 124(552):2771–2792.

Draxler, R. R., Heffter, J. L., and Rolph, G. D. (2001). Data archive of tracer experiments and meteorology. Technical report, Citeseer.

Draxler, R. R. and Hess, G. (1997). Description of the hysplit4 modeling system.

Efthimiou, G. C., Kovalets, I. V., Venetsanos, A., Andronopoulos, S., Argyropoulos, C. D., and Kakosimos, K. (2017). An optimized inverse modelling method for determining the location and strength of a point source releasing airborne material in urban environment. *Atmospheric environment*, 170:118–129.

Enting, I. G. (2002). *Inverse problems in atmospheric constituent transport*. Cambridge University Press.

Gelman, A. and Rubin, D. B. (1992). Inference from iterative simulation using multiple sequences. *Statistical science*, pages 457–472.

Gifford, F. (1984). The random force theory: Application to meso-and large-scale atmospheric diffusion. *Boundary-Layer Meteorology*, 30(1):159–175.

Gloster, J., Jones, A., Redington, A., Burgin, L., Sørensen, J. H., Turner, R., Hullinger, P., Dillon, M., Astrup, P., Garner, G., D'Amours, R., Sellers, R., and Paton, D. (2010). Airborne spread of foot-and-mouth disease – model intercomparison. *Veterinary Journal*, 183:278–286.

Graziani, G., Klug, W., and Mosca, S. (1998). *Real-time long-range dispersion model evaluation of the ETEX first release*. Office for Official Publications of the European communities.

Gudmundsson, M. T., Pedersen, R., Vogfjörd, K., Thorbjarnardóttir, B., Jakobsdóttir, S., and Roberts, M. J. (2010). Eruptions of eyjafjallajökull volcano, iceland.

Hanna, S. (1984). Applications in air pollution modeling. In *Atmospheric Turbulence and Air Pollution Modelling: A Course held in The Hague, 21–25 September, 1981*, pages 275–310. Springer.

Hanna, S. R. and Paine, R. J. (1989). Hybrid plume dispersion model (hpdm) development and evaluation. *Journal of Applied Meteorology and Climatology*, 28(3):206–224.

Hastings, W. K. (1970). Monte carlo sampling methods using markov chains and their applications.

Hersbach, H., Bell, B., Berrisford, P., Hirahara, S., Horányi, A., Muñoz-Sabater, J., Nicolas, J., Peubey, C., Radu, R., Schepers, D., et al. (2020). The era5 global reanalysis. *Quarterly Journal of the Royal Meteorological Society*, 146(730):1999–2049.

Hoe, S., , Sørensen, J. H., and Thykier-Nielsen, S. (1999). The nuclear decision support system argos nt and early warning systems in some countries around the baltic sea. *In: Proceedings of the 7th Topical Meeting on Emergency Preparedness and Response. September 14–17, Santa Fe, New Mexico, USA*.

Hoe, S., Müller, H., Gering, F., Thykier-Nielsen, S., and Sørensen, J. H. (2002). Argos 2001 a decision support system for nuclear emergencies. *In: Proceedings of the Radiation Protection and Shielding Division Topical Meeting. April 14–17. Santa Fe, New Mexico, USA*.

Hoffman, M. D., Gelman, A., et al. (2014). The no-u-turn sampler: adaptively setting path lengths in hamiltonian monte carlo. *J. Mach. Learn. Res.*, 15(1):1593–1623.

Högström, U. (1988). Non-dimensional wind and temperature profiles in the atmospheric surface layer: A re-evaluation. *Topics in micrometeorology. A Festschrift for arch dyer*, pages 55–78.

Hyndman, R. J. (1996). Computing and graphing highest density regions. *The American Statistician*, 50(2):120–126.

Jones, A., Thomson, D., Hort, M., and Devenish, B. (2004). The uk met office's next-generation atmospheric dispersion model, name iii. In *Air Pollution Modeling and its Application XVII, Proceedings of the 27th NATO/CCMS International Technical Meeting on Air Pollution Modelling and its Application*, pages 24–29.

Keats, A., Yee, E., and Lien, F.-S. (2007). Bayesian inference for source determination with applications to a complex urban environment. *Atmospheric environment*, 41(3):465–479.

Kolmogorov, A. N. (1941). The local structure of turbulence in incompressible viscous fluid for very large reynolds. *Numbers. In Dokl. Akad. Nauk SSSR*, 30:301.

Koo, Y.-H., Yang, Y.-S., and Song, K.-W. (2014). Radioactivity release from the fukushima accident and its consequences: A review. *Progress in Nuclear Energy*, 74:61–70.

Korsakissok, I. and Mallet, V. (2009). Comparative study of gaussian dispersion formulas within the polyphemus platform: evaluation with prairie grass and kincaid experiments. *Journal of applied meteorology and climatology*, 48(12):2459–2473.

Kovalets, I. V., Efthimiou, G. C., Andronopoulos, S., Venetsanos, A. G., Argyropoulos, C. D., and Kakosimos, K. E. (2018). Inverse identification of unknown finite-duration air pollutant release from a point source in urban environment. *Atmospheric Environment*, 181:82–96.

Kovalets, I. V., Romanenko, O., and Synkevych, R. (2020). Adaptation of the rodos system for analysis of possible sources of ru-106 detected in 2017. *Journal of environmental radioactivity*, 220:106302.

Le Brazidec, J. D., Bocquet, M., Saunier, O., and Roustan, Y. (2020). Mcmc methods applied to the reconstruction of the autumn 2017 ruthenium-106 atmospheric contamination source. *Atmospheric Environment: X*, 6:100071.

Liu, Y., Haussaire, J.-M., Bocquet, M., Roustan, Y., Saunier, O., and Mathieu, A. (2017). Uncertainty quantification of pollutant source retrieval: comparison of bayesian methods with application to the chernobyl and fukushima daiichi accidental releases of radionuclides. *Quarterly Journal of the Royal Meteorological Society*, 143(708):2886–2901.

Marchuk, G., Shutyaev, V., and Bocharov, G. (2005). Adjoint equations and analysis of complex systems: Application to virus infection modelling. *Journal of computational and applied mathematics*, 184(1):177–204.

Masson, O., Steinhauser, G., Zok, D., Saunier, O., Angelov, H., Babić, D., Bečková, V., Bieringer, J., Bruggeman, M., Burbidge, C., et al. (2019). Airborne concentrations and chemical considerations of radioactive ruthenium from an undeclared major nuclear release in 2017. *Proceedings of the National Academy of Sciences*, 116(34):16750–16759.

Mikkelsen, T., Alexandersen, S., Astrup, P., Champion, H. J., Donaldson, A. I., Dunkerley, F. N., Gloster, J., Sørensen, J. H., and Thykier-Nielsen, S. (2003). Investigation of airborne foot-and-mouth disease virus transmission during low-wind conditions in the early phase of the uk 2001 epidemic. *Atmos. Chem. Phys*, 3:2101–2110.

Monin, A. and Obukhov, A. (1954). Osnovnye zakonomernosti turbulentnogo peremeshivanija v prizemnom sloe atmosfery (basic laws of turbulent mixing in the atmosphere near the ground). *Trudy geofiz. inst. AN SSSR*, 24(151):163–187.

Mortensen, N. G. and Gryning, S.-E. (1989). *The Øresund Experiment Data Bank Report*. Department of Meteorology and Wind Energy, Risø National Laboratory.

Nodop, K., Connolly, R., and Girardi, F. (1998). The field campaigns of the european tracer experiment (etex): Overview and results. *Atmospheric Environment*, 32(24):4095–4108.

Olesen, H. (2005). *User´s guide to the Model Validation Kit*. Research Notes from NERI. National Environmental Research Institute.

Pisso, I., Sollum, E., Grythe, H., Kristiansen, N. I., Cassiani, M., Eckhardt, S., Arnold, D., Morton, D., Thompson, R. L., Groot Zwaaftink, C. D., et al. (2019). The lagrangian particle dispersion model flexpart version 10.4. *Geoscientific Model Development*, 12(12):4955–4997.

Pudykiewicz, J. A. (1998). Application of adjoint tracer transport equations for evaluating source parameters. *Atmospheric environment*, 32(17):3039–3050.

Robertson, L., Langner, J., and Engardt, M. (1999). An eulerian limited-area atmospheric transport model. *Journal of Applied Meteorology and Climatology*, 38(2):190–210.

Saenko, V., Ivanov, V., Tsyb, A., Bogdanova, T., Tronko, M., Demidchik, Y., and Yamashita, S. (2011). The chernobyl accident and its consequences. *Clinical Oncology*, 23(4):234–243. The Radiobiological Consequences of the Chernobyl Accident 25 Years On - April 2011.

Salvatier, J., Wiecki, T. V., and Fonnesbeck, C. (2016). Probabilistic programming in python using pymc3. *PeerJ Computer Science*, 2:e55.

Saunier, O., Didier, D., Mathieu, A., Masson, O., and Le Brazidec, J. D. (2019). Atmospheric modeling and source reconstruction of radioactive ruthenium from an undeclared major release in 2017. *Proceedings of the National Academy of Sciences*, 116(50):24991–25000.

Saunier, O., Korsakissok, I., Didier, D., Doursout, T., and Mathieu, A. (2020). Real-time use of inverse modeling techniques to assess the atmospheric accidental release of a nuclear power plant. *Radioprotection*, 55:107–115.

Saunier, O., Mathieu, A., Didier, D., Tombette, M., Quélo, D., Winiarek, V., and Bocquet, M. (2013). An inverse modeling method to assess the source term of the fukushima nuclear power plant accident using gamma dose rate observations. *Atmospheric Chemistry and Physics*, 13(22):11403–11421.

Scire, J. S., Strimaitis, D. G., Yamartino, R. J., et al. (2000). A user's guide for the calpuff dispersion model. *Earth Tech, Inc*, 521:1–521.

Seibert, P. (2000). Methods for source determination in the context of the ctbt radionuclide monitoring system. In *Informal Workshop on Meteorological Modelling in Support of CTBT Verification, Vienna*, pages 4–6. Citeseer.

Seibert, P., Frank, A., and Kromp-Kolb, H. (2002). Inverse modelling of atmospheric trace substances on the regional scale with lagrangian models. In *Proceedings of the EUROTRAC-2 Symposium*, pages 11–15. Garmisch-Partenkirchen, Germany.

Sofiev, M., Vira, J., Kouznetsov, R., Prank, M., Soares, J., and Genikhovich, E. (2015). Construction of the silam eulerian atmospheric dispersion model based on the advection algorithm of michael galperin. *Geoscientific Model Development*, 8(11):3497–3522.

Sørensen, J., Feddersen, H., Tølløse, K., Uppstu, A., Klein, H., Ulimoen, M., Robertson, L., Pehrsson, J., Lauritzen, B., Hac-Heimburg, A., Roed, H., Améen, E., Syed, N., Blixt Buhr, A., Lindgren, J., and Peltonen, T. (2023). *SOurce CHAracterizatiOn accounting for meTeorologIcal unCertainties (SOCHAOTIC) – final report: Final report of the NKS-B SOCHAOTIC activity.* NKS Secretariat. Report no NKS-470.

Sørensen, J. H. (1998). Sensitivity of the derma long-range gaussian dispersion model to meteorological input and diffusion parameters. *Atmospheric Environment*, 32(24):4195–4206.

Sørensen, J. H. (2018). Method for source localization proposed and applied to the october 2017 case of atmospheric dispersion of ru-106. *Journal of environmental radioactivity*, 189:221–226.

Sørensen, J. H., Baklanov, A., and Hoe, S. (2007). The danish emergency response model of the atmosphere (derma). *Journal of environmental radioactivity*, 96(1-3):122–129.

Sørensen, J. H., Jensen, C. Ø., Mikkelsen, T., Mackay, D., and Donaldson, A. I. (2001). Modelling the atmospheric spread of foot-and-mouth disease virus for emergency preparedness. *Phys. Chem. Earth*, 26:93–97.

Sørensen, J. H., Klein, H., Ulimoen, M., Robertson, L., Pehrsson, J., Lauritzen, B., Bohr, D., Hac-Heimburg, A., Israelson, C., Buhr, A. M. B., Lindgren, J., Karhunen, T., and Peltonen, T. (2020). Nks-430: Source localization by inverse methods (slim). Technical report, Nordic Nuclear Safety Research (NKS).

Sørensen, J. H., Mackay, D. K. J., Jensen, C. Ø., and Donaldson, A. I. (2000). An integrated model to predict the atmospheric spread of foot-and-mouth disease virus. *Epidemiol. Infect.*, 124:577–590.

Stohl, A., Forster, C., Frank, A., Seibert, P., and Wotawa, G. (2005). The lagrangian particle dispersion model flexpart version 6.2. *Atmospheric Chemistry and Physics*, 5(9):2461–2474.

Stohl, A., Seibert, P., Wotawa, G., Arnold, D., Burkhart, J. F., Eckhardt, S., Tapia, C., Vargas, A., and Yasunari, T. J. (2012). Xenon-133 and caesium-137 releases into the atmosphere from the fukushima dai-ichi nuclear power plant: determination of the source term, atmospheric dispersion, and deposition. *Atmospheric Chemistry and Physics*, 12(5):2313–2343.

Stull, R. B., Ahrens, C. D., et al. (2000). *Meteorology for scientists and engineers.*

Tarantola, A. (2005). *Inverse problem theory and methods for model parameter estimation.* SIAM.

Terada, H., Nagai, H., Tsuduki, K., Furuno, A., Kadowaki, M., and Kakefuda, T. (2020). Refinement of source term and atmospheric dispersion simulations of radionuclides during the fukushima daiichi nuclear power station accident. *Journal of environmental radioactivity*, 213:106104.

Thykier-Nielsen, S., Deme, S., and Mikkelsen, T. (1999). Description of the atmospheric dispersion module rimpuff. *Riso National Laboratory, PO Box*, 49.

Tichỳ, O., Šmídl, V., Hofman, R., and Evangeliou, N. (2018). Source term estimation of multi-specie atmospheric release of radiation from gamma dose rates. *Quarterly Journal of the Royal Meteorological Society*, 144(717):2781–2797.

Tølløse, K. S. and Sørensen, J. H. (2024*). A new hybrid particle-puff approach to atmospheric dispersion modelling, implemented in the danish emergency response model of the atmosphere (derma). *manuscript not yet submitted.*

Tomas, J. M., Peereboom, V., Kloosterman, A., and van Dijk, A. (2021). Detection of radioactivity of unknown origin: Protective actions based on inverse modelling. *Journal of environmental radioactivity*, 235:106643.

Tølløse, K. S., Kaas, E., and Sørensen, J. H. (2021). Probabilistic inverse method for source localization applied to etex and the 2017 case of ru-106 including analyses of sensitivity to measurement data. *Atmosphere*, 12(12).

Tølløse, K. S. and Sørensen, J. H. (2022). Bayesian inverse modelling for probabilistic multi-nuclide source term estimation using observations of air concentration and gamma dose rate. *Atmosphere*, 13(11).

Vogelezang, D. and Holtslag, A. (1996). Evaluation and model impacts of alternative boundary-layer height formulations. *Boundary-Layer Meteorology*, 81(3):245–269.

Weiss, W. (2018). Chernobyl thyroid cancer: 30 years of follow-up overview. *Radiation Protection Dosimetry*, 182(1):58–61.

Winiarek, V., Bocquet, M., Saunier, O., and Mathieu, A. (2012). Estimation of errors in the inverse modeling of accidental release of atmospheric pollutant: Application to the reconstruction of the cesium-137 and iodine-131 source terms from the fukushima daiichi power plant. *Journal of Geophysical Research: Atmospheres*, 117(D5).

Wotawa, G., De Geer, L.-E., Denier, P., Kalinowski, M., Toivonen, H., D'Amours, R., Desiato, F., Issartel, J.-P., Langer, M., Seibert, P., et al. (2003). Atmospheric transport modelling in support of ctbt verification—overview and basic concepts. *Atmospheric Environment*, 37(18):2529–2537.

Wyngaard, J. C. (2010). *Turbulence in the Atmosphere*. Cambridge University Press.

Yee, E., Hoffman, I., and Ungar, K. (2014). Bayesian inference for source reconstruction: A real-world application. *International Scholarly Research Notices*, Volume 2014:12 pages.

Yee, E., Lien, F.-S., Keats, A., and D'Amours, R. (2008). Bayesian inversion of concentration data: Source reconstruction in the adjoint representation of atmospheric diffusion. *Journal of Wind Engineering and Industrial Aerodynamics*, 96(10-11):1805–1816.

Zannetti, P. (2013). *Air pollution modeling: theories, computational methods and available software*. Springer Science & Business Media.

Ádám Leelőssy, Lagzi, I., Kovács, A., and Mészáros, R. (2018). A review of numerical models to predict the atmospheric dispersion of radionuclides. *Journal of Environmental Radioactivity*, 182:20–33.